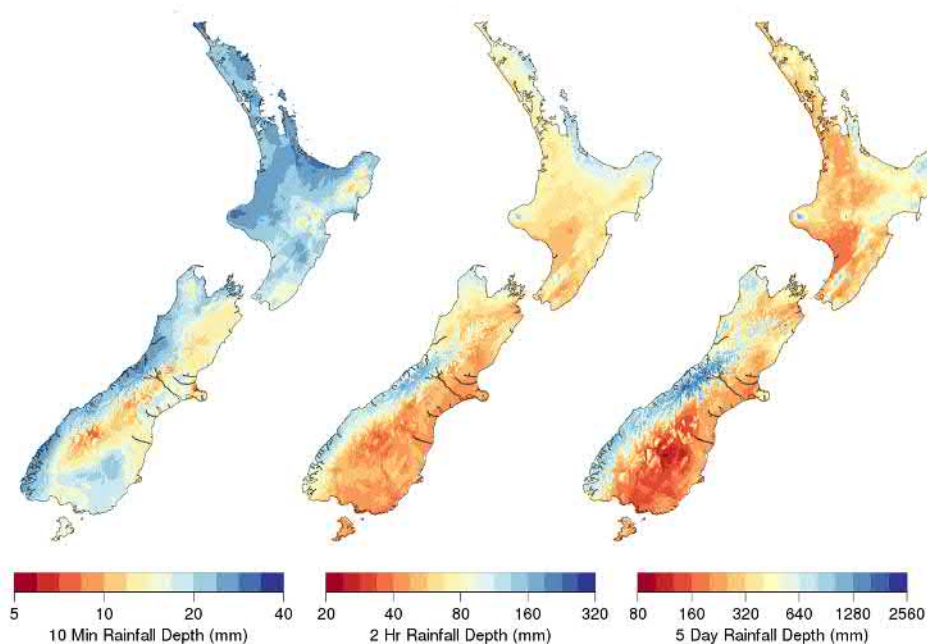


# High Intensity Rainfall Design System

Version 4

*Prepared for Envirolink*

*August 2018*



Prepared by:  
Trevor Carey-Smith  
Roddy Henderson  
Shailesh Singh




For any information regarding this report please contact:

Trevor Carey-Smith  
Climate Scientist  
Climate Dynamics  
+64-4-386 0394  
trevor.carey-smith@niwa.co.nz

National Institute of Water & Atmospheric Research Ltd  
Private Bag 14901  
Kilbirnie  
Wellington 6241

Phone +64 4 386 0300

NIWA CLIENT REPORT No: 2018022CH  
Report date: August 2018  
NIWA Project: ELF16250

Quality Assurance Statement		
	Reviewed by:	Charles Pearson, National Manager, Environmental Information Operations
	Formatting checked by:	Fenella Falconer, Office Administrator
	Approved for release by:	Dr Sam Dean, Chief Scientist for Climate, Atmosphere and Hazards

**Cover Image:** Rainfall depths for 10-minute, 2-hour and 5-day duration events, all with recurrence intervals of 100 years.

---

© All rights reserved. This publication may not be reproduced or copied in any form without the permission of the copyright owner(s). Such permission is only to be given in accordance with the terms of the client's contract with NIWA. This copyright extends to all forms of copying and any storage of material in any kind of information retrieval system.

Whilst NIWA has used all reasonable endeavours to ensure that the information contained in this document is accurate, NIWA does not give any express or implied warranty as to the completeness of the information contained herein, or that it will be suitable for any purpose(s) other than those specifically contemplated during the Project or agreed by NIWA and the Client.

# Contents

- Executive summary ..... 8**
  
- 1 Introduction ..... 9**
  
- 2 Data ..... 11**
  - 2.1 Sources..... 11
  - 2.2 Station coverage ..... 11
  - 2.3 Data pre-processing..... 12
  - 2.4 Merging of neighbour sites..... 13
  
- 3 Regional frequency analysis ..... 14**
  - 3.1 Rainfall index variable..... 14
  - 3.2 Frequency distribution and regional growth curves..... 20
  - 3.3 Depth-duration-frequency calculation ..... 25
  - 3.4 Example results and comparison with HIRDSv3 ..... 28
  
- 4 Climate change response ..... 34**
  - 4.1 Climate scenarios..... 35
  - 4.2 Analysis of RCM extreme precipitation ..... 35
  - 4.3 RCM results..... 38
  - 4.4 Augmentation factors for HIRDS..... 42
  
- 5 Areal reduction factors ..... 46**
  - 5.1 Background ..... 46
  - 5.2 Theory ..... 46
  - 5.3 Analysis ..... 48
  - 5.4 Summary..... 56
  
- 6 Temporal design storm ..... 58**
  - 6.1 Background ..... 58
  - 6.2 Theory ..... 58
  - 6.3 Analysis ..... 59
  - 6.4 Summary..... 65
  
- 7 Conclusion ..... 66**
  
- 8 Acknowledgements ..... 67**

**Tables**

Table 1: Number of stations and station-years available for three main groups of durations. Sub-hourly includes 10-, 20- and 30-minute durations while sub-daily includes hourly to 12-hourly durations. 11

Table 2: Adjustment factors for monthly maxima derived from daily rainfall observations 13

Table 3: Factorial standard errors for selected record lengths derived from annual maxima rainfall series 16

Table 4: Percentage of sites remaining heterogeneous following the Viglione homogeneity testing strategy. 22

Table 5: Factors used by HIRDSv3 for deriving extreme rainfall intensities from current intensity estimates and an expected temperature change [Mullan *et al.*, 2007]. 34

Table 6: Percentage change factors to project rainfall depths derived from the current climate to a future climate that is 1 degree warmer. 44

Table 7: As in Table 6, but showing the variability that could be expected across New Zealand based on the Regional Climate Modelling results. 44

Table 8: New Zealand land-average temperature increase relative to 1986—2005 for four future emissions scenarios. The three 21<sup>st</sup> century projections result from the average of six RCM model simulations (driven by different global climate models). The early 22<sup>nd</sup> century projections are based only on the subset of models that were available and so should be used with caution. 45

Table 9: Gauges used for ARF analysis in each of the three regions. 48

Table 10: Parameters for empirical power law function in Equation (6) fitted to regional areal reduction factors. 53

Table 11: Parameter values in Equation (8) for each of the climate regions and the whole country. Parameters are given for 6 different storm durations. 61

**Figures**

Figure 1: Climate station coverage for HIRDSv4 for 10-minute (left) and 24-hour (right) durations. The size of each point represents the record length and red points are stations that are new since HIRDSv3. 12

Figure 2: Scatter plot of median annual maximum rainfall for all standard durations. On the y-axis are medians obtained from the 50<sup>th</sup> percentile of annual maximum rainfalls, and on the x-axis the medians are computed from a peaks-over-threshold method of monthly maxima. The red line is the 1:1 line. 16

Figure 3: Relationship between the logarithms of the median annual maximum rainfall and its standard error. 17

Figure 4: Parameters for the empirical standard error relationship as derived for each duration. The solid line shows the estimated parameters when fitting to all durations. 18

Figure 5: Median annual maximum rainfall (mm) for 10 minute, 1 hour and 1 day durations. Note the different logarithmic scales. 19

Figure 6: Clustering tree based on regionalised L-moment ratios over the 12 event durations. 23

Figure 7: Spatial distribution of the L-coefficient of variation for the different data types used. 24

Figure 8: Spatial distribution of the L-coefficient of skewness for the different data types used. The equivalent GEV shape parameter, $k$ , is also shown on the colour scale in brackets.	24
Figure 9: Example design rainfalls showing two different DDF models fitted to the data.	27
Figure 10: Mean error of the depth-duration-frequency model over all standard durations and frequencies. Each histogram includes all points in the 2 km digital elevation model.	27
Figure 11: Example 24-hr duration HIRDS growth curve for Auckland Airport. Observed annual maxima are shown as black circles while the blue line shows a GEV distribution fitted directly to this data. The GEV fitted using regional frequency analysis is shown in red. The final HIRDS result following application of the DDF model is shown by the green line. The orange line shows the HIRDS version 3 result.	28
Figure 12: Rainfall depth and standard error for a 24-hour duration event with a 100-year recurrence interval. Depth is shown on the left using a logarithmic scale, while standard error is shown on the right using a linear scale.	29
Figure 13: The percent standard error in rainfall depth for 10- and 100-year recurrence intervals for a selection of event durations.	30
Figure 14: Rainfall depth for a 2-hour duration event with a 100-year recurrence interval. Results from the previous version of HIRDS are shown on the left and the current analysis is on the right.	31
Figure 15: Difference in rainfall depth between the previous version of HIRDS and the current analysis for a 100-year recurrence interval. The percentage difference (relative to HIRDSv3) is shown for three different event durations.	32
Figure 16: Rainfall depths for all standard durations and for four different average recurrence intervals. The top row displays rainfall depths for a 5 year recurrence interval, the next row for 20 year, the third row for 100 year and the bottom row a 250 year recurrence interval. The 12 durations are shown from left to right; 10, 20 and 30 minute; 1, 2, 6 and 12 hour; and 1, 2, 3, 4 and 5 day.	33
Figure 17: Projected New Zealand-average temperatures relative to 1986-2005 for six CMIP5 global climate models downscaled via NIWA's RCM. Historical simulations (here 1971-2005) and four future simulations (RCPs 2.6, 4.5, 6.0 and 8.5) are included [Mullan <i>et al.</i> , 2016].	36
Figure 18: The 24-hour annual maxima series at a point near Dunedin for two RCM simulations driven by the HadGEM2-ES global CMIP5 model (black lines). RCP2.6 (left) and RCP8.5 (right) are included for comparison. Event magnitudes for three different return periods derived from a non-stationary GEV fit to the data are shown in the coloured lines.	36
Figure 19: Distributions of $\mu$ (left) and $\sigma$ (right) trends over all RCM land points for 4 different RCPs. Each histogram includes all six CMIP5 GCMs.	37
Figure 20: The RCM derived 100-year event magnitude of a 24-hour duration event. Each map is a multi-model mean over 24 separate RCM simulations. The results based on the current climate (1985—2005) are shown on the left while the centre and right maps show projections based on the 1 and 2.6 degrees of warming. These latter two images (and most other images in this section) are not associated with a particular future period, rather they show results associated with a particular temperature change. This has been done to reduce the complexity that comes when dealing with multiple possible emissions scenarios.	38

Figure 21: Percentage changes per degree of warming in the 24-hour duration, 50-year event magnitude for each individual model simulation. The top row shows the change based on the RCP4.5 emissions scenario and the lower row shows the change based on the RCP8.5 scenario.	39
Figure 22: Percentage changes per degree of warming in the 50-year event magnitude for each GCM driving model. The top row shows the change for the 1-hour duration event and the bottom row for the 5-day event.	40
Figure 23: Trends in $\mu$ and $\sigma$ as a function of temperature, for four different event durations, derived from all 24 RCM simulations combined. Each parameter is mapped as a percentage change relative to $\mu$ over the 1986–2005 period.	41
Figure 24: Percentage changes in the 50-year event magnitude for four different event durations. Each map combines all 24 different RCM simulations and shows the change per degree of warming.	42
Figure 25: Augmentation factors for extreme precipitation based on 1 degree of warming plotted as a function of return period. The solid lines show the median over New Zealand for different event durations and the 5 <sup>th</sup> and 95 <sup>th</sup> percentiles are displayed as shaded bars for the 1- and 120-hour event durations.	43
Figure 26: Examples of Thiessen polygons for 10 and 100 km <sup>2</sup> areas in the Auckland region. Black circles represent stations used in the study. Colours pertain to the different Thiessen groups for the given area. For the 10 km <sup>2</sup> area, there are 12 different Thiessen groups, each containing 2 gauges. For the 100 km <sup>2</sup> area, there are four groups containing between 5 and 14 gauge each.	50
Figure 27: Areal reduction factors for a 100 km <sup>2</sup> area derived from Auckland gauges. Different colours denote the different methodologies used.	52
Figure 28: As Figure 27 but for the Christchurch and Tasman regions.	52
Figure 29: Empirical power law function fitted to areal reduction factors for Auckland (left), Christchurch (centre) and Tasman (right). All panels show 1-ARF on a logarithmic scale on the y-axis with calculated ARF values as solid lines and the empirical fits as dashed lines. The top row shows each different area (as colours) plotted as a function of duration. The bottom row shows the different durations (as colours) plotted as a function of area. For both duration and area, the x-axis is also on a logarithmic scale.	53
Figure 30: The same data as Figure 29, but separated by area and showing ARF on a non-logarithmic y-axis. The different regions are shown as different colours and areal reduction factors as published by <i>Tomlinson</i> [1980] are shown by the dotted orange line. The dashed black line shows the empirical model as fitted to all three regions at once.	54
Figure 31: Areal reduction factors as a function of return period for a range of durations and areas. The curves derived from the three regional datasets are shown as solid lines and an empirical fit to these results is depicted by the dashed lines. Note the different y-axis scales.	55
Figure 32: Area reduction factors (in %) derived from the empirical model of Equation (6) fitted to all three regions.	57
Figure 33: Location of raingauges and regions used for the temporal design storm analysis.	59
Figure 34: Fitted cumulative hyetograph (red line) for raingauges in the east of the South Island region for all durations. The cumulative hyetographs based on observations from each raingauge are shown by thin grey lines.	60

- Figure 35: Fitted cumulative hyetographs for various durations showing results for individual regions (coloured lines) and for the whole country (thick black line). 62
- Figure 36: Fitted cumulative hyetograph (red line) for the 72-hour duration at each climate region. The cumulative hyetographs based on observations from each raingauge are shown by thin grey lines. 63
- Figure 37: Average fitted cumulative hyetographs for various durations for North and South Islands. 64

## Executive summary

Using a regionalised index-frequency method, estimates of high intensity rainfall for all New Zealand have been revised for use in the High Intensity Rainfall Design System (HIRDS). This update of HIRDS has been prepared in consultation with Regional Councils and was funded through an Envirolink Tools Grant. The project has endeavoured to utilise all available historical records and the most up-to-date rainfall measurements gathered from multiple agencies. This comprehensive data set has enabled more accurate estimates of median annual maximum rainfall and more robust regionalisation of growth curve parameters than was possible in earlier versions of this work. This is particularly true for sub-daily event durations and even more so sub-hourly durations.

The main purpose of HIRDS is to provide estimates of high intensity rainfall at ungauged locations for a range of return periods and event durations. These depth-duration-frequency (DDF) tables can be used for design storm assessment and in the design of flood protection works and other waterway structures. HIRDS DDF tables can also be used for flood modelling, including flood routing, retention basin design and inundation mapping activities, helping to minimise flood risk within communities across the country. In certain circumstances HIRDS may be used for post-event analysis, however, it has been designed to provide reliable estimates of return periods at ungauged locations, not to replace site-specific extreme value analysis at gauged locations.

The impact of future climate change on extreme rainfall has been assessed using regional climate model simulations of rainfall over New Zealand. From these simulations, amplification factors that can be applied to depth-duration-frequency tables have been estimated for four different emissions scenarios and two future time slices. These factors allow estimates of future extreme rainfall intensities to be derived based on those calculated from historical rainfall records.

Several established areal reduction methodologies have been applied to different regions across New Zealand and using the most appropriate, area reduction factors have been estimated for three regions in New Zealand and extended to apply to New Zealand as a whole. A literature review and extensive analysis has been made into temporal design storm patterns and storm curves have been estimated for the six main climate regions of New Zealand.

This report is intended to be a technical documentation of the data and methodology used in the HIRDS analysis. Summary information and access to the estimates of high intensity rainfall derived in this report, along with climate change projections, is available through the online tool found at <https://hirds.niwa.co.nz>.



# 1 Introduction

Reliable and locally relevant estimates of extreme rainfall intensities are vital to a large variety of planning and engineering practices. These include the design of infrastructure to protect human life and mitigate damage from flooding, rainfall and runoff design guidelines, design storm analysis and flood hazard planning.

To this end, with support from Regional Councils, an update to the High Intensity Design Rainfall System (HIRDS) has been performed via an Envirolink Tools Grant. The previous version of the HIRDS tool (version 3) was in urgent need of upgrading as, although launched in 2010, it was mostly based on rainfall records up to 2006. The large increase in automated raingauges in the last two decades, and the realisation that many older records were not included in the HIRDSv3, meant that there is valuable additional insight into storm design to be gained by updating the HIRDS tool.

The main purpose of this work is to develop a method and an associated tool to estimate high intensity rainfall at ungauged locations for a range of return periods and event durations. The depth-duration-frequency (DDF) tables produced using this method are expected to be used for design storm assessment and in the design of flood protection works and other waterway structures. The DDF tables will also be applicable to flood modelling, including flood routing, retention basin design and inundation mapping activities, thereby helping to minimise flood risk within communities across the country.

In certain circumstances, the resulting tool may also be used to estimate return periods for post-event analysis, for example comparing a particular rainfall gauge event magnitude to the equivalent DDF output. However, except for cases where the gauge record is short, it is preferable to estimate the event return period directly from an extreme value analysis of the gauge record itself. That is, the main purpose of the tool developed here is to provide reliable estimates of return periods at ungauged locations, not to replace site-specific extreme value analysis at gauged locations.

Extreme rainfall in New Zealand has been studied for many years, with early investigations into the frequency of heavy rainfall published by the New Zealand Meteorological Service [Robertson, 1963; Seelye, 1947]. Following that, several regional frequency analyses of extreme rainfalls and floods have been undertaken in New Zealand [Thompson, 1992; 2002; 2011; Tomlinson, 1980, for rainfall]; [Beable and Mckerchar, 1982; Mckerchar and Pearson, 1989, for floods]. A computer-based procedure for estimating rainfall event quantiles, called HIRDS (High Intensity Rainfall Design System), was first developed in 1992 and was based on Tomlinson's [1980] graphical method of rainfall frequency analysis.

In 2002, the calculation of high intensity rainfalls was revised and updated to incorporate a large increase in archived rainfall data, and to take advantage of the robust analysis techniques afforded by regional frequency analysis. This version (HIRDSv2) was available as a Windows® executable. In 2011, a revised and updated analysis, incorporating many regional council gauges and feedback on previous versions, was completed and the results made available via an online tool hosted on NIWA's website (HIRDSv3).

The underlying method in the second and third version of HIRDS [Thompson, 2002; 2011] is an index-frequency procedure. The index-variable is a relatively common event [Dalrymple, 1960; Stewart et al., 1999], such as the median annual maximum rainfall that can be computed typically from the

available record. The frequency-variable is derived from a regional analysis, where data from several sites are combined to estimate a dimensionless rainfall growth curve which represents a set of factors at different recurrence intervals relative to the index variable.

This report describes a further revision of HIRDS which includes additional rainfall observations that were not included in HIRDSv3, both recent records to bring the tool up to date and older records that were missing from previous versions. The rainfall data and pre-processing methodology are described in Section 2. The underlying index-frequency procedure is very similar to that used in the previous version of HIRDS and is described in Section 3. This section also explains how the depth-duration-frequency tables are calculated including a discussion on how the tool has been extended to include event durations of 4 and 5 days and return periods of 250 years.

Section 4 covers a new analysis that has been performed to update the factors used to estimate the response of extreme rainfall to climate change. Using the regional climate model simulations performed by NIWA based on four future climate scenarios (relative concentration pathways or RCPs) estimates of the change in rainfall depth, for different event durations and frequencies, have been calculated for both the mid and late 21<sup>st</sup> century. Sections 5 and 6 provide some background and guidelines for the use of areal reduction factors and temporal design storm profiles, respectively. These sections evaluate and describe the most appropriate methodologies to use within New Zealand before providing results for different regions and New Zealand as a whole.

## 2 Data

To generate nationwide estimates of maximum precipitation depth over a range of durations and return periods it is necessary to have a comprehensive dataset of rainfall observations covering as much of the country as possible. In addition, to estimate low probability events very long records are needed. For optimum results, then, it is important to gather as many precipitation records as possible.

### 2.1 Sources

In New Zealand, there are two main repositories for rainfall records, both managed by NIWA; the Climate Database (CliDB) and National Hydrometric Database (NHD).

CliDB contains climate station observations from both manual rain gauges and automatic stations that are now managed by both NIWA and MetService. In addition, CliDB also hosts weather observations from approximately 120 sites managed by Fire and Emergency New Zealand. The NHD contains rainfall observations collected mainly for hydrological purposes. This archive includes hydrology sites managed by NIWA and also holds copies of many of the records stored in New Zealand Regional and District Council archives. In addition, rainfall data was sourced directly from Regional and District Councils.

### 2.2 Station coverage

This HIRDS update has expanded the rainfall dataset by extending the end date of the rainfall records obtained from CliDB from 2008 to 2016, an additional 8 years of data. For NHD data, the end data for HIRDSv3 was 2005 for about 2/3 of stations and 2008 for the remainder; this has been extended to 2015 for HIRDSv4 except for Auckland Council which extends to early 2017.

HIRDSv4 has 59 additional manual stations with at least 6 years of monthly data bringing in a total of 881 additional years of daily rainfall observations. Additional CliDB stations with at least 6 years of hourly rainfall observations number 197 providing a combined total of 2785 additional years of data. Many of these sites are part of the network managed by Fire and Emergency New Zealand. For 10-minute observations, there are 23 additional CliDB stations totalling 178 years of data. There are 192 additional stations available from the NHD providing a total of 2360 additional years of data for all event durations.

The total number of stations used in HIRDSv4 is 3404 and the numbers of stations available for the various duration classes are shown in Table 1. The geographical coverage of these sites is displayed in Figure 1 which also shows which sites are new and gives an indication of their record length. It is clear that some regions of New Zealand have much better coverage than others and this generally correlates with population density. In particular, the south west of the South Island, inland from Kaikoura and the Central Plateau have lower station density than other areas.

**Table 1: Number of stations and station-years available for three main groups of durations. Sub-hourly includes 10-, 20- and 30-minute durations while sub-daily includes hourly to 12-hourly durations.**

	Sub-hourly	Sub-daily	Daily
Number of Stations	1134	1353	3402
Number of Station-Years	22373	25929	97854

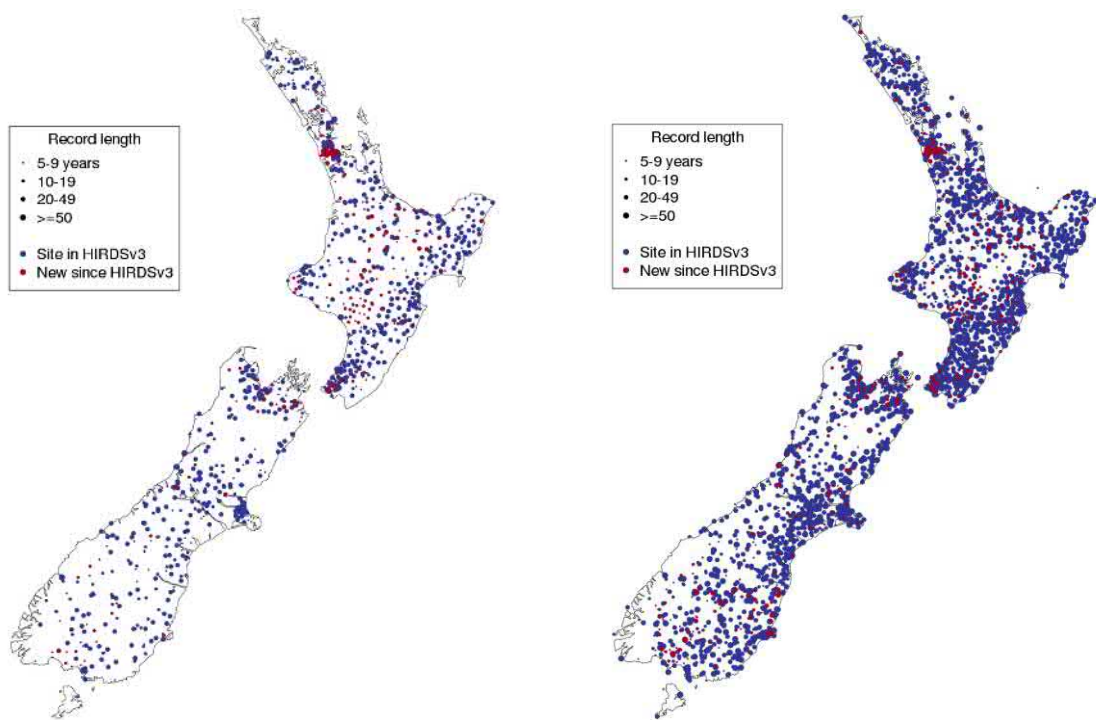


**Figure 1: Climate station coverage for HIRDSv4 for 10-minute (left) and 24-hour (right) durations. The size of each point represents the record length and red points are stations that are new since HIRDSv3.**

## 2.3 Data pre-processing

Rainfall records are stored in a variety of formats in the source databases. Most of the NHD records and some in CliDB are stored as events where each data point contains both a rainfall depth and the duration over which it fell. This format allows high temporal resolution data to be stored in a compact form as long dry periods can be stored as single events. Conversely, many of the records in CliDB are stored as time-series with regular temporal spacing. The different accumulation periods used in CliDB include 10 minute, 1 hour and 24 hours.

### 2.3.1 Creating monthly maxima

To be of use for the regional frequency analysis, the source rainfall data needs to be processed to produce monthly maxima for each of the standard durations used in HIRDS. For version 4, these durations are 10, 20 and 30 minutes; 1, 2, 6 and 12 hours; and 1, 2, 3, 4 and 5 days. Monthly maxima are calculated simply by finding the maximum rainfall that fell over the required duration any time during the month in question. There are however, a couple of points that need to be taken into consideration during this calculation.

Firstly, the (artificial) boundary between months should not limit whether an event occurred. That is, when searching for the largest event in any month, the end of the preceding month and beginning of the following month need to be included. This leads to the second issue, which is that an event (or part of an event) should not be double counted. When maxima from consecutive months are being calculated, it is necessary to ensure that if an event which straddles the month boundary is assigned to one month, then any part of that event already accounted for should not also be included in the largest event for the second month.

In practise, the simplest way to avoid these issues is to process the entire rainfall record for a given site and event duration at once. This can be done iteratively by first finding the largest event;

assigning it to the correct month; removing that month and event from the record; and then repeating the iteration by finding the next largest event in the record.

For records stored as regular time-series, the shortest duration for monthly maxima is of course the same as the temporal resolution of the original record (hence a much larger number of stations available for daily durations than sub-daily or sub-hourly). For event-based rainfall records, it is convenient to convert the record into a fixed frequency time-series so it can be processed into monthly maxima using the same methodology, however it is important that the temporal resolution of this intermediate step is not so coarse that errors are introduced. This can be ensured by setting the intermediate resolution at least 10 times shorter than the required duration.

### 2.3.2 Daily measurement adjustment factors

When daily data (usually recorded from 9am to 9am) are used to estimate monthly maxima, significant errors are introduced due to the rigid sampling that has been imposed. When a maximum is found for a given month, the chance that the true maximum was missed because it straddled two daily measurements is quite high. Adjustments should be made to monthly maxima calculated from daily observations to account for this bias. Adjustment factors appropriate for New Zealand can be estimated using available sub-daily rainfall records by comparing the true monthly maxima to those obtained when only using rainfall accumulations from 9am to 9am.

Adjustment factors for 1 through 5-day durations were estimated from the HIRDSv4 data set and are shown in Table 2. These values are slightly different from those used in the previous version of HIRDS and although slightly larger than those given by the WMO, they are broadly consistent with both sets of adjustment factors.

**Table 2: Adjustment factors for monthly maxima derived from daily rainfall observations**

	1 day	2 day	3 day	4 day	5 day
WMO	1.13	1.04	1.03	1.03	1.02
HIRDSv3	1.14	1.07	1.04		
HIRDSv4	1.148	1.056	1.045	1.036	1.030

## 2.4 Merging of neighbour sites

Precipitation exhibits large fluctuations in both time and space [see for example *Austin and Houze, 1970*]; yet despite this near neighbour rainfalls tend to show high inter-site correlations [*Nandakumar et al., 1997*]. For this study, rainfall sites within 500 m of each other were merged into composite site series. A distance of 500 m was used as it is large enough to capture small site relocations, but well within the 2 km resolution of the final HIRDS surfaces.

Merging of neighbouring sites allowed the extension of the monthly maxima time series if they were mutually exclusive. Where rainfall records overlapped, the maximum value of the contributing sites was chosen for the extreme rainfall series. This process also provided an estimate of the extreme if missing values existed within any of the series. Neighbouring sites were chosen in an iterative process, by first grouping the closest sites together then checking if any additional sites are still within 500 m. This prevents combining two sites together which may be closer than 500 m, but would be better left separate and combined with other, nearer stations. Amalgamation reduced the total number of sites to 3168.

### 3 Regional frequency analysis

A fundamental issue in the estimation of quantiles is the need to extrapolate to recurrence intervals significantly larger than the available records. A second issue is the ability to estimate quantiles at locations for which no observed records are available. Both issues can be solved using regionalisation, a standard practice for improving the estimation of event quantiles at sites with comparatively short records. Among the various regionalisation procedures, a widely used one is the index-flood (also called index-rainfall or index-frequency) method first proposed by *Dalrymple* [1960] for flood frequency estimation. The basic principle of this approach is defining statistically homogeneous regions containing sites with similar frequency distributions apart from a scaling factor (the index variable).

Dalrymple defined the index-variable as the mean annual flood (i.e., the 2.33-year recurrence interval derived from a Gumbel frequency curve for each site), and the regional growth curve (frequency-variable) as the median of at-site event quantiles estimated from empirical at-site growth curves. In this study, the median annual maximum rainfall has been used for the index, or scaling, variable and the Generalised Extreme Value distribution has been used to model the frequency distribution, or growth curve. Instead of dividing the country up into fixed homogeneous regions, this study finds a homogeneous region for each rain gauge. These regions will overlap and provide enough data to derive a frequency distribution for each gauge. The details of this methodology are described in this section.

#### 3.1 Rainfall index variable

In this report, and in line with other studies, [*Faulkner*, 1999; *Jakob et al.*, 2007; *Stewart et al.*, 1999; *Thompson*, 2002] the median annual maximum rainfall,  $R_{MED}$ , was used in preference to the mean annual maximum rainfall. The median has an annual exceedance probability (equivalent to  $1 - q$ ) of 0.5, corresponding to an annual recurrence interval of 2-years and is expected to be exceeded “every other year”. More importantly, it is a robust and resistant estimator of distribution location and is not usually affected by the skewness of the distribution or by the presence of outliers. However, the standard error of the sample median is generally larger than that of the sample mean.

*Robson and Reed* [1999] provide complementary procedures in computing the index variable (in their case flow rate) based on the record length of the available at-site data. For series with at least 14 years of ranked annual maxima, the median annual maximum is easily found as the middle-ranking value or 50<sup>th</sup> percentile. When the record length is shorter, data are extracted in a peaks-over-threshold (POT) form, and an annual exceedance series is created containing on average one event per year. In general peaks-over-threshold can provide improved estimates of event quantiles, with smaller standard errors, as the procedure utilises multiple rainfall exceedances in a year that would otherwise not be included if there were just annual maxima. For this analysis, monthly maxima were used in the POT approach instead of a full daily (or similar) time series. This means the series only approximates the true POT distribution, as independent storm maxima may occur in the same month. However, as only the median annual maximum is being estimated here, this approximation will have minor impact.

### 3.1.1 Peaks over threshold technique

*Robson and Reed* [1999] provide the theoretical link between peaks-over-threshold and annual maximum series. If the POT series follows a Poisson process then the annual exceedance probability ( $AEP_R$ ) of an event with magnitude  $R$  is given by

$$AEP_R = 1 - e^{-\lambda_R}$$

where  $\lambda_R$  is the exceedance rate which can be estimated at each ordered position of a POT series of length  $N$  as

$$\lambda_{R_i} = \frac{i - 0.5}{N}.$$

$R_{MED}$  is evaluated by finding the two points in the POT series which are above and below an  $AEP_R$  of 0.5 ( $R_i$  and  $R_{i+1}$ ).  $R_{MED}$  is the weighted average of these two points

$$R_{MED} = wR_i + (1 - w)R_{i+1}$$

where  $w$  is defined as

$$w = \frac{RV_{R_{i+1}}}{RV_{R_{i+1}} - RV_{R_i}}$$

using the reduced variate

$$RV_R = \ln \frac{AEP_R}{1 - AEP_R}.$$

A POT series can be tested to see if it follows a Poisson process by evaluating its index of dispersion,  $D$ , which is defined as the ratio between the variance and mean of the number of events per year. If  $D$  is close to 1, then the series follows a Poisson process. For the HIRDS dataset, the mean of the index of dispersion over all stations (weighted by the length of the POT series) comes to 0.97, so the assumption that events occur randomly in time seems valid.

A variation of the *Robson and Reed* [1999] scheme was applied in this study. At sites of 6 – 20 years of records, the median annual maximum is determined from ranked monthly maxima using a peaks-over-threshold method, while at sites with longer records (more than 20 years), the 50<sup>th</sup> percentile of ranked annual maxima were computed. Figure 2 shows a scatter-plot of the index rainfall computed by the two methods regardless of record length. On the y-axis of the median from the annual maximum series, and on the x-axis are the median from the equivalent peaks-over-threshold approach. There is very close agreement. Points with greatest departure from equality line tend to be sites with relatively short records.

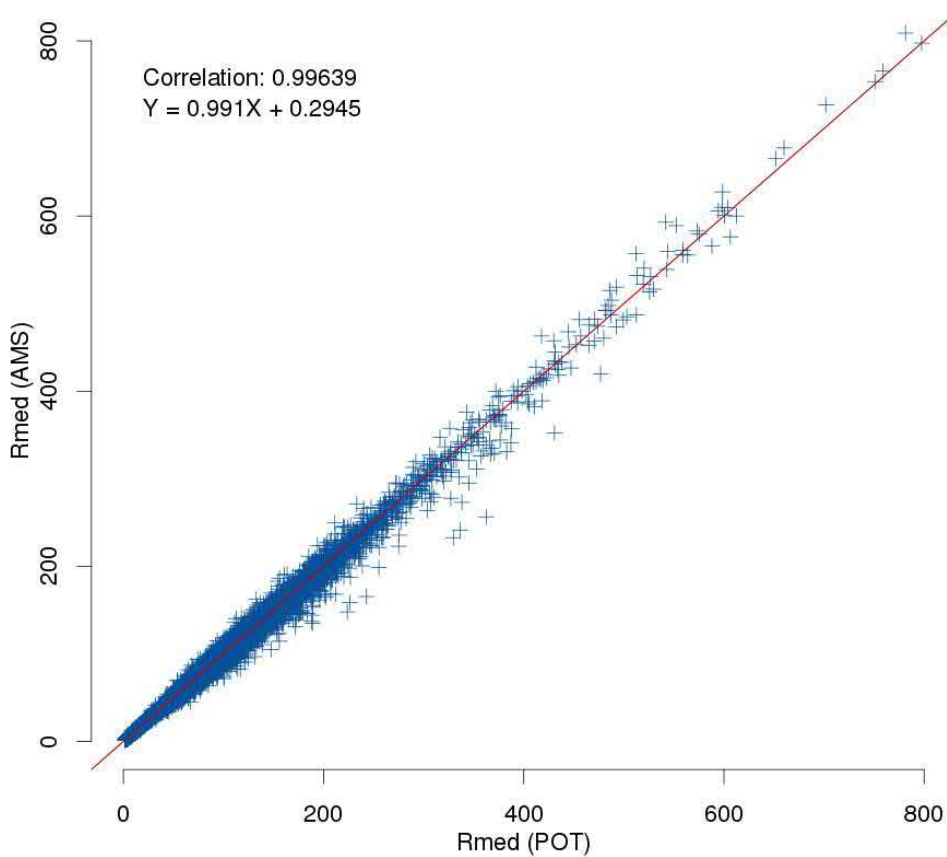


**Figure 2: Scatter plot of median annual maximum rainfall for all standard durations. On the y-axis are medians obtained from the 50<sup>th</sup> percentile of annual maximum rainfalls, and on the x-axis the medians are computed from a peaks-over-threshold method of monthly maxima. The red line is the 1:1 line.**

### 3.1.2 Standard error estimation

As no assumption has been made on the underlying frequency distribution for  $R_{MED}$ , resampling methods [Robson and Reed, 1999] are used to estimate the uncertainty (or standard errors) associated with the median annual maximum rainfall. For large sample sizes, a balanced resampling method is used, and for small record lengths, a factorial standard error approach is used.

The basic idea of resampling is to take the observed data set and generate hypothetical samples [Reed, 1999]. In balanced resampling, the observed data values are replicated  $M$  times to form a super-sample data set. These values are randomly re-ordered and divided into  $M$  sets of data. The median of each resample is derived from which the standard error,  $se$ , is computed. This method has been used to estimate the standard error for  $R_{MED}$  calculated from annual maxima series.

The factorial standard error,  $fse = e^{se}$ , is the exponential of the standard error on a logged scale, and is used to estimate the uncertainty in  $R_{MED}$  in terms of multiplicative errors [Robson and Reed, 1999]. Empirically derived factorial standard errors from New Zealand data sets are given in Table 3.

**Table 3: Factorial standard errors for selected record lengths derived from annual maxima rainfall series**

N	6	8	10	12	14	16	18	20	25	30
$fse$	1.179	1.154	1.138	1.126	1.117	1.109	1.103	1.097	1.090	1.080



These were calculated by estimating the standard error via balanced resampling for each different record length. Values close to 1 indicate good estimates of the median annual maxima. Factorial standard errors have been used to estimate the standard error for  $R_{MED}$  calculated using the peaks over threshold approach. As the standard error is approximately symmetric about  $R_{MED}$ , the uncertainty associated with the median annual maximum is  $se \approx R_{MED}(fse - 1)$ .

When the logarithm of the median annual maximum estimate and its standard error are compared, there exists a linear relationship between them ( $se = aR_{MED}^b$ ) that is largely independent of duration and sample size. As shown in Figure 3, which contains all durations, errors increase as medians increase. Using linear regression, an empirical relation for uncertainty in  $R_{MED}$  is found to be

$$se = 0.12R_{MED}^{0.92}$$

which is similar to those found for the earlier versions of HIRDS [Thompson, 2002; 2011].

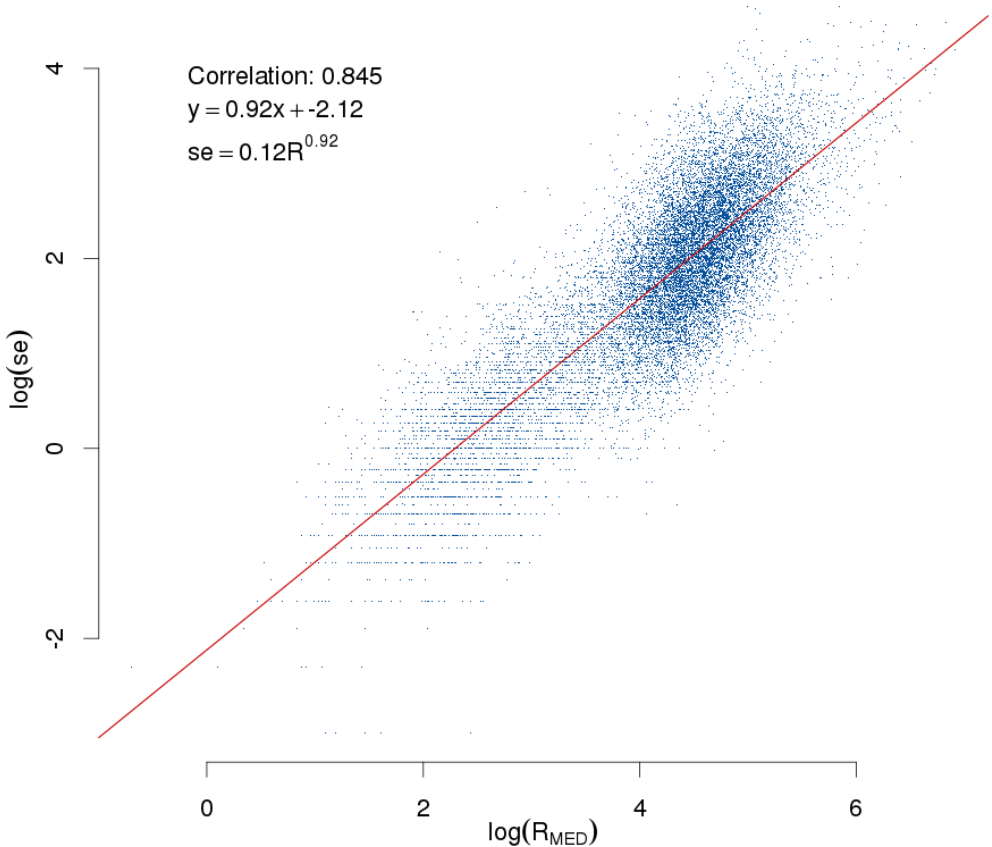


**Figure 3: Relationship between the logarithms of the median annual maximum rainfall and its standard error.**

When this relationship is fitted for each duration separately, the parameters  $a$  and  $b$  are broadly consistent, although the smaller sample sizes (particularly for shorter durations) result in some variability between estimates (Figure 4). While this empirical method for estimating the standard

error in median annual rainfall is not accurate for all locations, it has been used in this study for locations where no other estimate was available.

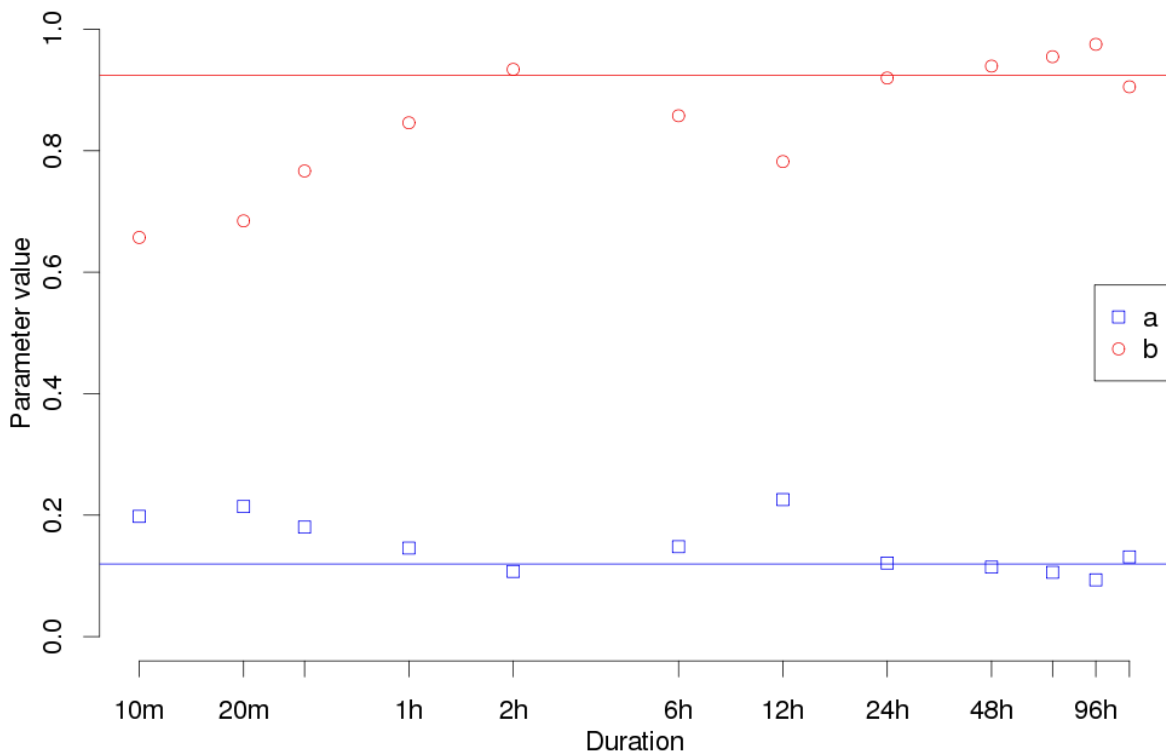


**Figure 4: Parameters for the empirical standard error relationship as derived for each duration. The solid line shows the estimated parameters when fitting to all durations.**

### 3.1.3 Mapping the rainfall index variable

Surfaces of median annual maximum rainfall were fitted with a tri-variate thin-plate spline, with the three independent variables being easting, northing and elevation above sea level. The tri-variate spline allows for a continuous spatially varying dependence on elevation [Hutchinson, 1995], is well suited to applications over complex terrain as is found in New Zealand, and can provide a robust method of surface fitting meteorological data from moderately sparse data networks [Tait et al., 2006]. Correctly specifying elevation units is critical to the performance of thin-plate splines [Hutchinson, 1995]; as a rule the elevation scaling should be 100 times the horizontal scale. With position coordinates in kilometres, elevation should be in decametres.

All 12 surfaces were fitted using a common signal to error ratio and were mapped using the ANUSPLIN software package onto a 2 km by 2 km digital elevation model. Fitting multiple surfaces simultaneously (i.e., 10 to 30 minutes, 1 to 12 hours, and 1 to 5 days) ensures consistency between the surfaces in the group. For 10 to 30 minutes there were 957 sites available, for 1 to 12 hours there were 1123 sites available, and for the daily durations 2849 sites. The three groups are analysed separately to allow for the larger number of sites available at longer durations.

Following the spline interpolation procedure, a bias correction step has been performed to ensure that the largest  $R_{MED}$  values have not been excessively reduced by the smoothing process. This was done by performing quantile-quantile matching between the station and spline  $R_{MED}$  values.

Maps showing the 10 minute, 1 hour and 1 day median annual maximum rainfall over New Zealand are shown in Figure 5. The strong influence of New Zealand’s orography on the rainfall pattern is noticeable, in particular for the 1 day duration, in that the largest values are found in the mountainous regions of both islands. However, for the 10-minute duration, the north of the North Island has values of similar magnitude to the mountainous regions and the west coast of the South Island.

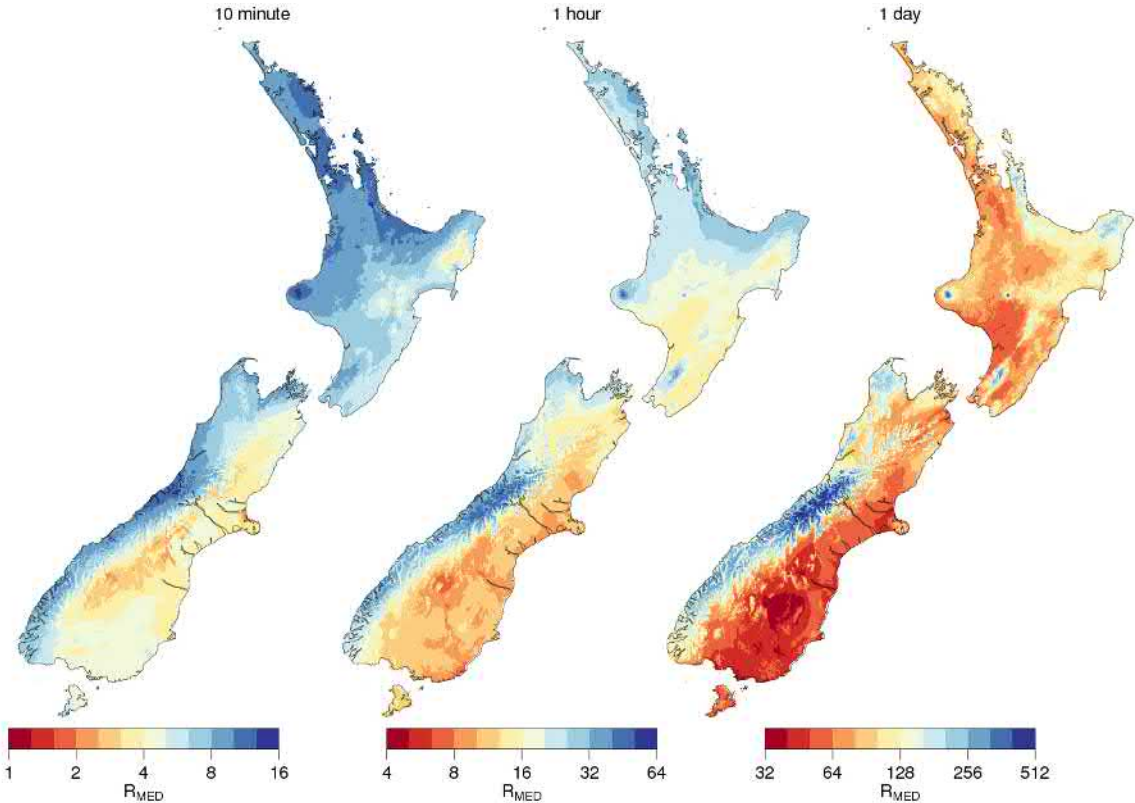


**Figure 5: Median annual maximum rainfall (mm) for 10 minute, 1 hour and 1 day durations. Note the different logarithmic scales.**

## 3.2 Frequency distribution and regional growth curves

The second component in the index-frequency method is the development and application of regional growth curves derived from cumulative frequency distributions of fitted annual maximum rainfalls. As in the previous version of HIRDS, the Generalised Extreme Value (GEV) distribution was selected to fit annual maximum rainfalls in New Zealand for the 12 storm durations used in this study.

### 3.2.1 Generalised Extreme Value distribution

The GEV is a flexible, three-parameter distribution that combines three extreme-value distributions within a single framework: the Gumbel (EV1), Frechet (EV2) and Weibull (EV3) [Jenkinson, 1955]. The parameters of the distribution are  $\sigma > 0$ ,  $\mu$  and  $k$  (the scale, location and shape respectively) with a cumulative frequency distribution function given by

$$F(z) = \begin{cases} e^{-(1-kz)^{1/k}}, & k \neq 0 \\ e^{-e^{-z}}, & k = 0 \end{cases} \quad (1)$$

where  $z = (x - \mu)/\sigma$  and  $k$  is the shape parameter. When  $k = 0$ , the three parameter GEV distribution reduces to the 2 parameter Gumbel;  $k < 0$  corresponds to a lower bound, heavy-tail Frechet distribution; and  $k > 0$  to an upper bound light-tail Weibull distribution.

The first three L-moments of the GEV are

$$\begin{aligned} \lambda_1 &= \mu + \frac{\sigma(1 - \Gamma(1 + k))}{k} \\ \lambda_2 &= \frac{\sigma(1 - 2^{-k})\Gamma(1 + k)}{k} \\ \lambda_3/\lambda_2 &= \tau_3 = \frac{2(1 - 3^{-k})}{1 - 2^{-k}} - 3 \end{aligned} \quad (2)$$

where the  $\tau_3$  L-moment ratio is analogous to the conventional coefficient of skewness and  $\tau_2 = \lambda_2/\lambda_1$  is the L-coefficient of variation, and  $\lambda_1$  is the mean [Hosking, 1990].

Two common methods of estimating the GEV parameters are method of maximum likelihood and the method of L-moments. Morrison and Smith [2002] proposed methods for estimating the GEV parameters that combine both maximum likelihood and L-moment methods. Subsequently, Ailliot et al. [2011] extended their method to include the asymptotic covariance structure of the estimates. The parameter estimation method denoted M1 by Ailliot et al. [2011] is used here, where the shape parameter is determined using maximum likelihood, the scale and location parameters are estimated by L-moments. This is like the MIX2 method in Morrison and Smith [2002], but subject to an additional constraint of  $-0.5 < k < 0.5$ .

Although  $k$  is estimated using the mixed L-moment and maximum likelihood M1 method, the subsequent mapping of the frequency distribution parameters was performed on the L-moment ratios so involved determining  $\tau_2$  and  $\tau_3$ .

Parameters of the GEV distribution were fitted to data for each of the 12 durations at each site, provided there was at least 15 years of annual maximum rainfalls for the sub-daily durations, and 18 years for the daily durations. This reflects the relative lengths of the data where the record lengths of the annual maxima are generally smaller for sub-daily durations than for the longer durations. The

minimum record length is also a compromise between fitting GEV distributions with small amounts of data which can lead to difficulties in reliably estimating the shape parameter [Lu and Stedinger, 1992; Martins and Stedinger, 2000], and having a sufficiently large number of spatially distributed sites across New Zealand in order to produce acceptable nationwide maps of GEV parameters.

### 3.2.2 Regionalisation

Regional frequency analysis is a common method used in the estimation of quantiles when rainfall or river flow records are too short to allow reliable estimation of long recurrence intervals. A region of influence is a site-specific region with a collection of sites with similar extreme rainfall properties that can be used in the estimation of quantiles at the site of interest [Burn, 1990; Burn and Goel, 2000]. The collection of sites should be able to form a homogeneous region, and ideally the site of interest should be close to the centre of the group of sites as determined by an appropriate similarity measure [Burn, 1997].

The number of sites to include in the region of interest is chosen to provide a large enough total number of station-years,  $N_s$ , while retaining homogeneity within the group of sites. Hosking and Wallis [1988] recommended the use of 20 sites as being optimal, while Cluckie and Pessoa [1990] suggested that at least 300 station-years provided stability. More recently, it has been recommended by Burn [1997] and Robson and Reed [1999] to use 5 times the length of the required recurrence interval as a guide to the optimal total number of station-years. Using this rule of thumb, the maximum recurrence interval of 250 years that this version of HIRDS is required to provide suggests a total number of station-years of 1250. However, because the 100-year return period will be more commonly used, a lower value of 1000 years has been used for  $N_s$ , as a compromise between 500 and 1250 station years for return periods 100 and 250 years, respectively. For sub-daily durations,  $N_s$  has been reduced further to 800 due to the sparser network of sub-daily observations.

Stations should not be included in the region of interest simply to achieve the target number of station-years if they are too dissimilar from the central site. Homogeneity of stations is ensured via a three-stage process. Firstly, for each site and duration, stations are ordered based on geographic distance from the target site and enough sites are selected to bring the total station-years to  $3 \times N_s$ .

Secondly, a similarity metric is used to rank these sites based on selected station attributes and to remove those which are too dissimilar. The attributes used in this step were the second and third L-moment ratios ( $\tau_2$  and  $\tau_3$ ) and 90<sup>th</sup> percentile of the annual maxima series. The metric used was the Mahalanobis distance, which considers not only the group-average of all the sites but also the covariance structure of the attributes [Cunderlik and Burn, 2006]. Sites that fail the Hosking and Wallis [1997] discordancy test at the 10% confidence are removed from consideration.

Finally, the remaining stations are removed in order of their dissimilarity as measured above to ensure the total station-years is less than  $N_s$  and also that the region as a whole is homogeneous. Homogeneity is ensured following the methodology described by Viglione *et al.* [2007], where either the k-sample Anderson-Darling rank test or the Hosking and Wallis [1997]  $HW_1$  test is used depending on whether the regional L-coefficient of skewness is greater or smaller than 0.23, respectively. The Anderson-Darling test is based on comparing individual sites with regional empirical distributions. Significant heterogeneity in the region of influence is found by estimating the 0.05 level of significance by Monte Carlo simulations. The  $HW_1$  test compares the variability of L-moment ratios for the group of sites with the expected variability obtained from simulation and if  $HW_1 > 2$  then the region of influence is “definitely heterogeneous”. Sites are removed iteratively until either the region is found to be homogeneous or the total number of station-years does not drop below  $0.6 \times N_s$ . The

percentage of sites whose region of influence remained heterogeneous (in order to keep the number of station-years at an acceptable level) are shown in Table 4.

Once the region of influence has been established, regional L-moment ratios ( $\tau_2^R$  and  $\tau_3^R$ ) are found by taking the average over the individual sites weighted by an effective record length [Robson and Reed, 1999]. This can be expressed as

$$\tau_r^R = \frac{\sum_{i=1}^M w_i \tau_r^i}{\sum_{i=1}^M w_i}, \quad (r = 1, 2)$$

where  $M$  is the number of sites in the region of influence, and  $w_i$  is an effective record length at site  $i$ , defined by  $w_i = S_i n_i$ . Here,  $n_i$  is the actual record length and  $S_i$  is a similarity ranking factor given by

$$S_i = \frac{\sum_{j=i}^M n_j}{\sum_{j=1}^M n_j}.$$

Thus, the most-similar site has a similarity ranking factor of 1, while at the least-similar site  $S_M = n_M / (n_1 + \dots + n_M)$ .

**Table 4: Percentage of sites remaining heterogeneous following the Viglione homogeneity testing strategy.**

Duration	10m	20m	30m	1h	2h	6h	12h	1d	2d	3d	4d	5d
%	5.3	3.6	3.8	0.7	1.7	0.6	0.6	0.4	0.6	0.7	1.3	1.4

### 3.2.3 Frequency clustering over event durations

Frequency distributions, at a site or averaged over a region, fitted to data from different durations are not always consistent. For example, the 12-hour 100-year rainfall event could be smaller than the 6-hour, 100-year rainfall. To minimize this occurrence, *Durrans and Kirby* [2004] proposed a three-class data typing based on the duration of storm rainfalls; daily, hourly, and sub-hourly. This has some meteorological equivalence to synoptic (daily) and convective (sub-hourly) storm typing reflecting the dominant dynamic atmospheric processes associated with such rainfalls [Thompson, 2002]. However, the data-type for durations from 1 – 12 hours is likely to be a blend of both convective and synoptic scale processes as the storm dynamics transition from dominant convective processes to synoptic rainfall processes as duration increases.

More refined data-types have been used in this study by using hierarchical clustering of the regionalised L-moment ratios. Figure 6 shows the cluster tree derived using both  $\tau_2^R$  and  $\tau_3^R$  using only those sites which have data for all durations. This tree can be nicely divided into either two groups (durations up to and above 2 hours) or four groups (sub-hourly, hourly (1 & 2 hr), sub-daily (6 & 12 hr) and daily). The latter grouping seems most appropriate as it avoids combining durations that have quite different properties, i.e., 10 minutes with 2 hours or 6 hours with 5 days.

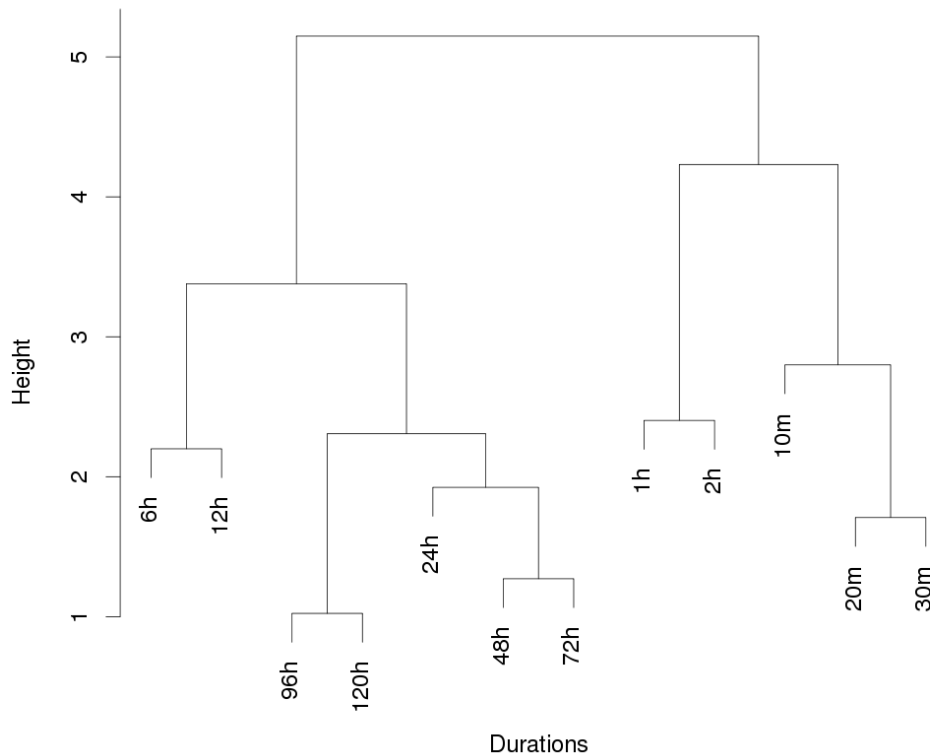


**Figure 6: Clustering tree based on regionalised L-moment ratios over the 12 event durations.**

*Durrans and Kirby* [2004] adjusted the L-moment ratios so that they would vary from site to site, but would remain constant across all durations with the given data-type, by computing averages of original L-moments for the constituent durations. To maintain consistency, the original second L-moment,  $\lambda_2$ , and the corresponding  $\mu$  and  $\sigma$  are adjusted to conform with the mean L-coefficient of variation,  $\tau_2$ , for the data-type.

### 3.2.4 Mapping the frequency variables

Surfaces of regional L-coefficient of variation ( $\tau_2^R$ ) and L-coefficient of skewness ( $\tau_3^R$ ) for each of the data-types were fitted using a common signal to error characteristic, and were mapped onto a 2 km by 2 km spot digital elevation model using the ANUSPLIN suite of programs. Maps of the spatial patterns for  $\tau_2^R$  and  $\tau_3^R$  are given in Figure 7 and Figure 8, respectively, for all the data-types.

Highest values of L-coefficient of variation are generally in eastern regions of New Zealand and the regional pattern is broadly similar for the different data types. For longer durations, the smallest values of L-coefficient of skewness (i.e., where the shape parameter tends also to be close to zero or positive) tend to be in the western and mountainous areas of New Zealand, while for short durations the lower values tend to be in the north of the North Island. These spatial patterns and the general increase in  $k$  with duration are consistent with findings made by *Pearson and Henderson* [1998] in an earlier New Zealand study into annual maximum frequency distributions.

The importance of separating the 1, 2, 6 and 12 hour durations from a single data type in HIRDSv3 to two separate types becomes apparent when examining the mapped frequency variables, in particular  $\tau_3^R$ , which is markedly different between the hourly and sub-daily data types.

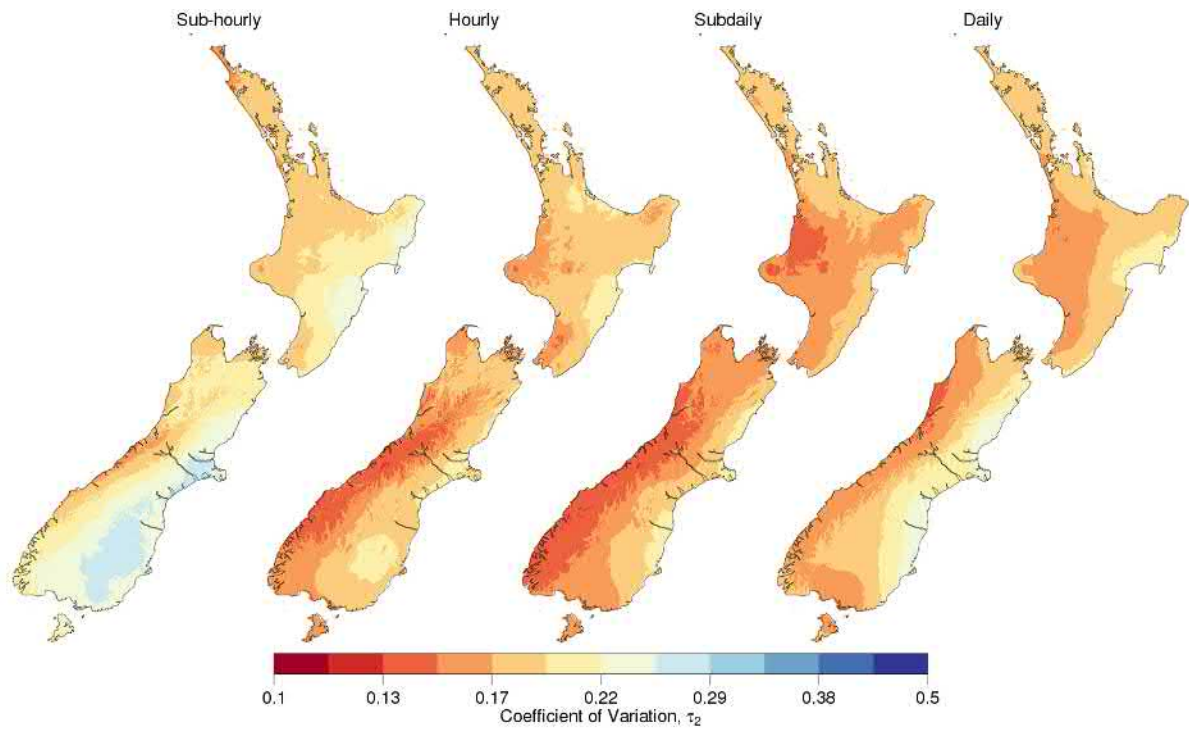


Figure 7: Spatial distribution of the L-coefficient of variation for the different data types used.

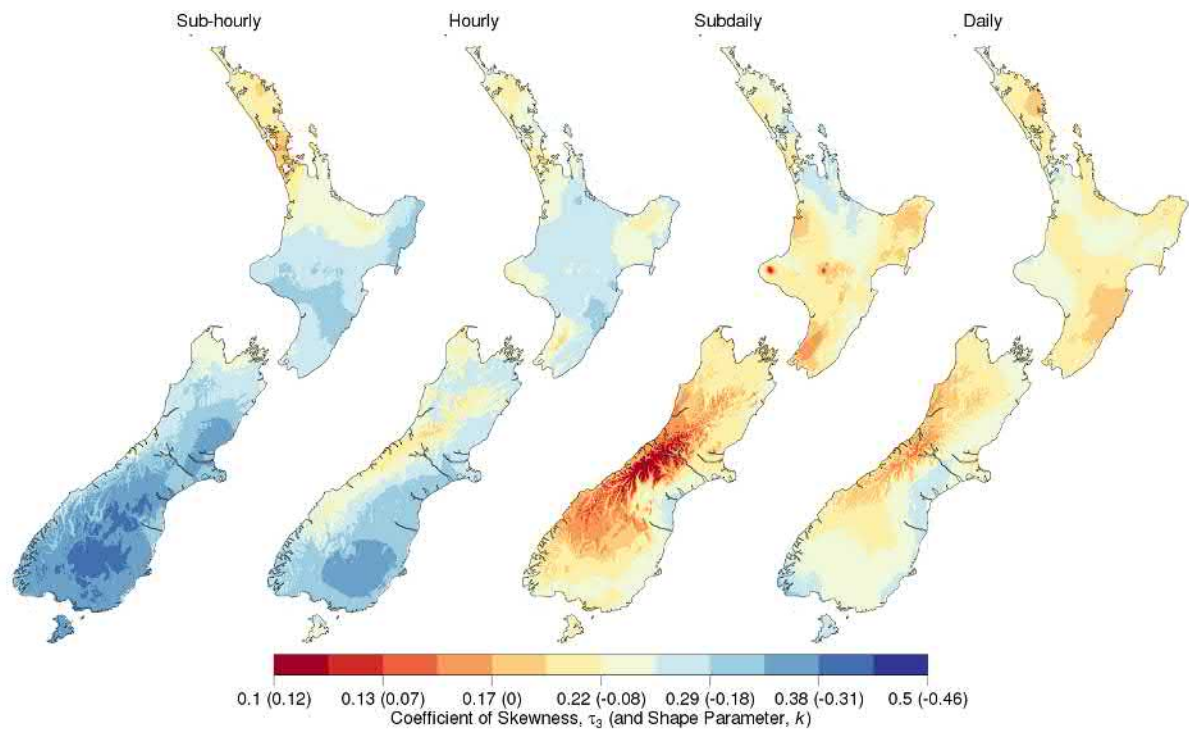


Figure 8: Spatial distribution of the L-coefficient of skewness for the different data types used. The equivalent GEV shape parameter,  $k$ , is also shown on the colour scale in brackets.



### 3.3 Depth-duration-frequency calculation

To derive depth-duration-frequency tables for a particular location, estimates of the magnitude and standard error of the rainfall index variable and the two growth curve parameters are needed. These are obtained from the mapped variables using bi-linear interpolation. Where the required location is within 2 km of a rainfall gauge, a weighted average of the mapped parameter and any gauge derived parameter is used for the final parameter estimate. The weights used are a combination of the inverse distance from the gauge to the point of interest and the inverse of the standard error. The combined weighting then accounts for both the quality of the record (mainly related to the record length) and the distance from the required location.

Given the median annual maximum rainfall,  $R_{MED}$ , and the two regional L-moment ratios  $\tau_2^R$  and  $\tau_3^R$ ,  $T$ -year rainfall depths for a range of storm durations can then be readily computed. The regional L-moment ratios derive the regional growth curve for a GEV frequency distribution. The shape parameter,  $k$ , is computed directly from its relationship with the L-coefficient of skewness,  $\tau_3$ , (see Equation (2)), while the scale and location parameters are given by

$$\sigma = \frac{\beta}{R_{MED}} \quad \text{and} \quad \mu = R_{MED} \left( 1 - \frac{\beta(1 - \ln(2))^k}{k} \right)$$

where  $\beta$  is given by *Robson and Reed* [1999] as

$$\beta = \frac{k\tau_2}{\tau_2(\Gamma(1+k) - \ln(2)^k) + \Gamma(1+k)(1 - 0.5^k)}$$

A depth-duration-frequency table (DDF), or equivalently an intensity-duration-frequency table (IDF), can be easily computed using the inverse of the cumulative density functions given in Equation (1), the quantile function

$$q(F) = \begin{cases} \mu + \frac{\sigma(1 - (-\ln F)^{-k})}{k}, & k \neq 0 \\ \mu - \sigma \ln(-\ln F), & k = 0 \end{cases}$$

The error estimates for the index variable and growth curve parameters are combined using a bootstrap approach to estimate the uncertainty for each rainfall depth in the DDF table. This bootstrap approach assumes that the errors in the three parameters are not strongly correlated with one another. In reality, the errors are likely to be somewhat correlated, so the final standard error estimates on the DDF tables may be slightly underestimated.

#### 3.3.1 Ensuring internal consistency

Despite using the index-frequency method to estimate tables of depth-duration-frequency, the tables can be internally inconsistent. When durations are treated separately, it is possible for “contradictions between rainfall events” [*Faulkner*, 1999] to occur between durations and recurrence intervals. Power laws of the form  $R = aD^b$ , where  $D$  is the duration,  $R$  is the rainfall depth or intensity and  $a$  and  $b$  are model coefficients, are commonly used to provide consistent tables. This was also done in the earlier versions of HIRDS.

*Faulkner* [1999] used a 6-coefficient flexible form of the power law relationship based on three concatenated line segments to allow the logarithmic relationship between duration and intensity to change with duration. HIRDSv3 used a modified 8-coefficient version of this relationship to allow for additional flexibility [*Thompson*, 2011]. For this study, the *Faulkner* [1999] model has been modified

in a different way to allow for additional flexibility in the frequency dimension and remove the need for segmentation. To do this the relationship between intensity and the Gumbel reduced variate has been modelled using a second order polynomial instead of a linear model and the three separate linear segments used to model the intensity-duration relationship have been replaced with a third order polynomial.

This alteration means the model is now fitted to all durations simultaneously and removes the complication of requiring an intercept for each segment.

The full DDF model is defined as

$$\ln R = cxy + dx + ex^2 + fx^3 + gy + hy^2 + i \quad (3)$$

where  $y$  is the Gumbel reduced variate

$$y = -\ln\left(-\ln\left(1 - \frac{1}{ARI}\right)\right)$$

and  $x = \ln D$ .  $D$  is the duration in hours,  $ARI$  is in years and  $R$  is the rainfall depth in mm. The seven parameters  $c$  through  $i$  are fitted using weighted linear least squares. The effective lengths of the annual maxima time-series at each duration are used for the weights. This means that the final DDF model should not be negatively affected by poor estimates at certain durations, for example near sites with long daily, but sparse sub-daily, records.

The addition of the third order polynomial allows for an improved fit over using individual segments, however if left unconstrained can cause issues when the input depth-duration-frequency values are not smoothly varying. For this study,  $f$  has been constrained to be in the range  $(-0.0065, 0)$ . Limiting the parameter to be negative means there is no positive inflection for the longer durations. Cases where a positive value provides a better fit were those with intermediate duration (sub-daily) intensities that were unrealistically low. Large negative values for  $f$  produce too much curvature at longer durations and can result in inconsistencies where for large return periods, intensities are not strictly increasing with increasing duration. The lower limit of  $-0.0065$  was chosen after fitting the unconstrained model to all points over New Zealand and finding that all inconsistencies occurred when  $f < -0.007$ . Both the lower and upper constraints come into effect in approximately 20% of cases.

Figure 9 contains rainfall depths plotted against duration for a location in Mount Aspiring National Park at a selection of return periods. For this location, there are some discontinuities arising at the boundaries of the different groups of durations, particularly for the longer return period events. The different colour curves show the three-segment *Faulkner* [1999] model (red) and the third-order polynomial model used in this report (blue). It is clear that the polynomial model provides a closer fit to the data especially at longer durations.

The two main improvements of this model over the earlier versions are firstly the more flexible intensity-frequency relation which reduces errors particularly for very low and very high frequency events (i.e., 2-year and 250-year return period events). Secondly, by fitting the full model simultaneously, biases are reduced and more evenly spread across the durations. In the *Faulkner* [1999] model, the intercept is derived from the linear model fitted to only the first segment, so the error tends to increase in the second and third segments. The reduction in bias from the three-segment model to the polynomial model is shown in Figure 10.

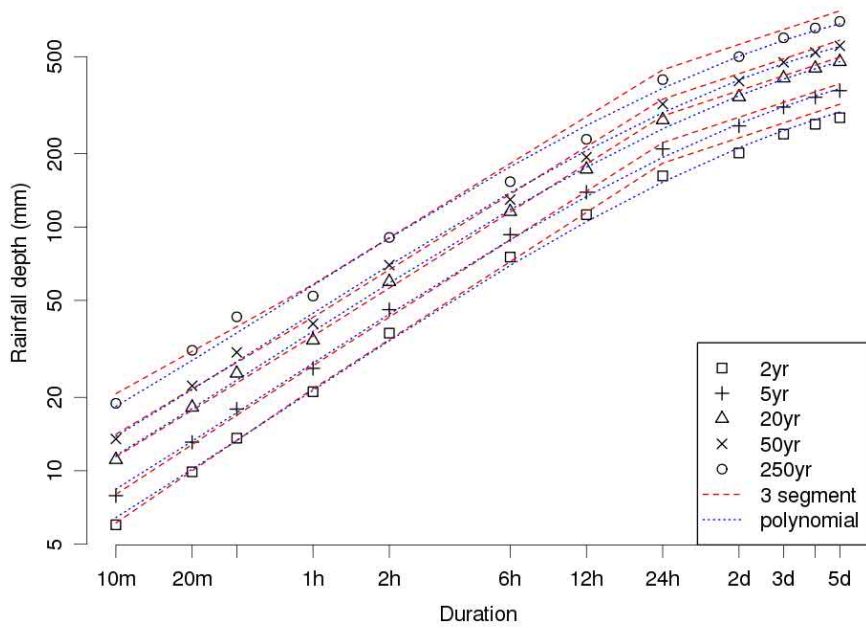


Figure 9: Example design rainfalls showing two different DDF models fitted to the data.

**Mean error of DDF model over all durations/frequencies**

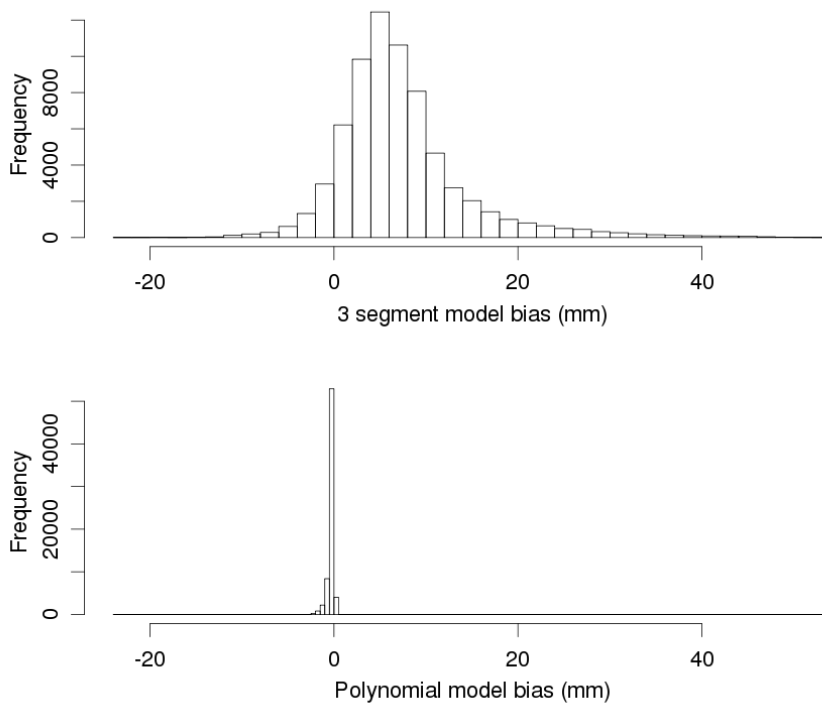
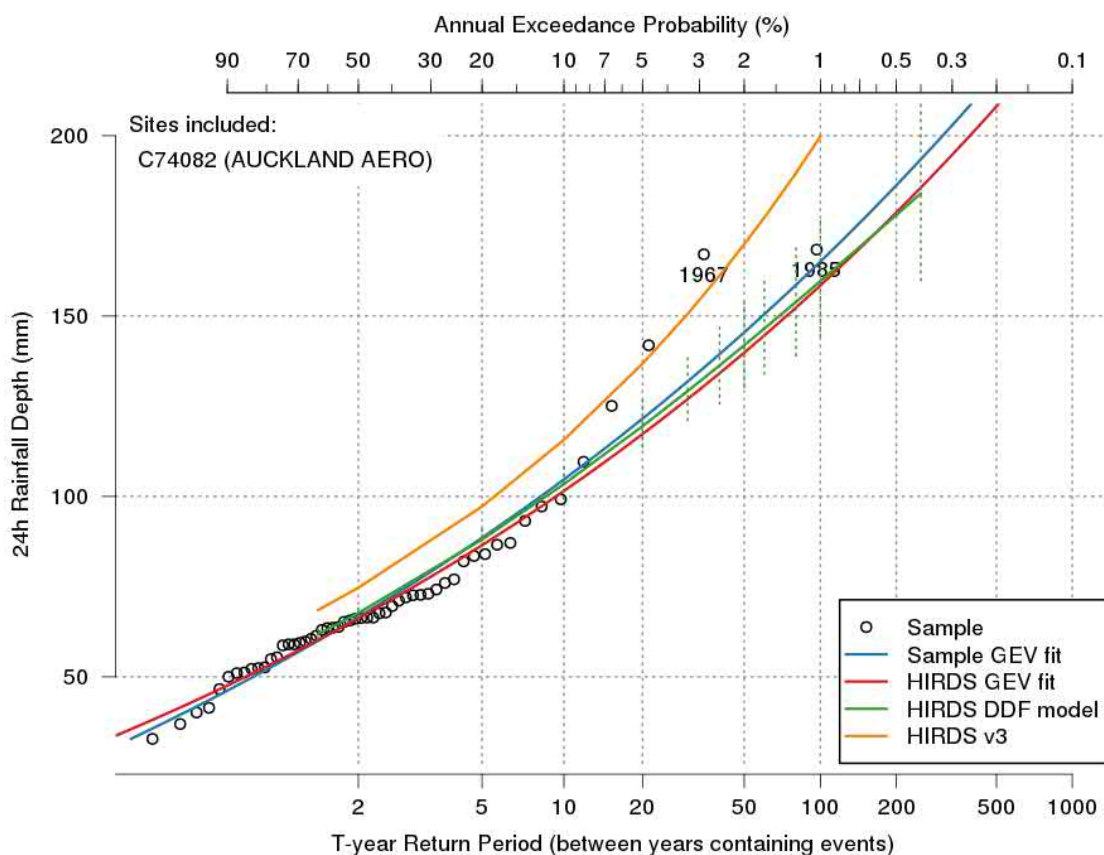


Figure 10: Mean error of the depth-duration-frequency model over all standard durations and frequencies. Each histogram includes all points in the 2 km digital elevation model.

### 3.4 Example results and comparison with HIRDSv3

For illustrative purposes, a 24-hr duration growth curve for a gauge with a relatively long record length of 54 years is provided in Figure 11. Annual maximum rainfall depth for Auckland Airport is plotted along with fitted GEV distributions at various stages in the HIRDS analysis. The fit after regionalisation (red line) is slightly different from the GEV fitted directly to the data (blue line) as it includes information from surrounding sites. For gauges with shorter record lengths, the difference between these two curves can be significantly larger. After applying the DDF model described in the previous section the curve (green line) is slightly different again as it has been adjusted to improve the continuity between different event durations. For reference, the result obtained using the previous version of the HIRDS tool is also shown (orange line).

Figure 12 contains a map of the 100-year, 24-hour duration event magnitude and its associated standard error. The most extreme events occur in areas of high elevation, but there are also regions over Tasman, Coromandel and East Cape that have relatively high event magnitudes. The smallest 1-day events occur in the south-east of the South Island (Canterbury, Otago and Southland) and also in the Manawatu region, inland from Whanganui. The standard error generally follows the same pattern as the event magnitude, with the largest errors in those places with the heaviest rainfall. Estimates of the standard error are generally lower in the vicinity of rainfall gauge locations.



**Figure 11: Example 24-hr duration HIRDS growth curve for Auckland Airport. Observed annual maxima are shown as black circles while the blue line shows a GEV distribution fitted directly to this data. The GEV fitted using regional frequency analysis is shown in red. The final HIRDS result following application of the DDF model is shown by the green line. The orange line shows the HIRDS version 3 result.**

The standard error expressed as a percentage of the rainfall depth for a selection of durations and return periods is shown in Figure 13. As expected, this figure shows that the relative error increases with return period; that is the uncertainty grows faster than the expected depth with increasing rarity. These maps also show that even though the largest absolute errors are collocated with the largest rainfall depths (refer Figure 12), the relative errors are actually lower in those regions with the largest rainfall depths, particularly for longer durations. This is likely to be due to the strong forcings (e.g.; topographic) in those regions providing more predictable or consistent extreme rainfall depths.

Another point of interest is that the shortest duration events generally have the largest relative error, especially for low frequency events. This is likely to be a result of the greater paucity of sub-hourly data, but also may be due to the larger variability of short duration events. Further work is needed to understand some aspects of these error patterns, such as the relatively high uncertainty in Otago/Southland for the longer duration events.

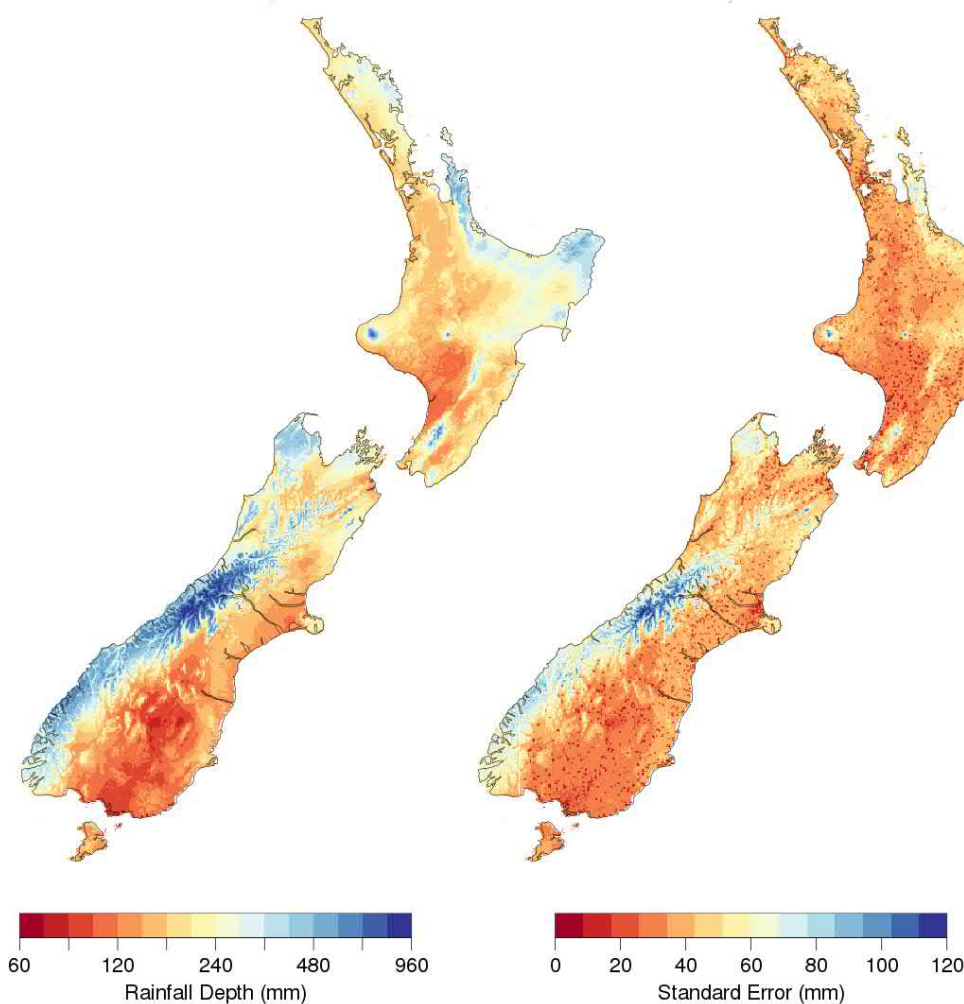


**Figure 12: Rainfall depth and standard error for a 24-hour duration event with a 100-year recurrence interval. Depth is shown on the left using a logarithmic scale, while standard error is shown on the right using a linear scale.**

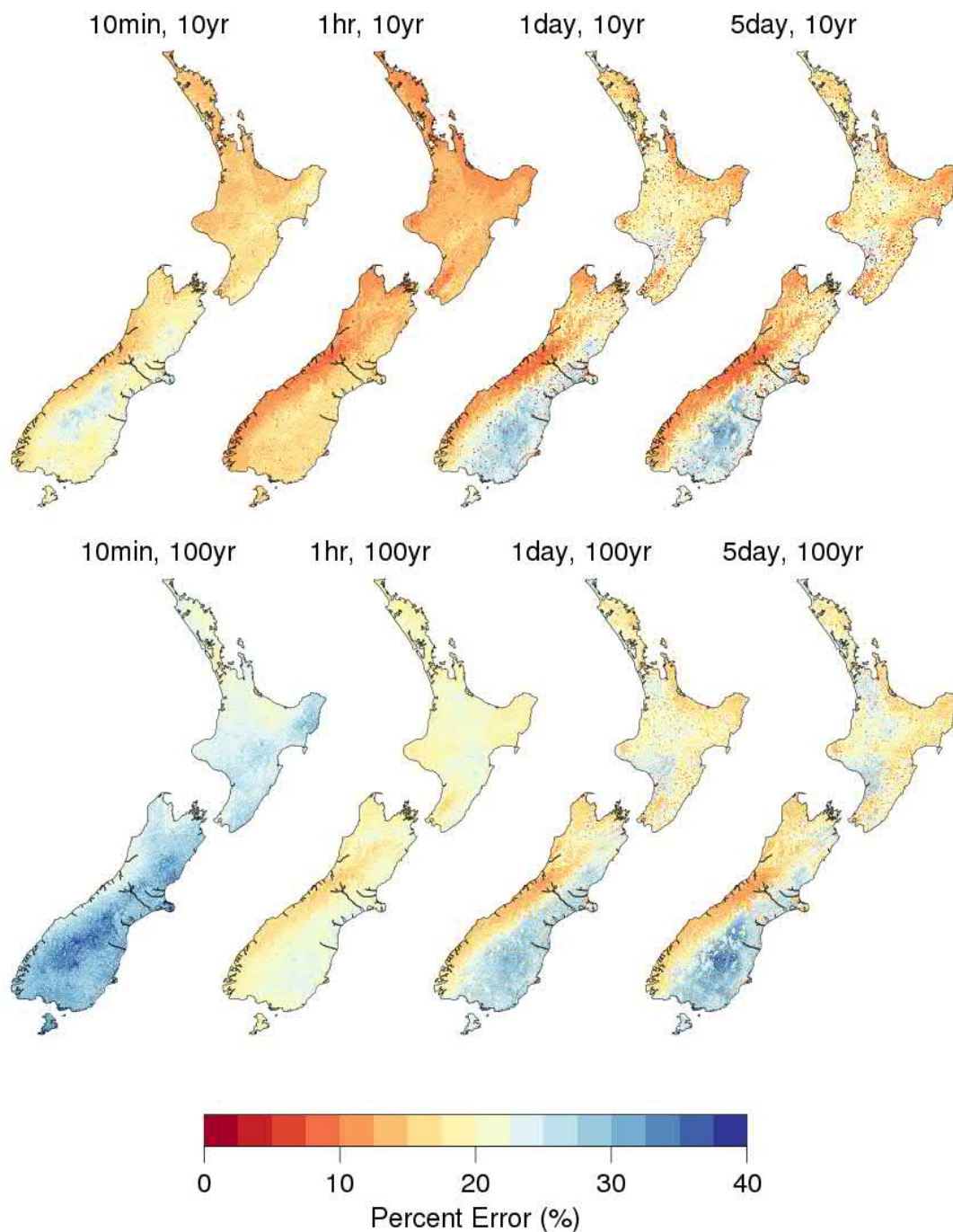


**Figure 13: The percent standard error in rainfall depth for 10- and 100-year recurrence intervals for a selection of event durations.**

Depending on location, there can be considerable differences between this analysis and the 2011 HIRDSv3. An example of this difference is shown in Figure 11 and a spatial comparison for the 100-year, 2-hour duration event is shown in Figure 14. The general spatial pattern is consistent between versions, however there are clear differences, most notably the increase in spatial detail derived from the underlying digital elevation model. In regions where the observation network is sparse, the spline mapping algorithm relies more heavily on the topography to estimate the index variable

(median annual maximum). Other differences that are observed, for example southern Fiordland where the hourly observations have nearly doubled in length, are mostly due to additional observations.

The percentage difference between HIRDSv3 and HIRDSv4 for three different event durations is shown in Figure 15 for a 100-year recurrence interval. The central panel is the percentage difference between the two maps shown in Figure 14. For all durations, the change from version 3 can be either positive or negative and is quite variable, that is a blanket statement such as “HIRDSv4 produces larger rainfall depths than HIRDSv3” cannot be given. The largest differences are either seen in the sub-daily durations (due to additional observations) or in regions of complex topography.

For all durations, the largest increases in depth are generally seen in high elevation areas of the South Island. When increases are seen in other parts of the country they are generally moderate and typically less than 15%.

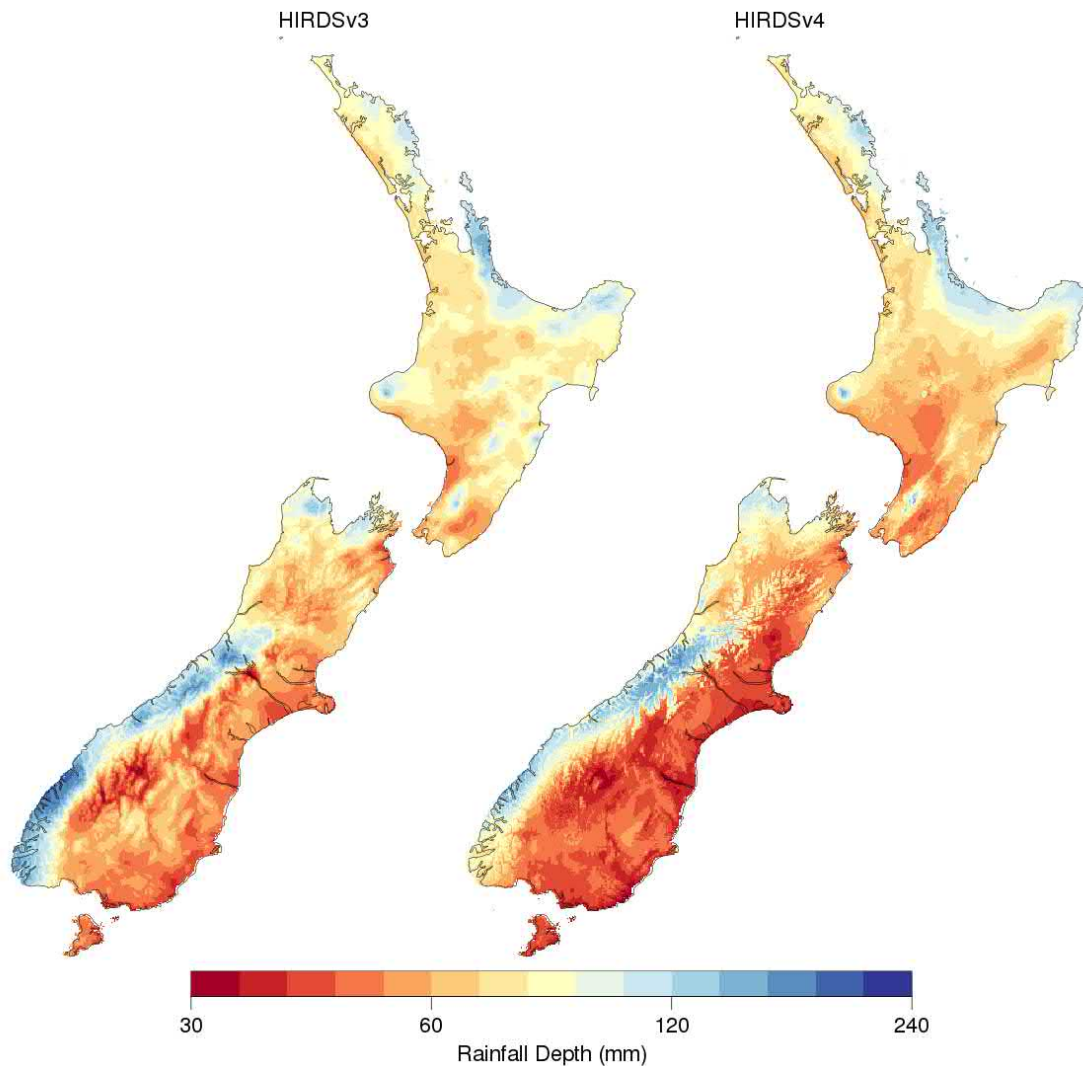


**Figure 14: Rainfall depth for a 2-hour duration event with a 100-year recurrence interval. Results from the previous version of HIRDS are shown on the left and the current analysis is on the right.**

Decreases in rainfall depth can be quite large even when not associated with complex terrain. For sub-hourly durations, the largest decreases are in central areas of the North Island and the Gisborne region. For 1 and 2-hour durations, there is a reasonably consistent decrease in rainfall depth in the lower North Island and both the east and south of the South Island. For daily durations, the largest differences are in regions of complex topography and there is a tendency for much of the North Island to have lower rainfall depths.

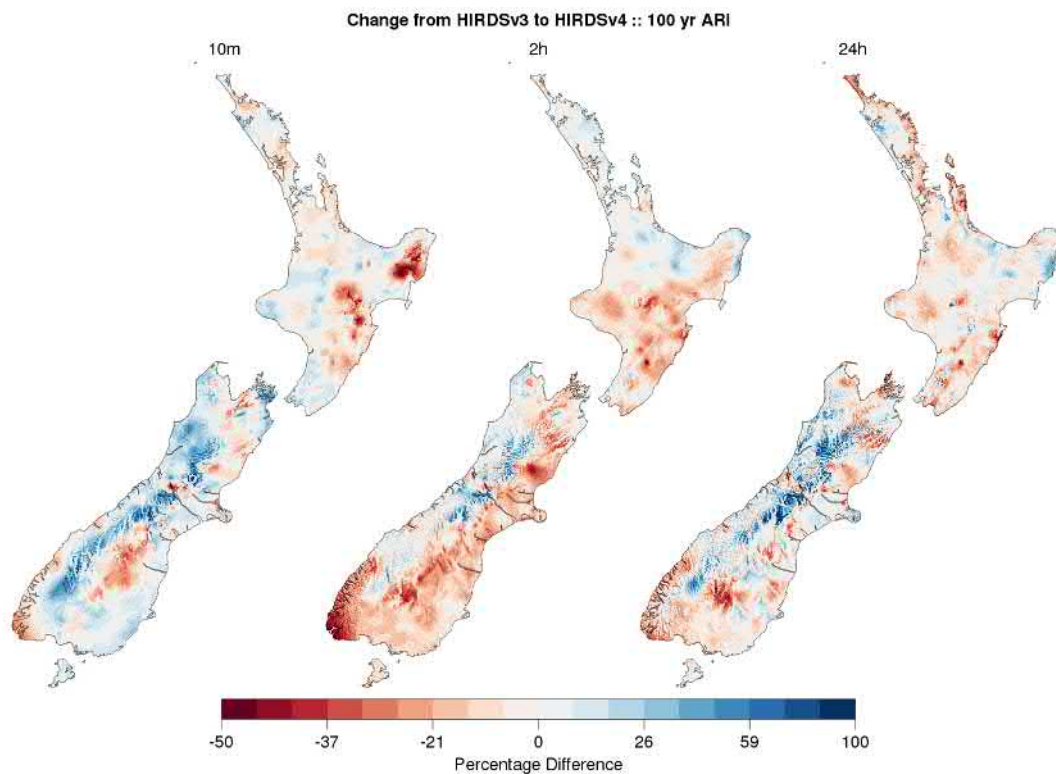


**Figure 15: Difference in rainfall depth between the previous version of HIRDS and the current analysis for a 100-year recurrence interval. The percentage difference (relative to HIRDSv3) is shown for three different event durations.**

An overview of the range of depths across different durations and with different return periods can be seen in Figure 16. While this figure is too broad to be useful for individual durations, frequencies or locations, it does show the generally monotonic increase in rainfall depth with both duration and return period. This is valuable information to check that both the mapping of the index variable at different durations and the combining of different durations into data types for the mapping of the frequency variables has not introduced inconsistencies. In addition, the smooth increase in rainfall depth from the 5-year to 250-year return period shows that the fitted growth curves are performing sensibly.



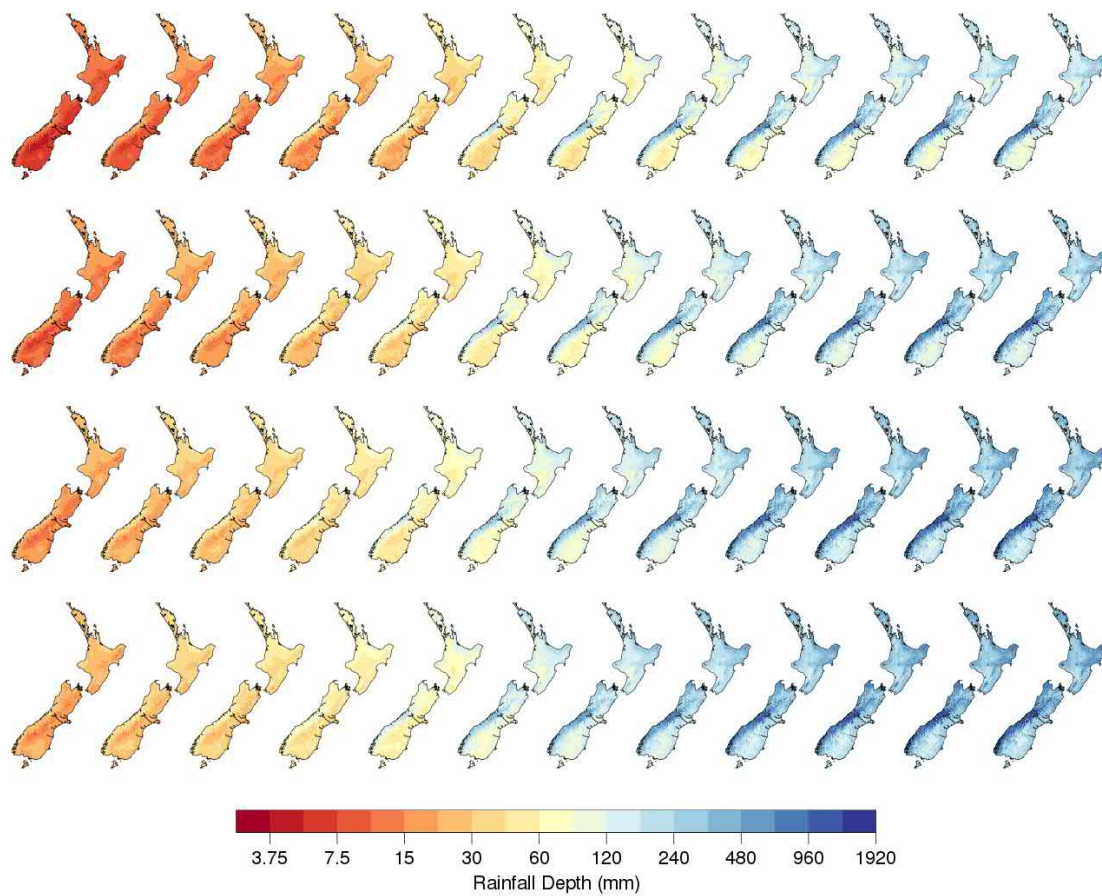


**Figure 16: Rainfall depths for all standard durations and for four different average recurrence intervals. The top row displays rainfall depths for a 5 year recurrence interval, the next row for 20 year, the third row for 100 year and the bottom row a 250 year recurrence interval. The 12 durations are shown from left to right; 10, 20 and 30 minute; 1, 2, 6 and 12 hour; and 1, 2, 3, 4 and 5 day.**

## 4 Climate change response

It is generally accepted that precipitation extremes will increase in intensity due to climate change [Fischer and Knutti, 2016; Trenberth, 1999]. This general increase is due to the Clausius-Clapeyron (C-C) relation, which states that the amount of precipitable water the atmosphere can hold increases by approximately 7% per degree of warming. However, an increasing amount of research has shown that there are additional processes impacting on precipitation extremes that also need to be taken into account. These include changes in dynamic processes such as vertical velocity [Pfahl et al., 2017] which can lead to the intensification of short duration convective storms [Feng et al., 2016; Prein et al., 2017]. In the mid-latitudes, changes in precipitation intensity can be up to twice the C-C relationship for the most extreme events, i.e., the increase in intensity may be up to 14% per degree of warming [Lenderink and Fowler, 2017].

In the New Zealand context, Griffiths [2007; 2013] looked at trends in observed extreme precipitation indices, but found little statistical significance or obvious regional trends. Carey-Smith et al. [2010] used regional and global climate model simulations to test the validity of the C-C relation over New Zealand and using the limited simulations available at the time found the change in extreme precipitation to range between 5 and 12% per degree of regional warming. A study by Graham et al. [2016] using the same generation of climate models described below found that the intensity of events with a peak precipitation rate greater than 2 mm/hr increased between 9 and 21% by the end of this century. The previous version of HIRDS used the extreme precipitation climate change factors from the 2007 Ministry for the Environment guidance manual which are shown in Table 5 [Mullan et al., 2007].

**Table 5: Factors used by HIRDSv3 for deriving extreme rainfall intensities from current intensity estimates and an expected temperature change [Mullan et al., 2007].**

Duration/ARI	2 yr	5 yr	10 yr	20 yr	30 yr	50 yr	100 yr
10 minutes	8.0	8.0	8.0	8.0	8.0	8.0	8.0
30 minutes	7.2	7.4	7.6	7.8	8.0	8.0	8.0
1 hour	6.7	7.1	7.4	7.7	8.0	8.0	8.0
2 hours	6.2	6.7	7.2	7.6	8.0	8.0	8.0
6 hours	5.3	6.1	6.8	7.4	8.0	8.0	8.0
12 hours	4.8	5.8	6.5	7.3	8.0	8.0	8.0
24 hours	4.3	5.4	6.3	7.2	8.0	8.0	8.0
48 hours	3.8	5.0	6.1	7.1	7.8	8.0	8.0
72 hours	3.5	4.8	5.9	7.0	7.7	8.0	8.0

Due to the increase in availability of regional climate change information and advances in extreme precipitation research, this HIRDS release provides an updated set of augmentation factors. These factors for precipitation extremes have again been given as a percent change per degree of warming but can be converted to fixed percent changes for different future time periods and climate change scenarios (RCPs) by multiplying the augmentation factors by the relevant temperature change. This augments the approach taken by the recent Ministry for the Environment report on climate change projections for New Zealand [Mullan et al., 2016] which limited its discussion of precipitation

extremes to changes in the 99<sup>th</sup> percentile of daily precipitation, finding a systematic increase in much of the South Island, with both time and increasing greenhouse gas concentration, and a more varied signal in the North Island.

#### 4.1 Climate scenarios

This study considers changes in future extreme rainfall using four concentration pathways from the Intergovernmental Panel on Climate Change (IPCC) Fifth Assessment [IPCC, 2014]. The pathways are known as representative concentration pathways (RCPs), and abbreviated as RCP2.6, RCP4.5, RCP6.0, and RCP8.5, in order of increasing radiative forcing by greenhouse gases. These pathways are identified by their approximate total (accumulated) radiative forcing at 2100 relative to 1750 (i.e., RCP2.6 has a total radiative forcing of approximately 2.6 W m<sup>-2</sup>).

Global climate models (GCMs) are used to make future climate change projections for each of these future scenarios and results from these are available through the Coupled Model Inter-comparison Project (CMIP5). Six GCMs were selected by NIWA for dynamical downscaling using the UK Met Office HadRM3P model; that is, sea surface temperatures from six global climate models are used to drive an atmospheric global model, which in turn drives a higher resolution regional climate model (RCM) over New Zealand. The six models chosen were those which validated well on the present climate, and were as varied as possible in the parent global model to span the likely range of model sensitivity [Mullan *et al.*, 2016].

The six GCMs chosen for dynamical downscaling were BCC-CSM1.1, CESM1-CAM5, GFDL-CM3, GISS-EL-R, HadGEM2-ES and NorESM1-M and all simulations provided hourly precipitation from 1970 through to 2100. The native resolution of the RCM is 27 km and there are known biases in the precipitation fields derived from this model. While there exists a bias corrected version of this data at 5 km resolution, this has not been used for this study as the bias correction methodology excludes the most extreme events from its adjustment and does not provide sub-daily information. For this study, only relative changes in extreme precipitation within a particular simulation are assessed and used, so the effect of biases in absolute values of precipitation are minimised.

#### 4.2 Analysis of RCM extreme precipitation

The impact of climate change on extreme precipitation was assessed using RCM simulations spanning from 1971 to 2100. For each RCM simulation, hourly estimates of precipitation were used to calculate annual maxima series for all standard durations (1 hour through 5 day) at each model grid square. The generalised extreme value (GEV) distribution was then fitted to the annual maxima series at each grid square separately.

When an annual maxima series covers a time period that is non-stationary (e.g., during climate change), the parameters of the fitted GEV distribution may vary with time. In the case of extreme precipitation, it is expected that the location and shape parameters will vary (to first order) as a function of temperature. If this is the case,  $\mu$  and  $\sigma$  can be replaced in the Equation (1) with an expected value and a trend component, that is  $\mu = \mu_0 + \mu_1 T$  and  $\sigma = \sigma_0 + \sigma_1 T$  where  $T$  in this study is the annual average temperature anomaly for the given year of the annual maxima series. For this analysis, the non-stationary GEV distribution has been fitted using the *extRemes* software package [Gilleland and Katz, 2016].

The temperature variable used as the covariate for this trend analysis was each RCM's land-average annual temperature anomaly (relative to 1986-2005) as shown in Figure 17.

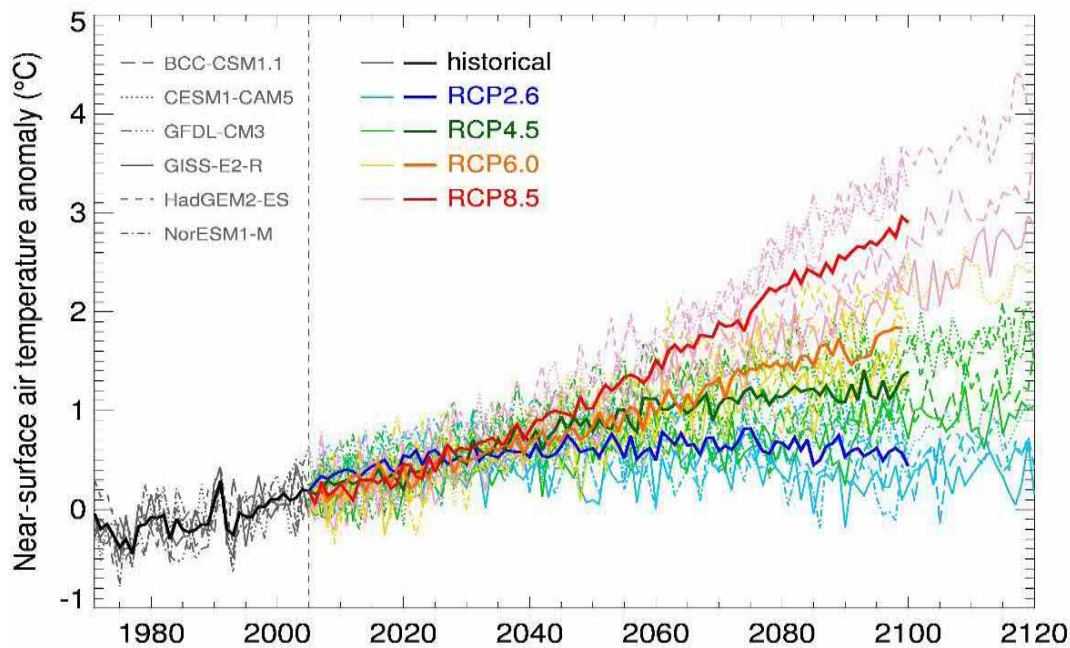


**Figure 17: Projected New Zealand-average temperatures relative to 1986-2005 for six CMIP5 global climate models downscaled via NIWA's RCM. Historical simulations (here 1971-2005) and four future simulations (RCPs 2.6, 4.5, 6.0 and 8.5) are included [Mullan et al., 2016].**

The non-stationary GEV can be fitted individually to each grid point for each RCM simulated annual maxima series. An example of how the rainfall event depth varies with temperature anomaly is shown in Figure 18 which contains the 24-hour annual maxima series for two simulations at a grid-point near Dunedin. Also included on these plots is the event magnitudes for three different return periods estimated from the non-stationary GEV distribution. The RCP2.6 simulation (left-hand image) shows very little trend with time, although the rainfall magnitudes are generally larger near the middle of the time period which matches the general temperature anomaly curve for RCP2.6 in Figure 17. An increasing trend is much more apparent in the right-hand image (RCP8.5) and this trend clearly follows the RCP8.5 temperature anomaly.

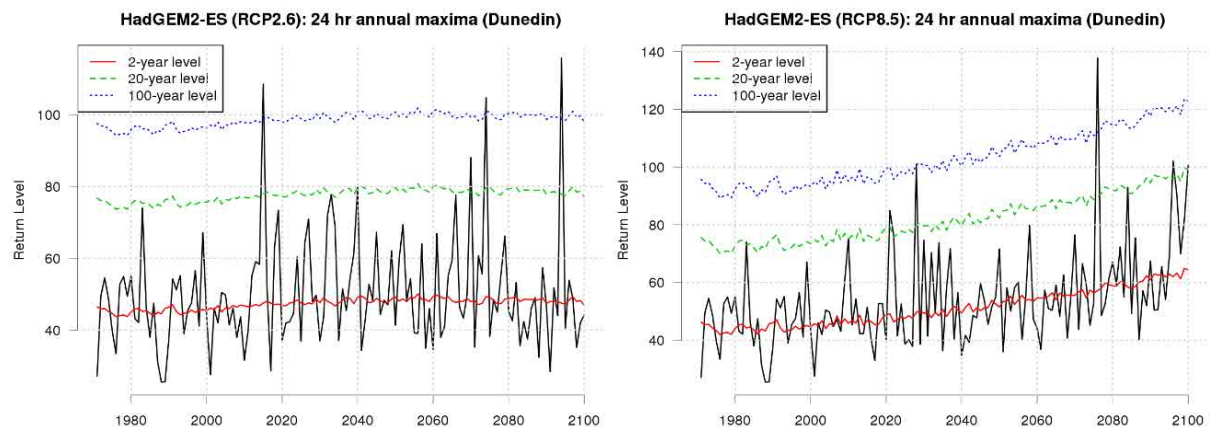


**Figure 18: The 24-hour annual maxima series at a point near Dunedin for two RCM simulations driven by the HadGEM2-ES global CMIP5 model (black lines). RCP2.6 (left) and RCP8.5 (right) are included for comparison. Event magnitudes for three different return periods derived from a non-stationary GEV fit to the data are shown in the coloured lines.**

Because the temperature anomaly is used as the covariate it means that the changes in extreme rainfall derived from the non-stationary GEV can be expressed as changes per degree of warming. Additionally, the trend in the  $\mu$  and  $\sigma$  parameters is expected to be the same for all RCP scenarios because it is expressed as a function of temperature anomaly. This is illustrated in Figure 19 which shows the trends fitted at each RCM grid point over New Zealand. Each histogram shows the trend derived from the GEV distribution fitted to annual maxima from all 6 GCM models together. It is clear that the estimated trends are consistent over all the RCPs. The main differences can be observed in the  $\sigma$  trend for which the distribution is wider for the lower RCPs (particularly RCP2.6 but also RCP4.5) compared with RCP6.0 and RCP8.5. This is due to the much weaker temperature anomaly signal in RCP2.6, meaning it is more difficult to obtain a clear trend.

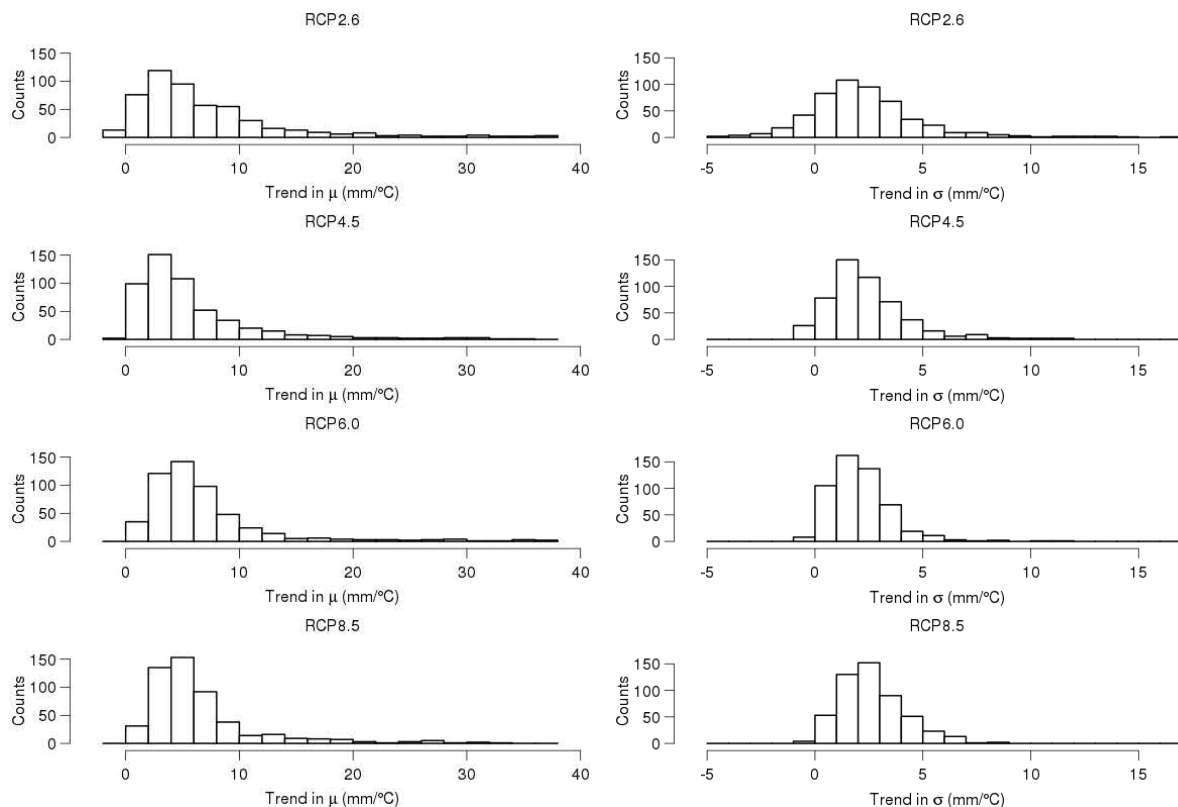


**Figure 19: Distributions of  $\mu$  (left) and  $\sigma$  (right) trends over all RCM land points for 4 different RCPs. Each histogram includes all six CMIP5 GCMs.**

Given that these trends are consistent between scenarios, the four RCPs can be combined and a single non-stationary GEV distribution fitted to the combined series. For each GCM driving model this includes a 35-year historical period (1971–2005) and four 95-year future periods (2006–2100) providing a combined annual maxima series of 415 years. All years in this series are independent and each has an associated temperature anomaly relative to 1986–2005. Analysis was done in this way to compare the regional structure obtained from each GCM (see next section).

For the final analysis, all 24 RCM simulations were combined to obtain the most robust GEV parameter estimates for all available event durations. All maxima values in this final series are not totally independent as the historical period for the six GCMs was forced by the same observed sea

surface temperatures. However, the “weather” in each GCM simulation was not constrained so these series are effectively independent for the purposes of this study.

Once fitted, both for the individual GCMs and all models combined, the GEV parameters can be used to calculate depth-duration-frequency tables at each grid square for the current climate and a future climate with one degree of warming. The percentage difference per degree of warming between the current and a future climate period can then be estimated.

### 4.3 RCM results

Despite the known biases in RCM precipitation, there is a high degree of similarity between the HIRDS derived rainfall depth surfaces and those derived from the climate model simulations. The 24-hour, 100-year event magnitude derived from all RCM simulations combined is shown in Figure 20, which uses the same colour scale as Figure 12 for ease of comparison. Due to the coarse resolution of the RCM, the largest rainfall depths estimated for the 1985-2005 period do not reach the same magnitudes as those from the HIRDS analysis, however the spatial characteristics are broadly consistent. Two maps based on future warming of 1 and 2.6 degrees are also shown.

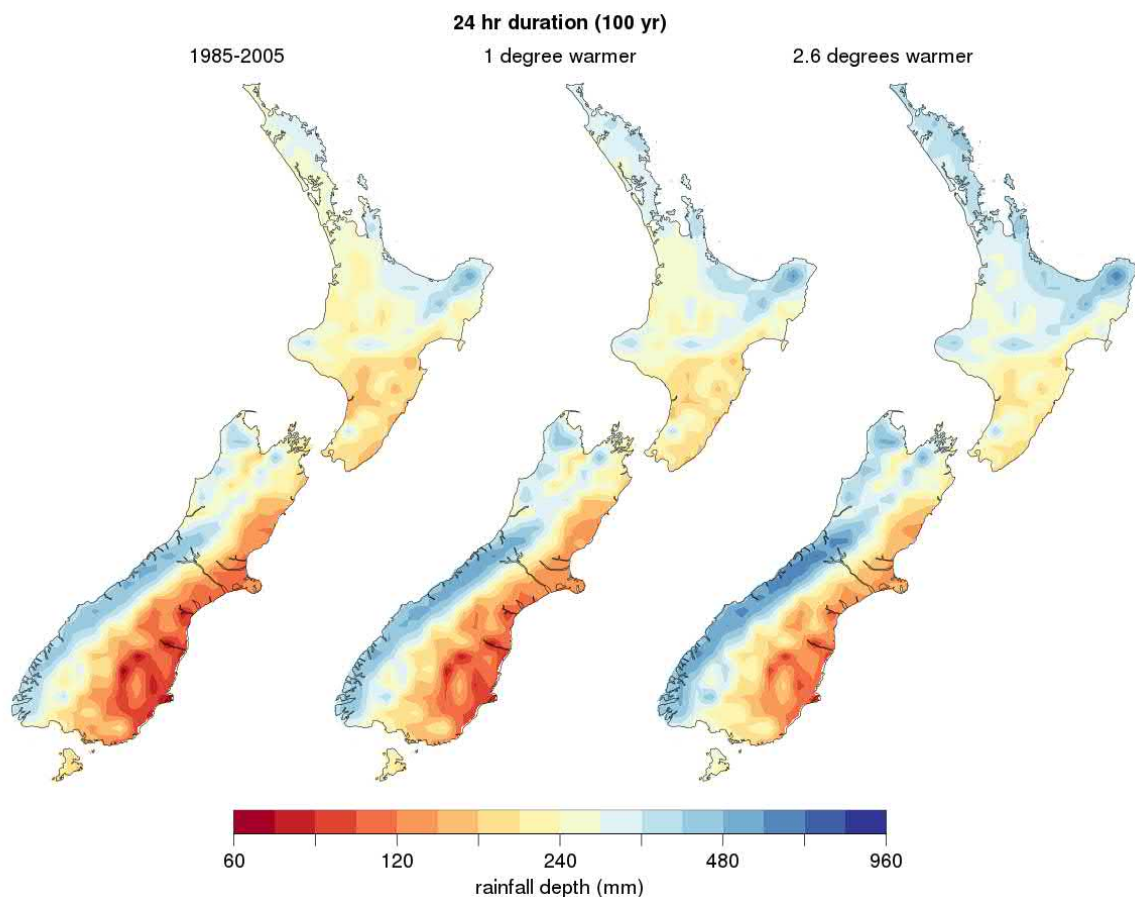


**Figure 20: The RCM derived 100-year event magnitude of a 24-hour duration event. Each map is a multi-model mean over 24 separate RCM simulations. The results based on the current climate (1985—2005) are shown on the left while the centre and right maps show projections based on the 1 and 2.6 degrees of warming. These latter two images (and most other images in this section) are not associated with a particular future period, rather they show results associated with a particular temperature change. This has been done to reduce the complexity that comes when dealing with multiple possible emissions scenarios.**

These future spatial patterns are also consistent with the HIRDS analysis and while on this logarithmic scale the differences appear small, the depths generally increase with temperature. However, the *changes* in rainfall depth due to climate change show regional patterns that vary considerably depending on the driving model. This is because the 24 different RCM simulations (6 driving models by 4 RCPs) have boundary conditions that come from different global climate simulations, and therefore, they each have different extreme events that occur at different times.

This can be observed in Figure 21, which shows percentage changes in rainfall depth per degree of warming for each RCM simulation. These maps show that increases in rainfall depth are more common than decreases (particularly for RCP8.5), but the spatial pattern of these changes is very different for the different simulations. Not only are the spatial patterns different between the 6 different driving models, but they also vary across the different RCPs for the same model.

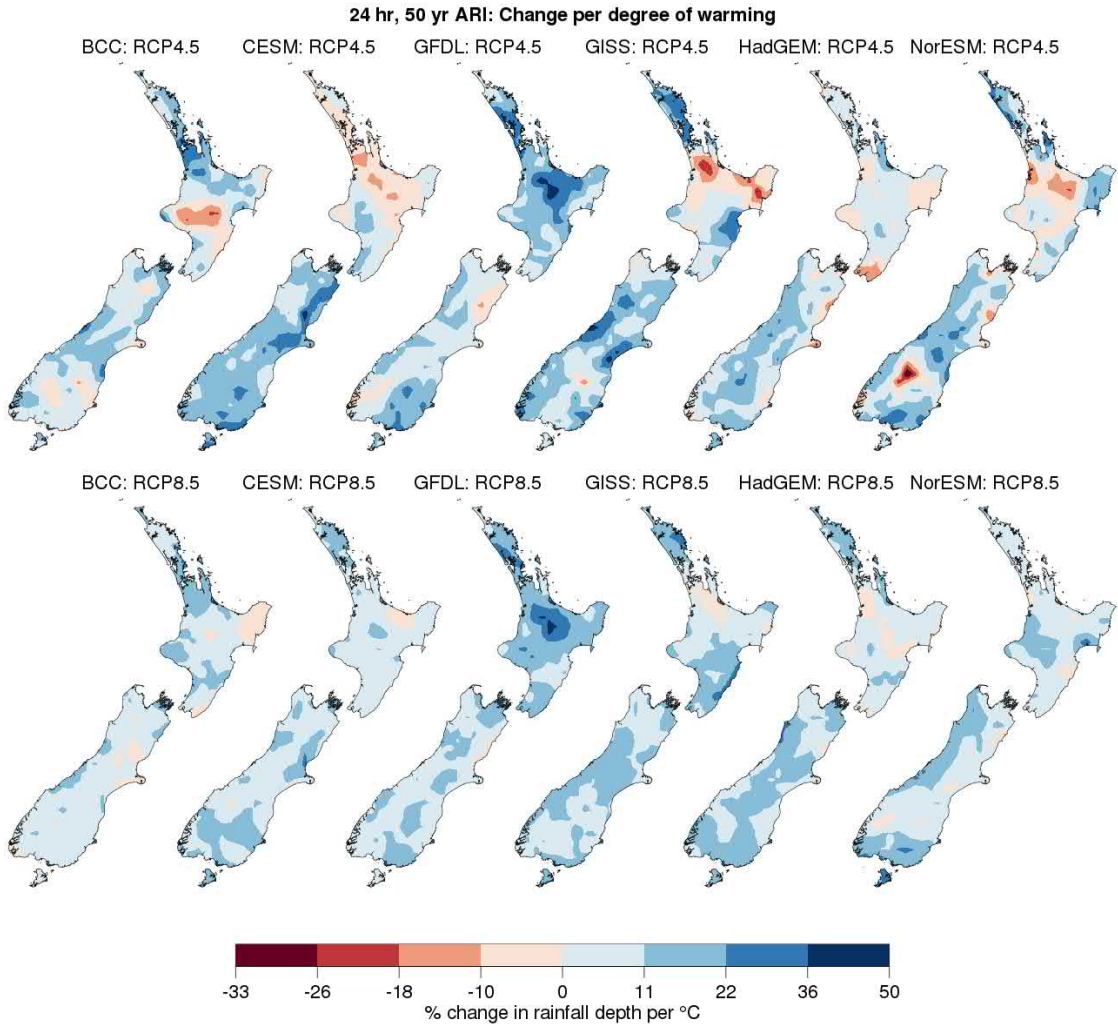


**Figure 21: Percentage changes per degree of warming in the 24-hour duration, 50-year event magnitude for each individual model simulation. The top row shows the change based on the RCP4.5 emissions scenario and the lower row shows the change based on the RCP8.5 scenario.**

Some of this variability can be reduced by combining the different RCP simulations for each of the 6 different driving models to create a 415-year series as described in the previous section. As shown in Figure 22, the increase in rainfall depth is now clearer, especially for short duration events, and the differences between the six GCMs have become less apparent. For the 1-hour event duration, the

changes are all positive and for the 5-day duration there are only some small regions where the rainfall depth decreases. However, the spatial patterns are still quite variable.

What this figure suggests is that there appears to be no clear regional pattern to the percentage change in extreme precipitation, regardless of the event duration. That there are no regions of New Zealand with a clearly different trend from anywhere else suggests that, given the available RCM projections, it is appropriate to use a uniform estimate of the percentage increase in precipitation per degree of warming (for each event duration and return period) to be used over the whole country.

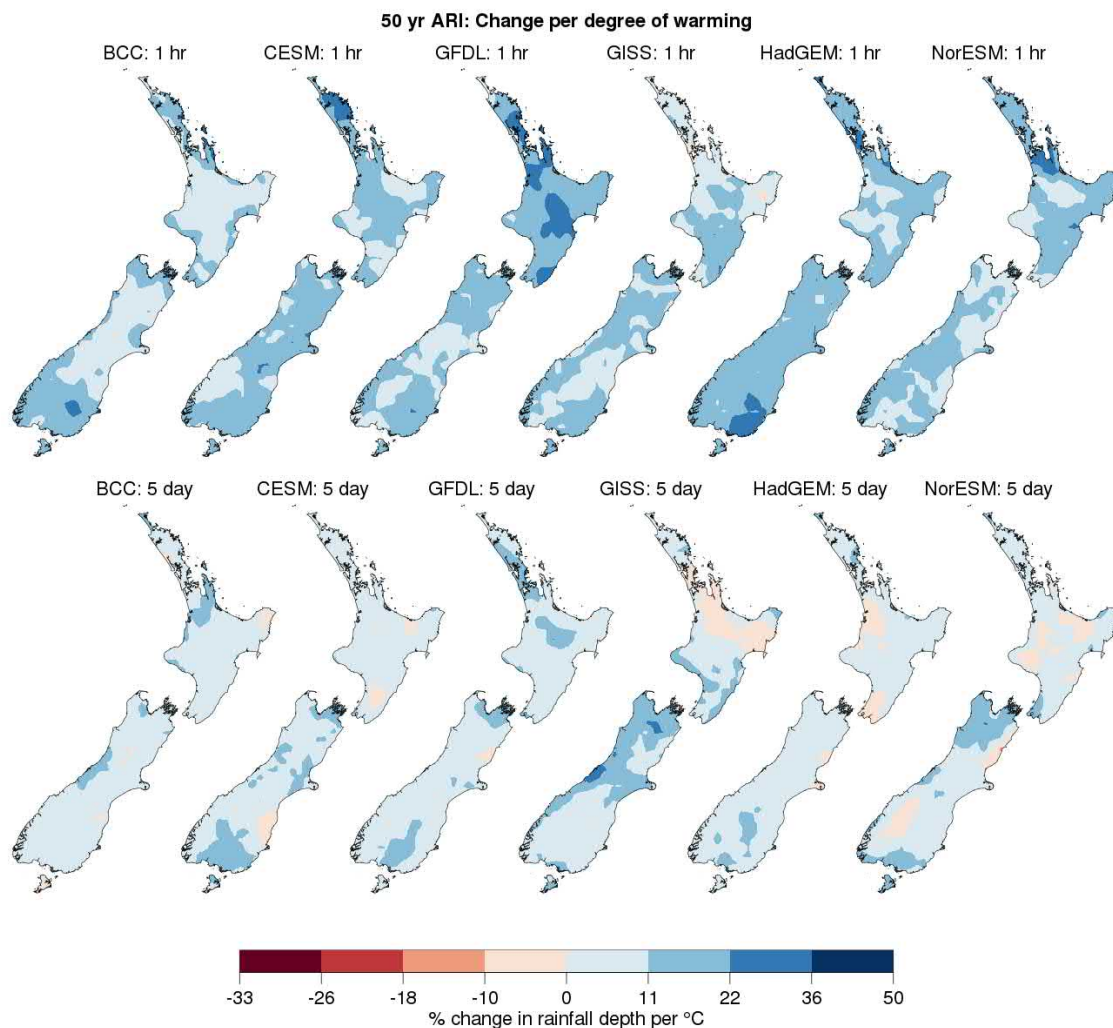


**Figure 22: Percentage changes per degree of warming in the 50-year event magnitude for each GCM driving model. The top row shows the change for the 1-hour duration event and the bottom row for the 5-day event.**

To obtain more robust estimates of the trends in the  $\mu$  and  $\sigma$  parameters of the fitted non-stationary GEV distribution, all available simulations were combined as described in the previous section. These trends are shown for a selection of event durations in Figure 23 and the resulting changes in event magnitude for a 50-year return period are shown in Figure 24. After combining all simulations, the changes in rainfall depth are all positive, regardless of event duration. Despite the large regional variability between the different models shown in Figure 22, some regional structure is apparent in this multi-model result, in particular, for short durations there appears to be larger increases in the north of the North Island and in the south-east of the South Island. Scrutiny of Figure 23 shows that



the increase in the far south is due to increases in the location of the GEV distribution (analogous to the mean); i.e., the entire annual maxima series distribution has increased more strongly in this region. Conversely, increases in the north are due to increases in the scale parameter (analogous to the variance); i.e., the spread is larger, producing larger extremes in this region.

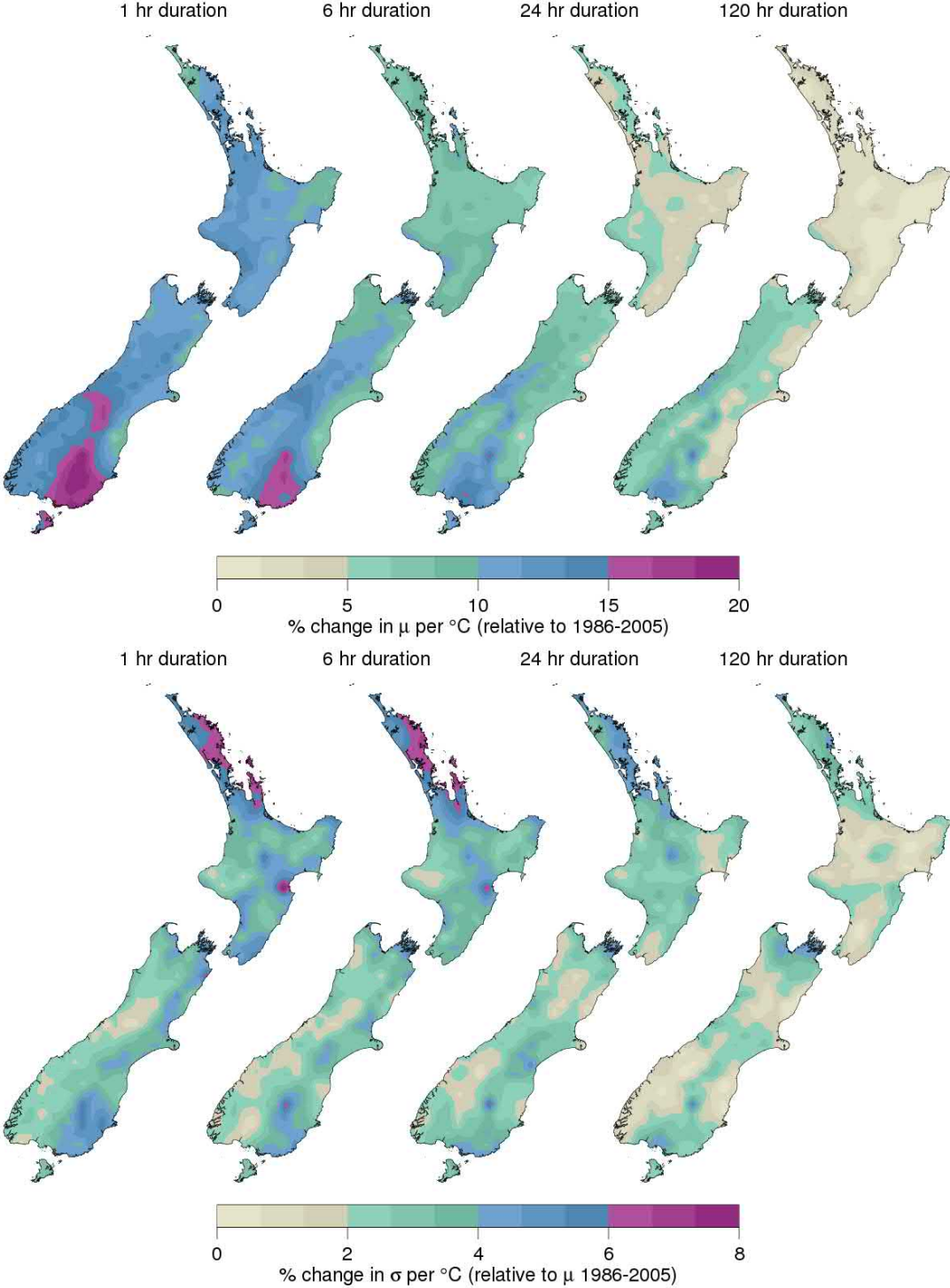


**Figure 23: Trends in  $\mu$  and  $\sigma$  as a function of temperature, for four different event durations, derived from all 24 RCM simulations combined. Each parameter is mapped as a percentage change relative to  $\mu$  over the 1986—2005 period.**

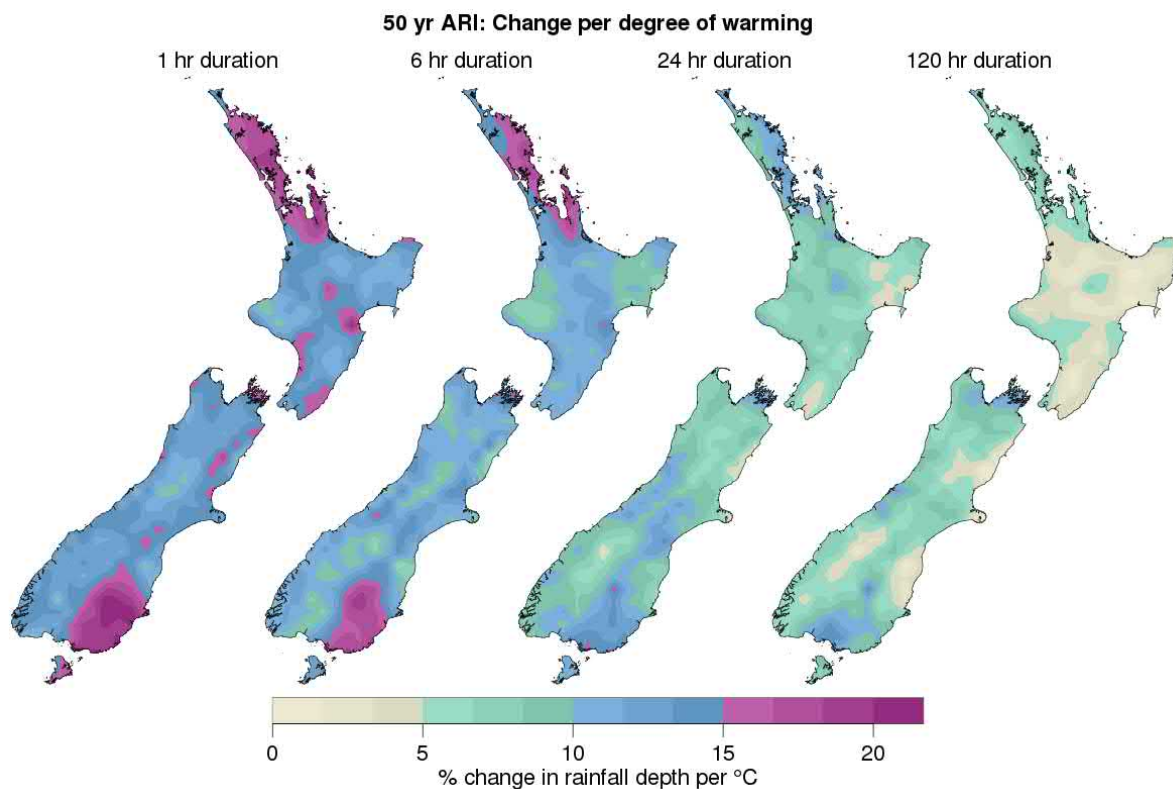


**Figure 24: Percentage changes in the 50-year event magnitude for four different event durations. Each map combines all 24 different RCM simulations and shows the change per degree of warming.**

While these regional patterns appear coherent and may have some physical explanation (for example more intense tropical storms in the future may lead to the most extreme events becoming more intense in Northland and Coromandel), the large regional variability between RCM simulations does not allow us to say with confidence that these patterns are correct. Until further research has confirmed or updated these patterns, it is not appropriate to estimate climate change augmentation factors for the HIRDS surfaces on a regional scale, however users should be aware that in reality some regions of New Zealand may have larger increases than others.

#### 4.4 Augmentation factors for HIRDS

For use in the HIRDS tool, change factors to incorporate the effect of climate change on extreme rainfall have been estimated from RCM results by taking an average over the whole of the New Zealand mainland. That is, for each event duration and return period, a uniform estimate of the percentage change per degree of warming has been made by taking the median over New Zealand of the relevant surface equivalent to those shown in Figure 24. In addition, the 5<sup>th</sup> and 95<sup>th</sup> percentile over the country has been taken to provide some indication of the possible range of values that might be expected.

These average values are shown in Figure 25 and Table 6 for a selection of durations and return periods. There is a large difference in the percentage change per degree of warming between the different event durations, whereas for a given duration the percentage change is relatively similar across the range of return periods shown. For the 24-hour duration the increase ranges from about 7.2 to 8.6%/°C, which is roughly equivalent to the Clausius-Claperyon relation discussed earlier. For

longer durations, the increase is less than this, but for shorter durations the increase exceeds the C-C relation. At the 1-hour duration it ranges from 12.2 to 13.6%/°C, which is slightly less than double the C-C relation.

The shaded bars in Figure 25 give an indication of the range of possible values that could be expected within New Zealand for the 1-hour and 5-day event duration. Table 7 provides this range of expected values for a larger selection of durations. The size of these bars relative to the difference between durations shows that we are still a way off providing precise predictions of how extreme precipitation will change in a warming climate. However, we can be confident that the change will be positive, even for long duration events, and that for hourly durations increases in excess of 10%/°C are very likely.

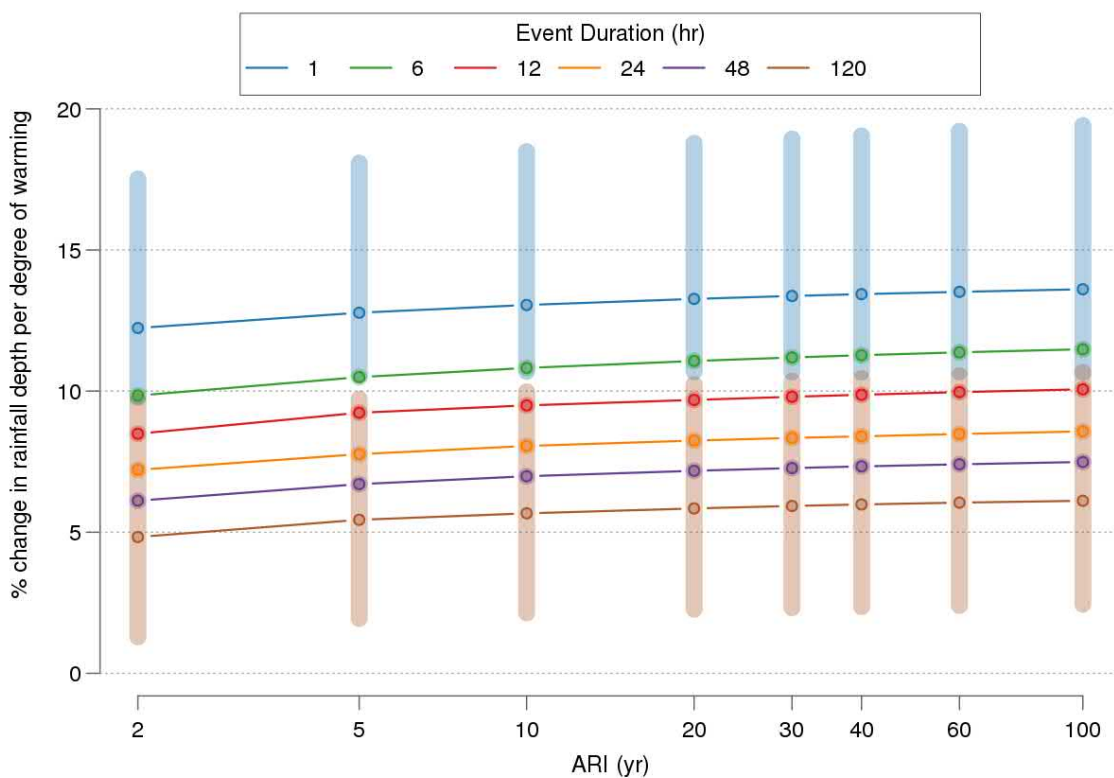


**Figure 25: Augmentation factors for extreme precipitation based on 1 degree of warming plotted as a function of return period. The solid lines show the median over New Zealand for different event durations and the 5<sup>th</sup> and 95<sup>th</sup> percentiles are displayed as shaded bars for the 1- and 120-hour event durations.**

In order to use the augmentation factors in Table 6 to create depth-duration-frequency tables for a particular time period of a given emissions scenario it is necessary to estimate the temperature change relative to the current climate. For this analysis, the New Zealand land average RCM bias-corrected surface air temperature was used to model the change in extreme rainfall (Figure 17). The years 1986—2005 were used to provide the “current climate” temperature and this is assumed to be equivalent to the period used for the main HIRDS analysis.

**Table 6: Percentage change factors to project rainfall depths derived from the current climate to a future climate that is 1 degree warmer.**

DURATION/ARI	2 YR	5 YR	10 YR	20 YR	30 YR	40 YR	50 YR	60 YR	80 YR	100 YR
1 HOUR	12.2	12.8	13.1	13.3	13.4	13.4	13.5	13.5	13.6	13.6
2 HOURS	11.7	12.3	12.6	12.8	12.9	12.9	13.0	13.0	13.1	13.1
6 HOURS	9.8	10.5	10.8	11.1	11.2	11.3	11.3	11.4	11.4	11.5
12 HOURS	8.5	9.2	9.5	9.7	9.8	9.9	9.9	10.0	10.0	10.1
24 HOURS	7.2	7.8	8.1	8.2	8.3	8.4	8.4	8.5	8.5	8.6
48 HOURS	6.1	6.7	7.0	7.2	7.3	7.3	7.4	7.4	7.5	7.5
72 HOURS	5.5	6.2	6.5	6.6	6.7	6.8	6.8	6.9	6.9	6.9
96 HOURS	5.1	5.7	6.0	6.2	6.3	6.3	6.4	6.4	6.4	6.5
120 HOURS	4.8	5.4	5.7	5.8	5.9	6.0	6.0	6.0	6.1	6.1

**Table 7: As in Table 6, but showing the variability that could be expected across New Zealand based on the Regional Climate Modelling results.**

DURATION/ARI	2 YR	5 YR	10 YR	20 YR	30 YR	50 YR	100 YR
1 HOUR	9.8 – 17.5	10.6 – 18.1	10.7 – 18.5	10.7 – 18.8	10.7 – 18.9	10.7 – 19.1	10.7 – 19.4
2 HOURS	9.2 – 18.0	9.9 – 18.4	10.0 – 18.7	10.1 – 19.0	10.1 – 19.1	10.1 – 19.3	10.1 – 19.6
6 HOURS	7.5 – 14.9	8.0 – 15.4	8.3 – 15.9	8.4 – 16.4	8.5 – 16.6	8.5 – 17.0	8.5 – 17.4
12 HOURS	5.7 – 13.5	6.5 – 13.9	6.8 – 14.2	7.1 – 14.5	7.2 – 14.8	7.3 – 15.1	7.3 – 15.4
24 HOURS	4.0 – 11.9	4.6 – 12.0	4.8 – 12.1	4.9 – 12.2	5.0 – 12.3	5.1 – 12.5	5.2 – 12.8
48 HOURS	2.6 – 11.0	3.1 – 11.1	3.3 – 11.2	3.4 – 11.3	3.4 – 11.3	3.4 – 11.4	3.5 – 11.5
72 HOURS	2.1 – 10.5	2.6 – 10.6	2.7 – 10.8	2.8 – 10.9	2.9 – 11.0	2.9 – 11.1	2.9 – 11.2
96 HOURS	1.7 – 10.0	2.2 – 10.2	2.4 – 10.5	2.5 – 10.7	2.6 – 10.9	2.6 – 11.0	2.7 – 11.2
120 HOURS	1.3 – 9.6	1.9 – 9.7	2.1 – 10.0	2.3 – 10.2	2.3 – 10.4	2.4 – 10.5	2.4 – 10.7

The historical observations used for the HIRDS analysis cover the period 1853—2016, which is clearly very different from 1986—2005, however, the vast majority of the observations were from the more recent decades (2/3 from after 1970). The 1986—2005 period is approximately half way between 1970 and 2016, and assuming a roughly linear temperature trend (see NIWA’s seven station series for example<sup>1</sup>), the average temperature during the shorter period should be similar to that of the longer period (1970—2016).

It is important that the temperature data used to estimate future augmentation factors be from the same source as that used to model the changes in extreme precipitation observed in the RCM simulations. For this purpose, Table 8 contains the mean temperature change for each RCP at three future time periods relative to 1986—2005. These projected temperature changes are different to those provided in Tables 5, 6 and 7 of *Mullan et al.* [2016] as those projections were derived from statistical downscaling of global climate models (rather than dynamical downscaling using a regional

<sup>1</sup> <https://www.niwa.co.nz/our-science/climate/information-and-resources/nz-temp-record/seven-station-series-temperature-data>

climate model) and also because the changes in this report are averages over the entire New Zealand, rather than selected locations or the seven station series.

**Table 8: New Zealand land-average temperature increase relative to 1986—2005 for four future emissions scenarios. The three 21<sup>st</sup> century projections result from the average of six RCM model simulations (driven by different global climate models). The early 22<sup>nd</sup> century projections are based only on the subset of models that were available and so should be used with caution.**

	2031—2050	2056—2075	2081—2100	2101—2120
<b>RCP 2.6</b>	0.59	0.67	0.59	0.59 (4 model avg)
<b>RCP 4.5</b>	0.74	1.05	1.21	1.44 (5 model avg)
<b>RCP 6.0</b>	0.68	1.16	1.63	2.31 (CESM1-CAM5 only)
<b>RCP 8.5</b>	0.85	1.65	2.58	3.13 (3 model avg)

## 5 Areal reduction factors

### 5.1 Background

In hydrological design and planning, it is usually necessary to prescribe a catchment design rainfall event consisting of a set of rainfall depths or intensities varying in space (i.e., areal variation) and time reflecting natural conditions within a storm. However, raingauge data are point-based and normally uniform over a small surrounding area. To convert point rainfall depths to areal depths an Areal Reduction Factor (ARF) is employed which is the ratio between areal average rainfall and point rainfall for a given area, duration and return period. The ARF may vary depending on catchment climate and characteristics as well as the record period and methods used in its derivation [Svensson and Jones, 2010].

At present areal rainfall is difficult to measure, so both indirect theoretical and empirical approaches have been developed [Pietersen et al., 2015; Srikanthan, 1995; Svensson and Jones, 2010].

Theoretical methods assume that rainfall processes are stationary and isotropic and have large data requirements. They are best suited for application to short duration rainfalls over small areas [Svensson and Jones, 2010]. In this nationwide exploratory study, where appropriate rainfall data are sparse, we employ an empirical approach. Two empirical methods are used internationally – storm-centred and geographically centred (fixed area). Broadly speaking, fixed area methods estimate ARF values by averaging rainfall data over an area whereas storm-centred ARF values are the result of calculating ARF values for each of a large sample of storms and averaging them [Olivera et al., 2008]. The storm-centred approach has not seen widespread application mainly due to lack of information about storms with large return periods, problems with including multi-centred storms and limitation to specific types of storm events [Asquith and Famiglietti, 2000]. This approach is generally used in calculating catchment probable maximum precipitation [Srikanthan, 1995].

In New Zealand, Tomlinson [1978] examined seven storms with extreme rainfalls, but was unable to calculate ARF values owing to very large variations in rainfall depth-area characteristics.

Subsequently, Tomlinson [1980] recommended the use, with caution, of ARF values published by the Natural Environment Research Council [NERC, 1975] which were derived by a fixed-area method.

These values are commonly employed in New Zealand without verification in the absence of alternatives.

Given these findings we adopt a fixed-area approach and apply three standard methods for estimating ARF values. Due mainly to limitations regarding record length and raingauge density, investigations are confined to areas in Auckland, Tasman and Christchurch. Other areas in Northland, Hawkes Bay, and Southland were examined, but consistent results could not be obtained at these locations. The methods and results shown in this section are based on work described in Singh et al. [2018].

### 5.2 Theory

Three standard methods are employed internationally to derive ARF values empirically using recorded rainfall depths at a number of raingauges [Srikanthan, 1995]. Two specify ARF as a function of area ( $A$ ) and rainfall duration ( $D$ ): the other includes return period  $T$  as well. A brief description of the methods and their behaviour follows [Pietersen et al., 2015; Srikanthan, 1995].

### 5.2.1 US Weather Bureau method (USWB)

Using data from raingauge networks covering areas from 200 to 1000 km<sup>2</sup>, the *United States Weather Bureau* [1957] employed the expression

$$ARF = \frac{\sum_{j=1}^n \sum_{i=1}^N w_i P_{dij}}{\sum_{j=1}^n \sum_{i=1}^N w_i P_{ij}} \quad (4)$$

in which  $N$  is the number of raingauges,  $w$  is a Thiessen weighting factor [Smith, 1993] for gauge  $i$ ,  $P_{dij}$  is the point rainfall for gauge  $i$  on the day the annual maximum areal rainfall occurs in year  $j$ ,  $P_{ij}$  is the annual maximum point rainfall for the chosen duration for year  $j$  at gauge  $i$ . The areal reduction factor for each event of specified duration is calculated using Thiessen weights and the largest of these in each year of record is selected. The sum of the resulting annual series multiplied by the number of gauges constitutes the numerator in Equation (4). The denominator in Equation (4) is the sum of the largest point rainfalls at each gauge in each year over all gauges and all years. On average the number of raingauges employed was six and the data period ranged from 7 to 15 years.

### 5.2.2 UK Flood Studies Report method (UKFSR)

In the UKFSR method, areal rainfall for each raingauge is computed to identify the time the maximum occurs and the  $P_{dij}$  values are abstracted [NERC, 1975]. Also, the maximum point values,  $P_{ij}$ , are identified. The mean of the ratio of  $P_{dij}/P_{ij}$  over all gauges and all years of record is determined and  $ARF$  is defined as

$$ARF = \frac{1}{n} \sum_{j=1}^n \sum_{i=1}^N w_i \frac{P_{dij}}{P_{ij}}$$

Generally, for a given area the ARF values produced by this method are smaller (i.e. they produce a larger reduction) than those given by the USWB method, but this difference decreases with increasing duration and area.

### 5.2.3 Bell's method

For the method of Bell [1976], the annual maximum areal rainfall and the annual maximum point rainfall series at each raingauge are ranked. Then the Thiessen weighted mean of point rainfalls of the same rank is computed to give an annual series of weighted maximum point rainfalls. The ARF of rank  $m$  is defined as the ratio of the areal rainfall of rank  $m$  to the weighted average point rainfall of rank  $m$ , that is

$$ARF_m = \frac{S_m}{R_m} = \frac{\sum_{i=1}^N w_i P_{dim}}{\sum_{i=1}^N w_i P_{im}} \quad (5)$$

where  $S_m$  is the  $m^{\text{th}}$  ranked annual maximum areal rainfall and  $R_m$  is the  $m^{\text{th}}$  ranked areal average of annual maximum *point* rainfall. If ARF values are assumed to be independent of rank, or return period, then the mean of  $ARF_m$  over all ranks gives an estimate dependent only on  $A$  and  $D$ .

Bell's method can be used to estimate the relationship between ARF and return period,  $T$ . To do this, an extreme value distribution is fitted separately to both the numerator and denominator of Equation (5). The ARF at a given return period is then simply the ratio of the two extreme value curves evaluated at that return period. Care must be taken to ensure that the fitted extreme value distributions are robust, especially when the record length is short. For this analysis, the Gumbel

distribution has been used as it is less prone to over-fitting than the GEV, which has been used in other parts of this report.

## 5.3 Analysis

### 5.3.1 Data and pre-processing

Using the station rainfall data gathered for the HIRDS analysis, locations in New Zealand were sought where there was a sufficient density of raingauges having enough simultaneous or common record length to be able to apply the three methods of ARF estimation. These requirements regarding density and record are quite stringent and were satisfied only by locations in Auckland (45 gauges with record lengths of 11 years), Christchurch (19 gauges with 12-year record lengths) and Tasman (15 gauges with 11-year record lengths) (Table 9).

**Table 9: Gauges used for ARF analysis in each of the three regions.**

Site Number	Site Name	Latitude	Longitude
<b>Auckland (2002—2012)</b>			
646619	Orewa at Orewa Treatmt Plant Pond	-36.596434	174.678149
647510	Ararimu at Zanders	-36.704659	174.555419
647513	Kumeu at Maddrens	-36.773967	174.561478
647614	Rangitopuni at Walkers ( Farm )	-36.738856	174.618907
647618	Albany at Albany Heights Rd	-36.710511	174.691272
647619	Paremoremo at School	-36.754625	174.6484
647727	Oteha at Rosedale Pond Treatment Plant	-36.731362	174.694872
647737	Mairangi Bay at School	-36.744046	174.7467
647738	Birkdale at Inwards Reserve	-36.797871	174.706593
647739	Torbay at Glamorgan School	-36.700983	174.73442
648510	Swanson at O'Neills Rd	-36.87369	174.582822
648513	AC Waitakere Filter Stn	-36.892107	174.556324
648515	WCC W/S Reservoir, Red Hills Rd	-36.838533	174.58314
648516	Waitakere Domain, Bethell Rd	-36.850893	174.539685
648517	Candia Rd at Henderson Valley	-36.893342	174.594503
648612	Henderson W.E.P.B. Depot	-36.884809	174.622353
648613	Transpower Sub Stn	-36.840714	174.617947
648614	WCC Sewer Pump Stn	-36.894149	174.659604
648615	Avondale Racecourse	-36.894539	174.692155
648625	WCC Pump Sn at Constable Lane	-36.819614	174.642112
648626	Te Pai Park Henderson	-36.861213	174.633011
648627	Sunnyvale, Blue Ridge Close	-36.892694	174.637125
648717	Meola Ck at Mt Albert Grammar	-36.885911	174.724481
648718	Alexandra Park Raceway	-36.892219	174.779623
648719	Albert Park ACC	-36.850061	174.767324



648732	Bayswater at Plymouth Reserve	-36.813746	174.783211
648733	Cox's Bay Park	-36.85153	174.732595
648816	Churchill Park	-36.853623	174.876208
648817	Okahu Bay Bowling Club	-36.855487	174.820177
649514	Arataki Visitor Centre	-36.946515	174.594618
649516	WCC Res Bush Rd, Waiatarua	-36.93492	174.586489
649517	247 Forrest Hill Rd, Waiatarua	-36.915066	174.588274
649518	71 Opanuku Rd, Henderson Valley	-36.912678	174.566891
649625	Waituna Stm at Huia Filter Station	-36.938591	174.641589
649636	Oratia Cemetery, Oratia	-36.910971	174.620727
649637	Cutler Park, New Lynn	-36.92261	174.683864
649638	9 Cochran Rd Oratia	-36.937205	174.61461
649713	Mt Roskill Sub Stn Whau	-36.912939	174.725157
649714	Onehunga Harbour Rd Reserve	-36.930903	174.783986
649723	Onehunga at Rowe St	-36.924523	174.788301
649818	Anns Ck at ACC Abattoir	-36.936379	174.83353
649820	Pakuranga at Pakuranga Village	-36.901037	174.896567
649836	Bassant Reserve	-36.908868	174.80811
649937	Mangamangaroa at Craigs	-36.936457	174.93234
659401	Matiatia Bay, Waiheke Island	-36.779297	174.999701
<b>Christchurch (2004—2015)</b>			
323605	42A Peraki St, Kaiapoi (XKA)	-43.384903	172.651829
324501	ChCh Airport	-43.493000	172.537000
324606	Harbour Rd, Brooklands	-43.399418	172.691247
324607	Lower Styx Rd	-43.443502	172.683612
324608	PS 62, Tyrone St	-43.443371	172.637901
324610	Firestone Factory, Papanui	-43.490961	172.604243
325403	PS 80 site, Templeton	-43.544940	172.464075
325507	College of Education	-43.522960	172.566812
325508	Wigram Retention Pond	-43.553878	172.579083
325510	Halswell Retention Basin	-43.561003	172.526998
325615	Kyle St EWS	-43.530740	172.607690
325616	ChCh Gardens	-43.529403	172.620063
325617	Horseshoe Lake, PS205	-43.503167	172.682807
325618	PS 42, Sparks Rd	-43.566721	172.602812
325619	Tunnel Rd	-43.555134	172.691695
325621	Bowenvale Flume	-43.580714	172.647646
325711	Van Asch St, Sumner	-43.580006	172.757133
325712	Reservoir #4, Clifton	-43.577674	172.740416
326616	Upper Bowenvale Valley	-43.599785	172.650323

**Tasman (2007—2017)**

132337	Wakapuaka at Hira	-41.213	173.3979
133236	Richmond at Race Course	-41.3284	173.1843
133237	Richmond at TDC Office	-41.3418	173.1865
133336	Brook at Third House	-41.3253	173.3247
133337	Nelson at Princes Dr	-41.2831	173.2562
134001	Wairoa at Little Ben	-41.4662	173.0959
134036	Wai-iti at Birds	-41.423	173.07
134236	Lee at Trig F	-41.4792	173.1883
157517	Wai-iti at Belgrove	-41.4554	172.958
157521	Wairoa at Irvines	-41.4033	173.1308
157523	Waimea at TDC Nursery	-41.3137	173.1262
157524	Roding at Skid Site	-41.3567	173.2618
157531	Kainui Dam	-41.5109	172.9542
157608	Orphanage at Ngawhatu	-41.3239	173.2317
157808	Maitai at Forks	-41.2931	173.37

Time series of annual maxima for the various durations exhibited no evidence of trend, periodicity, persistence or shifts according to the Mann-Whitney and Wald-Wolfowitz statistical tests and visual inspection [see also *G A Griffiths et al., 2014; Withers and Pearson, 1991*]. This means that records can be assumed to be stationary and composed of independent values.

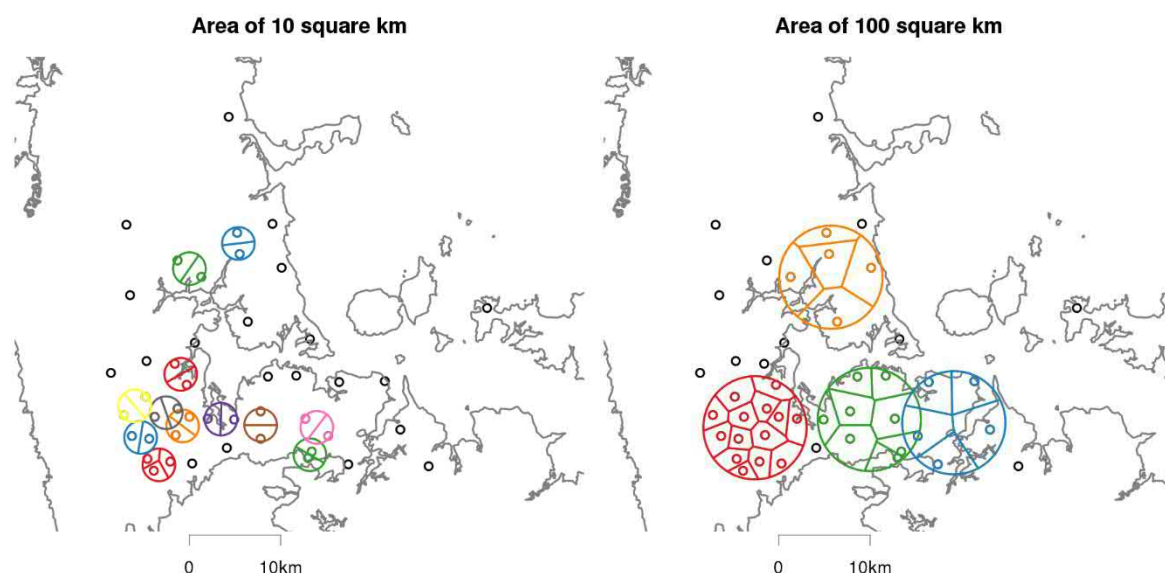


**Figure 26: Examples of Thiessen polygons for 10 and 100 km<sup>2</sup> areas in the Auckland region. Black circles represent stations used in the study. Colours pertain to the different Thiessen groups for the given area. For the 10 km<sup>2</sup> area, there are 12 different Thiessen groups, each containing 2 gauges. For the 100 km<sup>2</sup> area, there are four groups containing between 5 and 14 gauge each.**

The areal rainfall for a given area and duration was determined using the Thiessen polygon method [Smith, 1993]. This method divides a circular area into different polygons each containing a single gauge, where the edges of the polygons are halfway between the nearest gauges. The weights assigned to each gauge are determined by the relative size of its containing polygon.

For each region and area, the different combinations of gauges making up a Thiessen area were searched to find the maximum number of mutually exclusive sets of gauges. ARF values were found using the above methods for each group of stations. The final ARF for each region and area was then calculated as the average of the different groups, weighted by the number of gauges in each group. This technique means that the smaller areas, which contain fewer gauges and would therefore be less robust, have many groups of stations which increases confidence in the result. For the largest areas, there is generally only one group, but as it contains many gauges typically provides a robust result. Examples of this are shown in Figure 26.

### 5.3.2 Comparison of ARF methods

The USWB, UKFSR and Bell's methods were applied to calculate ARF values for the three regions. In applying the three methods, circular areas of 10, 20, 50, 100, 200 and 500 km<sup>2</sup> were specified along with durations ranging from 1 hour to 5 days. As Figure 27 and Figure 28 show, areal reduction factors derived using the different methodologies are very similar. Bell's method generally has the largest ARF values while the UKFSR method has the lowest, however the difference between the three methods less than 2 or 3%.

Agreement among the three calculation methods improves a for longer durations. This outcome agrees with previous work by *G A Griffiths and Pearson* [1993] and *G A Griffiths et al.* [2009] using storm and flood data for the Avon River catchment in Christchurch which yielded ARF values similar to those predicted by NERC [1975] as presented in *Faulkner* [1999]. Due to the similarity between the three methods, we have chosen here to use Bell's method as it also has the potential to estimate ARF values for different storm return periods.

The difference between the regions is also small, with Auckland and Tasman showing very similar results, both having slightly higher ARF values than Christchurch.

### 5.3.3 ARF empirical model

Areal reduction factors can be approximately modelled as a function of area (A) and duration (D) using the power law

$$ARF = 1 - cA^aD^{-d} \quad (6)$$

where the exponents *a* and *d* are positive. This function has been fitted to the regional ARF data using a non-linear minimisation technique and, as can be observed in Figure 29, on a logarithmic scale the empirical fit is quite good for durations less than or equal to 24 hours. However, for Auckland, and to a lesser extent Tasman and Christchurch, the power law relationship breaks down for durations greater than 24 hours. This poorer fit is not critical however, as the difference between the calculated and fitted ARF values for longer durations is on the order of 1 or 2%. Due to this mismatch, the parameters for Equation (6) have been estimated using only durations of 24 hours or less and are given in Table 10.

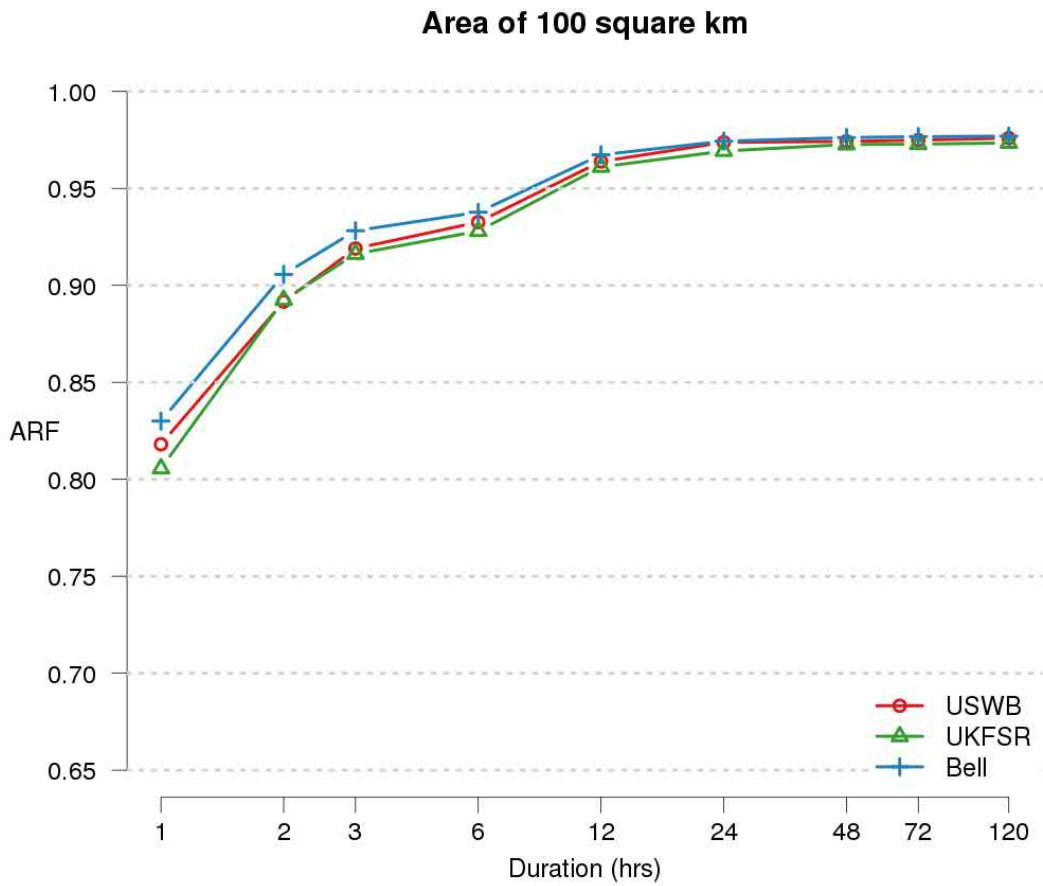


Figure 27: Areal reduction factors for a 100 km<sup>2</sup> area derived from Auckland gauges. Different colours denote the different methodologies used.

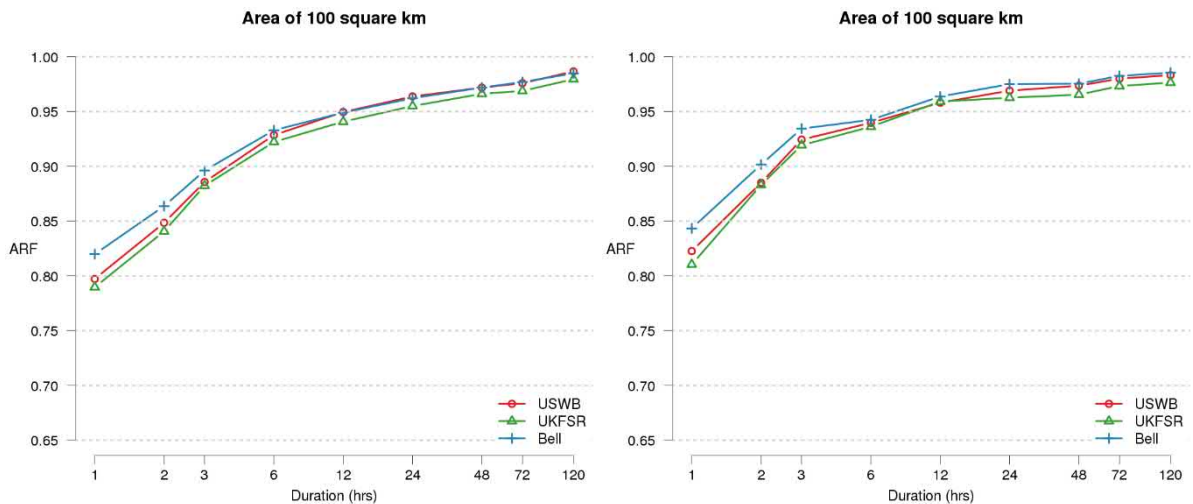
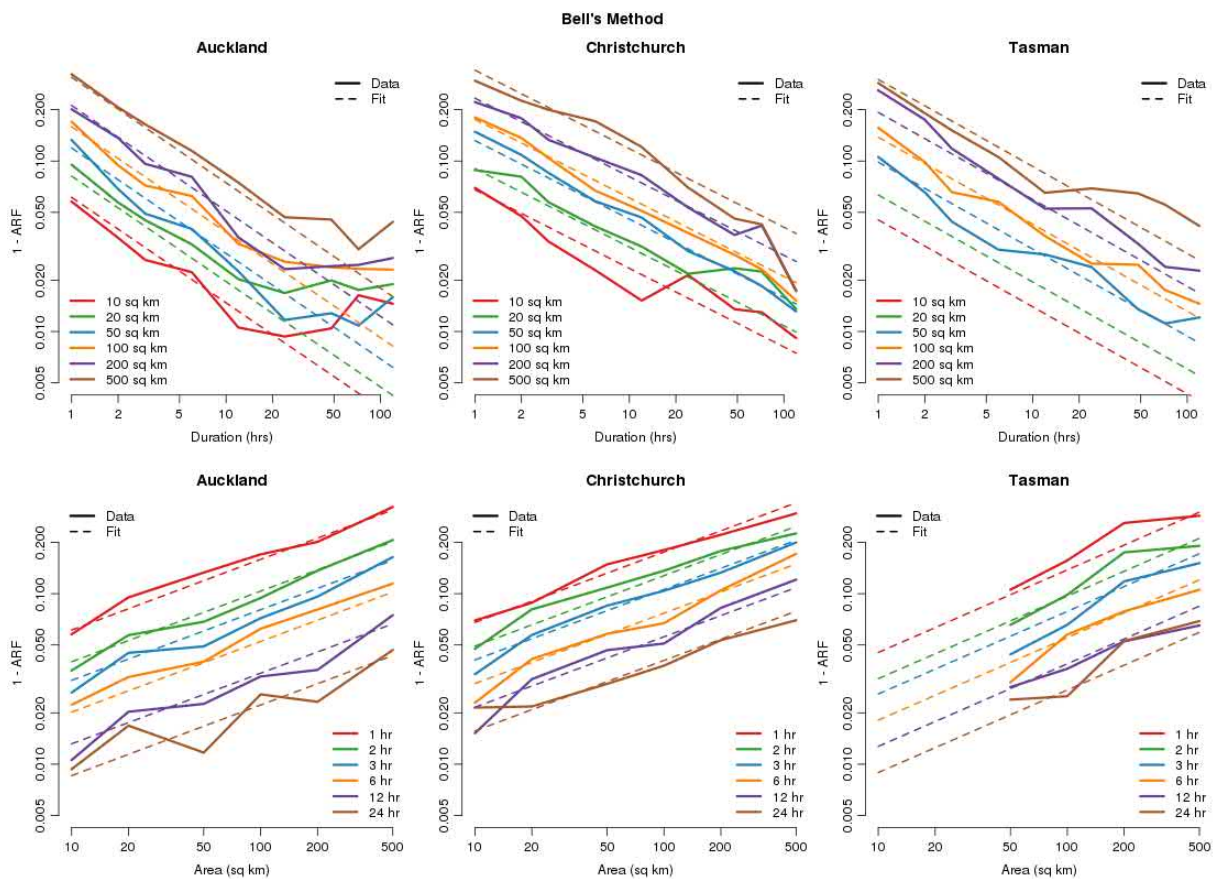


Figure 28: As Figure 27 but for the Christchurch and Tasman regions.



**Figure 29: Empirical power law function fitted to areal reduction factors for Auckland (left), Christchurch (centre) and Tasman (right). All panels show 1-ARF on a logarithmic scale on the y-axis with calculated ARF values as solid lines and the empirical fits as dashed lines. The top row shows each different area (as colours) plotted as a function of duration. The bottom row shows the different durations (as colours) plotted as a function of area. For both duration and area, the x-axis is also on a logarithmic scale.**

**Table 10: Parameters for empirical power law function in Equation (6) fitted to regional areal reduction factors.**

Parameter	Auckland	Christchurch	Tasman	All regions
c	0.024	0.026	0.015	0.024
d	0.62	0.46	0.51	0.53
a	0.41	0.41	0.48	0.41

The areal reduction factors and fitted empirical curves are shown on a linear scale in Figure 30. This figure again shows the similarity between Auckland and Tasman, with Christchurch generally having lower values. Also shown as a black dashed line in this figure is the empirical fit of Equation (6) to all three regions at once. As can be seen, this global fit is never more than approximately 5% away from any of the regional fitted curves so appears to be an appropriate approximation.

For reference, Figure 30 also includes areal reduction factors as published by *Tomlinson* [1980]. These are generally lower than the values derived in this study, although in most cases the differences are not large.

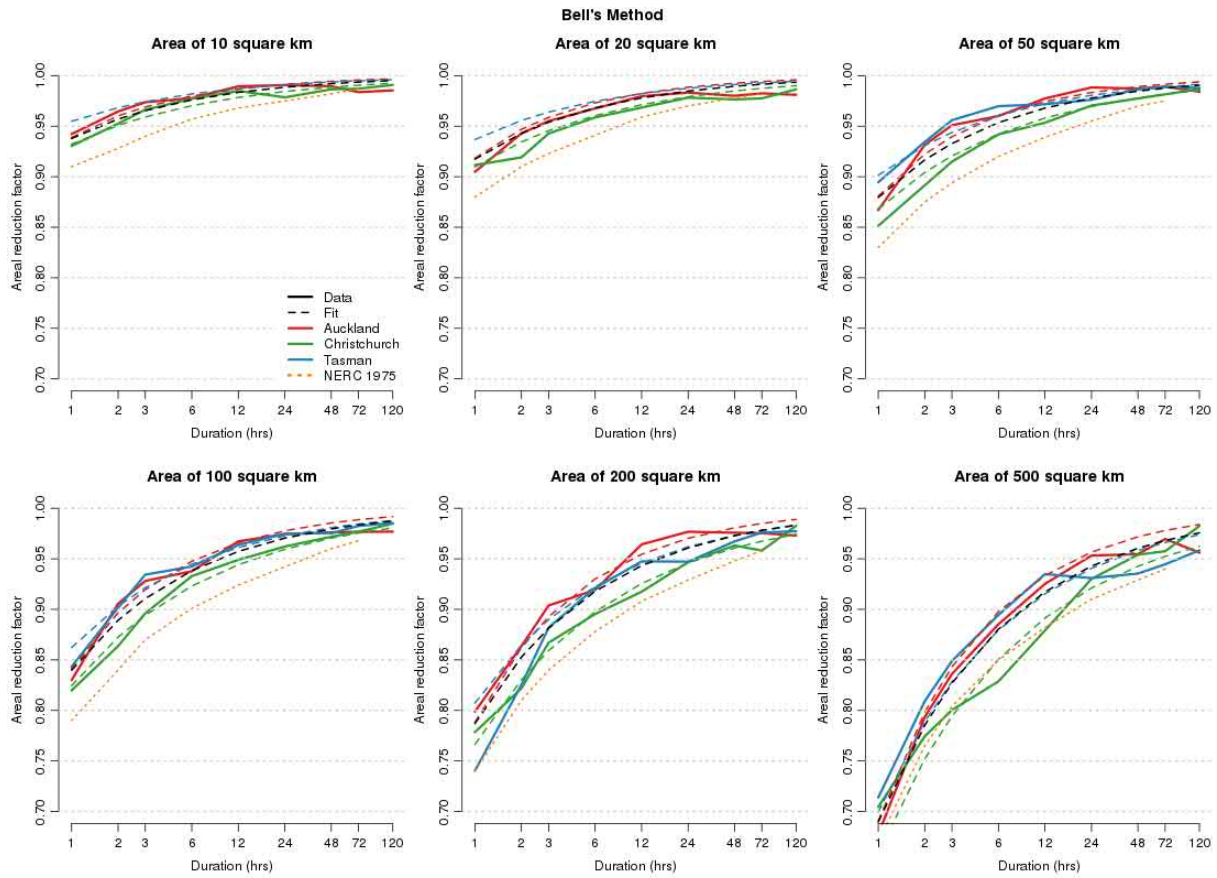


**Figure 30: The same data as Figure 29, but separated by area and showing ARF on a non-logarithmic y-axis. The different regions are shown as different colours and areal reduction factors as published by Tomlinson [1980] are shown by the dotted orange line. The dashed black line shows the empirical model as fitted to all three regions at once.**

### 5.3.4 Return period dependence

As described in Section 5.2.3, Bell's method can also be used to investigate how areal reduction factors change depending on the rarity of an event. To do this an extreme value distribution is fitted separately to each of the two components that make up the areal reduction ratio ( $S_m$  and  $R_m$ ) from Equation (5). In this report, each Gumbel distribution was fitted after taking the average over the (normalised)  $S_m$  and  $R_m$  from the Thiessen groups within each area (refer Figure 26). If there are  $K$  groups, these normalised averages are found using

$$S_m = \frac{1}{K} \sum_{k=1}^K \frac{S_m^k}{S^k} \quad \text{and} \quad R_m = \frac{1}{K} \sum_{k=1}^K \frac{R_m^k}{S^k}$$

where  $S_m^k$  is the  $m^{\text{th}}$  ranked annual maximum areal rainfall for the  $k^{\text{th}}$  group and  $S^k$  is the average of all  $m$  annual maxima areal rainfall for group  $k$ .  $S^k$  is used to normalise both the area-based maxima ( $S_m^k$ ) and the point-based maxima ( $R_m^k$ ). Once the Gumbel distribution has been fitted to both  $S_m$  and  $R_m$ , the areal reduction factor for a given return period is the ratio of the two extreme value curves evaluated at that return period. This fitting process is repeated for each duration and area.

Due to the limited length of the data sets used, sometimes the best fit distribution for a region did not seem plausible, especially for long durations and small areas. For this reason, the results included in the report (see Figure 31) are derived from all three regions combined.

Even after combining across regions, when both area is less than 50 km<sup>2</sup> and duration greater than 24 hours the results are not reliable, with some of the reduction factors exceeding 1. However, for the larger areas and shorter durations, the reduction factors follow a consistent decreasing pattern with increasing return period. For the 1-hour event duration, the decrease in ARF from a 2-year to 100-year return period can be up to 10%, whereas for the 12-hour duration the decrease is around 2%.

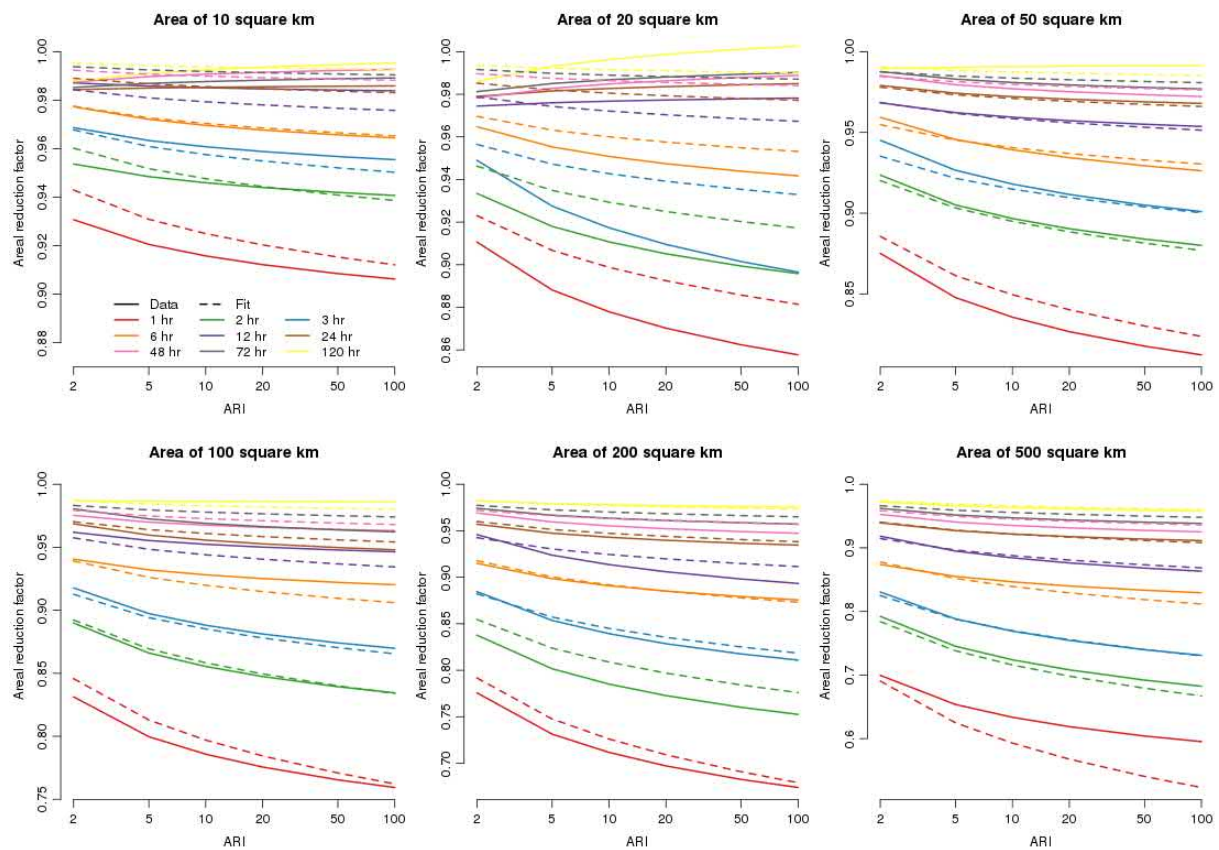


**Figure 31: Areal reduction factors as a function of return period for a range of durations and areas. The curves derived from the three regional datasets are shown as solid lines and an empirical fit to these results is depicted by the dashed lines. Note the different y-axis scales.**

This relationship can be approximated by adding an additional term to Equation (6) so that it becomes

$$ARF = 1 - cA^aD^{-d}(\ln T)^b \quad (7)$$

where  $T$  is the return period in years and the additional exponent  $b$  is positive. This empirical model, shown by the dashed lines in Figure 31, was fitted to the results described above, but only for durations of a day or less and areas greater than 20km. The parameters for this model were found to be  $c = 0.023$ ,  $d = 0.52$ ,  $a = 0.43$  and  $b = 0.23$ .

### 5.3.5 Usage

Areal reduction factors should be used to derive area average rainfall depth from point-based estimates of rainfall depth for an event of a given frequency and duration. The most common use is to estimate the total rainfall amount that will contribute to flow at the base of a catchment. Areal reduction factors are most accurate when an event's rainfall depth is not too dissimilar across the catchment as it is assumed that the rarest parts of the event could occur equally likely anywhere in the catchment. When part of the catchment has much larger rainfall depths than the remainder, the rare events in that area will typically align closely with the rare catchment events. This means that areal reduction factors should be used with caution in areas of complex terrain.

As an example of applying areal reduction factors, suppose the average rainfall depth for a 48-hour, 1-in-20 year event is required for a given catchment that has an area of 200 km<sup>2</sup>. Firstly, an estimate of the catchment average *point-based* rainfall depth is required. This can be found by taking the catchment average of multiple HIRDS 48-hour, 1-in-20 year rainfall depths as derived in Section 3 of this report. This point-based catchment average will be larger than the actual catchment event depth as it is unlikely that an event of a given rarity will occur throughout the catchment at the same time. The actual catchment average rainfall depth is found by multiplying the point-based average by the appropriate areal reduction factor.

Area average rainfall depth can also be derived in a similar manner based on estimates of point-based rainfall depth from gauge measurements instead of HIRDS. However, care must be taken as the one or more gauges used must be representative of the entire catchment.

## 5.4 Summary

Areal reduction factors have been estimated for three regions in New Zealand and the three methods tested produced relatively similar results. This study has used, and recommends usage of, the method described by *Bell* [1976] as it produces consistent results also allows for dependence on return period.

Areal reduction factors for Auckland and Tasman were found to be very similar, while those for Christchurch were slightly lower. The similarity between Auckland and Tasman may be because extremes in both locations will be dominated by convective processes, even though the initiation mechanisms may be different, with topography being a more important driver in the Tasman region. That the reduction factors are lower in Christchurch (i.e.; larger reductions) may seem counter-intuitive. However, as the largest differences are for large areas and durations of around 6 hours, this may be because in Christchurch extreme events of this type are caused by passing systems affecting only part of the region at a time, whereas for Auckland/Tasman the convective initiation mechanisms are geographically stationary and may cause similar impact throughout the event area.

Due to consistency between the regions, it is recommended that the empirical model fitted to all three regions be used to derive areal reduction factors for most regions New Zealand, excluding mountainous areas. Figure 32 can be used to find the NZ-wide areal reduction factor for a given duration and area. However, where appropriate, the reductions factors found for the individual regions should be used instead. The Auckland and Tasman values should be used in those regions, respectively, and the Christchurch values should be used on the plains of Canterbury and Otago. For these regions, Equation (6) along with the appropriate parameters from Table 10 can be used to derive the areal reduction factors.



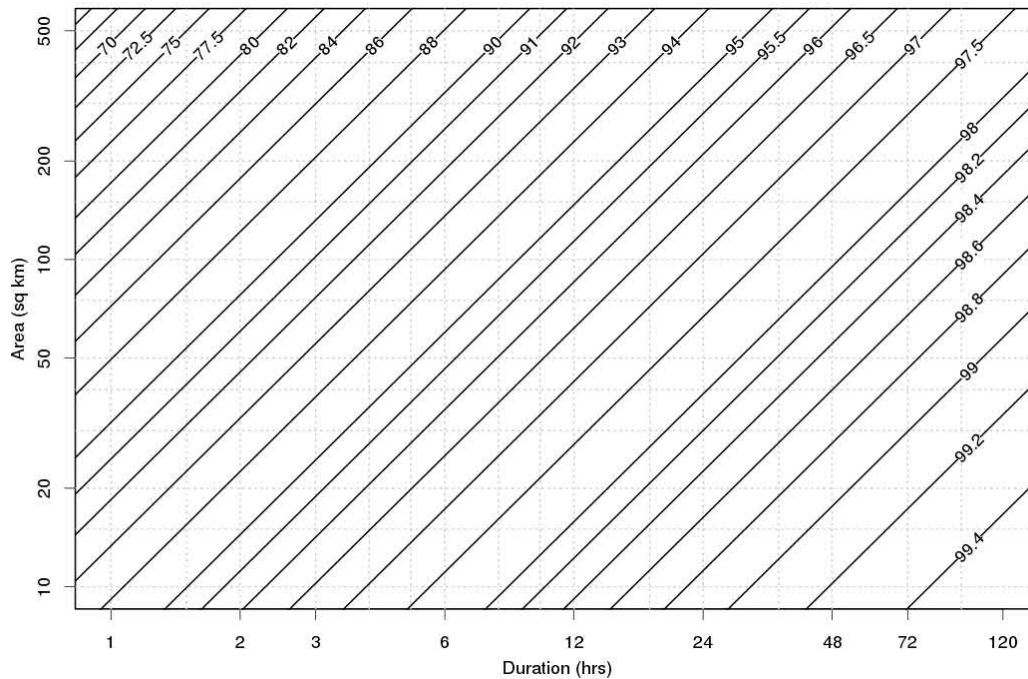


**Figure 32: Area reduction factors (in %) derived from the empirical model of Equation (6) fitted to all three regions.**

For event durations of 24 hours or less and areas greater than 20 km<sup>2</sup>, using reduction factors that don't take return period into account will result in a more conservative reduction than is necessary. That is, using Equation (6) or Figure 32 will result in smaller reductions than those derived from Equation (7), but the latter will be more accurate. When both the above criteria relating to duration and area are met, it is recommended that Equation (7) and associated parameters be used to derive areal reduction factors; i.e.

$$ARF = 1 - 0.023A^{0.43}D^{-0.52}(\ln T)^{0.23}$$

where  $A$  is the area in km<sup>2</sup>,  $D$  is the duration in hours and  $T$  is the return period in years.

## 6 Temporal design storm

### 6.1 Background

In contemporary flood estimation where interest lies with predicting not only the peak but also the volume of a catchment outflow hydrograph, it is necessary to prescribe a hyetograph of storm rainfall of given duration and return period. The variation of rainfall with time (or hyetograph) is characterised by a maximum rainfall depth and a temporal pattern or shape. It has long been known that cumulative hyetographs of rainfall in convective or frontal type storms tend to have their peak rainfall rates early in a storm while cyclonic events tend to have their peak rates near the middle of the storm duration [Eagleson, 1970]. Moreover, results from rainfall-runoff modelling show that hyetograph shape has a strong influence on the shape of a catchment outflow hydrograph [de Lima and Singh, 2002; Marani et al., 1997].

Several methods have been employed to generate temporal patterns of storm rainfall. These include stochastic or statistical approaches [Carroll and Rahman, 2004; Grimaldi and Serinaldi, 2006], sampling patterns from a raingauge record [Laurenson et al., 2010] and analysis of bursts in actual patterns [Bhuiyan et al., 2010; Pilgrim and Cordery, 1975; Rahman et al., 2006]. In New Zealand, Tomlinson [1978] found from a small sample of storms that, regarding peak rainfall and duration, temporal patterns varied most between storms as opposed to within storms; and that variations were relatively insignificant. G A Griffiths and Pearson [1993] employed dimensionless parabolic cumulative curves for hyetographs in a study of high intensity rainfalls in Christchurch. For design flood estimation Jowett and Thompson [1977] and G A Griffiths et al. [1989] used patterns from actual hyetographs. However there appears to have been no regional or national study of temporal storm rainfall patterns. Owing mainly to paucity of data we undertake a reconnaissance or pilot study of storm hyetographs using a conventional analysis of suitably long records from clusters of raingauges where available in New Zealand.

The purpose of the work is to provide guidance as to likely temporal patterns of varying durations for design hyetographs in a number of regions in New Zealand.

### 6.2 Theory

Temporal patterns of storm rainfalls are derived by applying the commonly and easily used average variability method of Pilgrim and Cordery [1975]. For a given raingauge and duration the largest storms by total rainfall depth are listed and the percentages of rain falling in a number of equal intervals of the duration are determined and ranked according to decreasing size. Then the average percentage of rain is found along with the average rank for each interval. The most intense period of rain is assigned to the interval with the lowest average rank and the second to the next lowest and so on. The method is not able to preserve the temporal correlation structure of storm rainfalls and may contain higher temporal correlations than in real storms, leading perhaps to overestimation of rainfall depths within a hyetograph [Australian Rainfall and Runoff, 2015].

To represent a pattern as a cumulative hyetograph we employ a non-dimensional asymmetric hyperbolic tangent function [French and Jones, 2012] of the form

$$\begin{aligned}
 P &= m \tanh[(D - n)W_L] + m & 0 \leq D \leq n \\
 P &= (1 - m) \tanh[(D - n)W_R] + m & n \leq D \leq 1
 \end{aligned}
 \tag{8}$$

in which  $P$  is the proportion of total rainfall depth of a hyetograph,  $D$  is the proportion of the duration,  $W_L$  and  $W_R$  are warp or shape factors left and right of the point of contraflexure or peak rainfall depth and  $m$  and  $n$  are the ordinate of (proportion of rain fallen at) and abscissa of (proportion of time past at) the peak rainfall depth. The tanh function is flexible as to internal subdivision and is more suitable for use in rainfall-runoff models than a gamma-like function as used by *García-Bartual and Andrés-Doménech* [2017] for example.

### 6.3 Analysis

Using the station rainfall data gathered for the HIRDS analysis, locations in New Zealand were sought where there was a sufficient density of raingauges (at least 10) all measuring at 15-minute intervals or less and having a long common record length (30 years) for analysis. These requirements regarding density and record are quite stringent and limit the this study to cover broad climate regions rather than smaller council regions. Around 70 gauges covering New Zealand were split into 6 climate regions as shown in Figure 33.

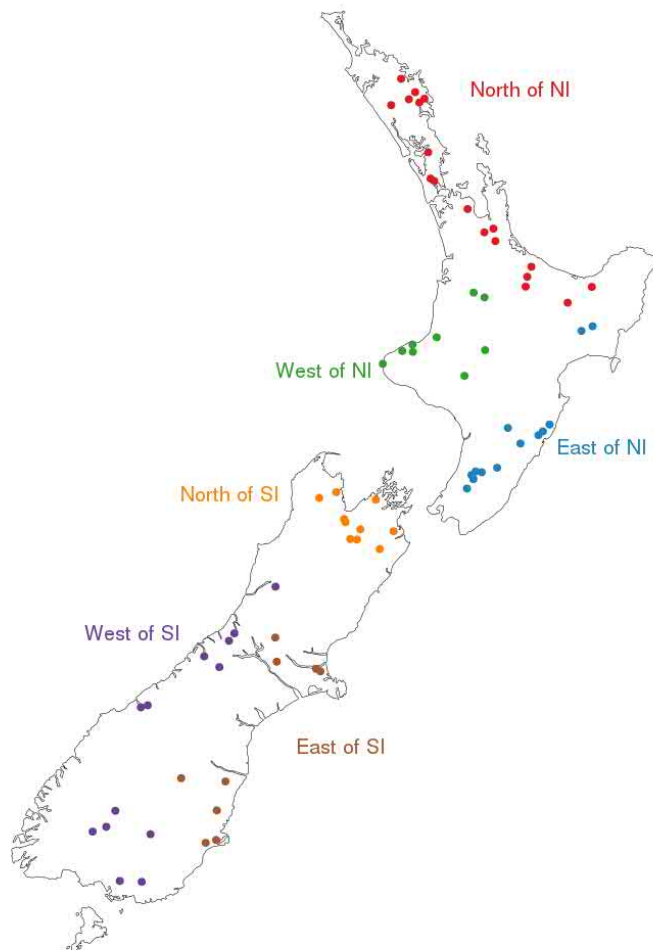
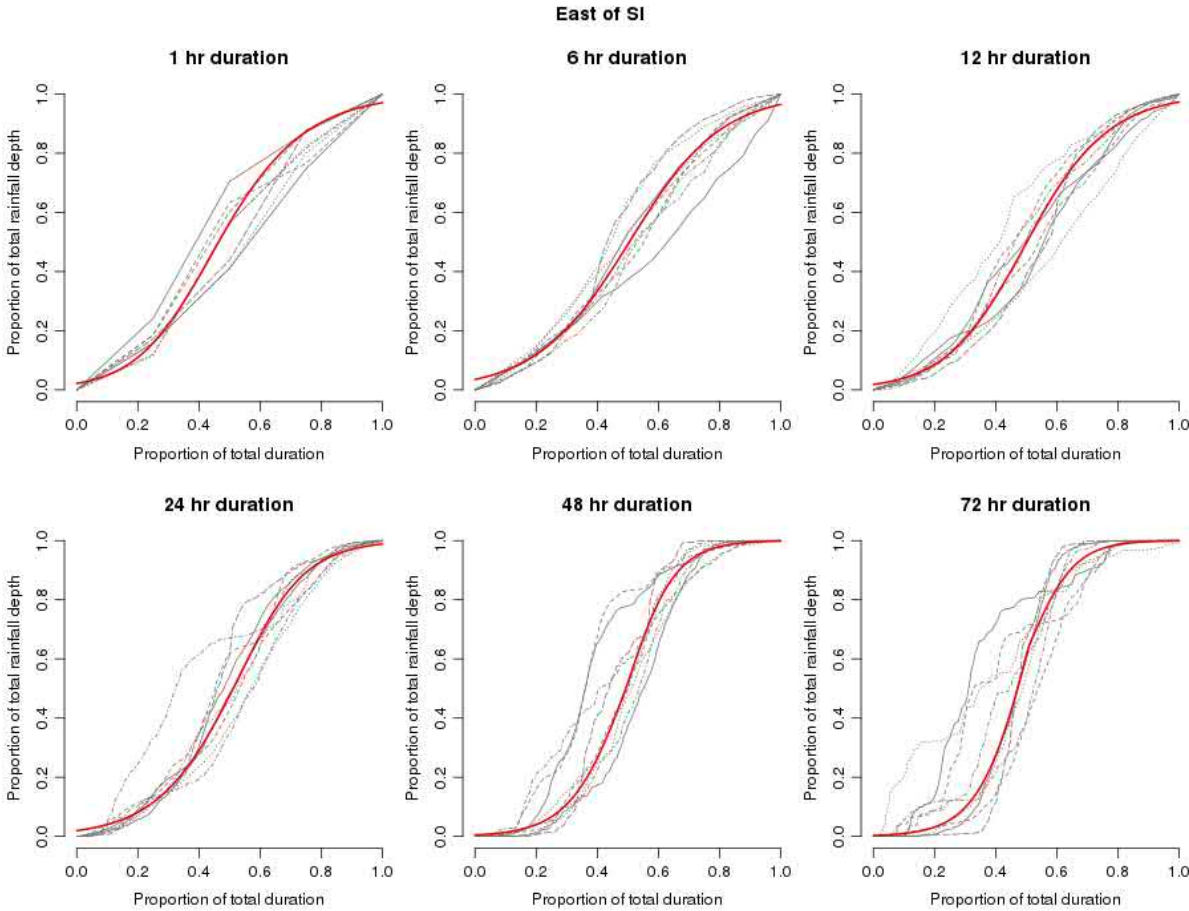


**Figure 33: Location of raingauges and regions used for the temporal design storm analysis.**

At each raingauge in Figure 33, and for durations of 1, 6, 12, 24, 48 and 72 hours, a sliding window was used to find the largest storm in each year. The average variability method was then applied to each multi-year series of storms to calculate a single hyetograph for each site and duration. Parameter values for Equation (8) were estimated for all durations at each of the 6 regions using a standard non-linear curve fitting method available in the R software language. Example results from this procedure are shown in Figure 34 for the East of SI region. It is evident from these results that the asymmetric hyperbolic tangent function provides a simple and robust model for cumulative hyetographs.

Figure 34 shows that the steepness of the hyetograph increases with duration, that is, as the storm duration gets longer, the rainfall is less evenly distributed across the event. It is also clear that for the longer durations, there is more variability in the individual raingauges. This is likely to be because the longer durations allow for multiple rain events to be included in the same storm, which introduces inconsistencies in the temporal ranking.

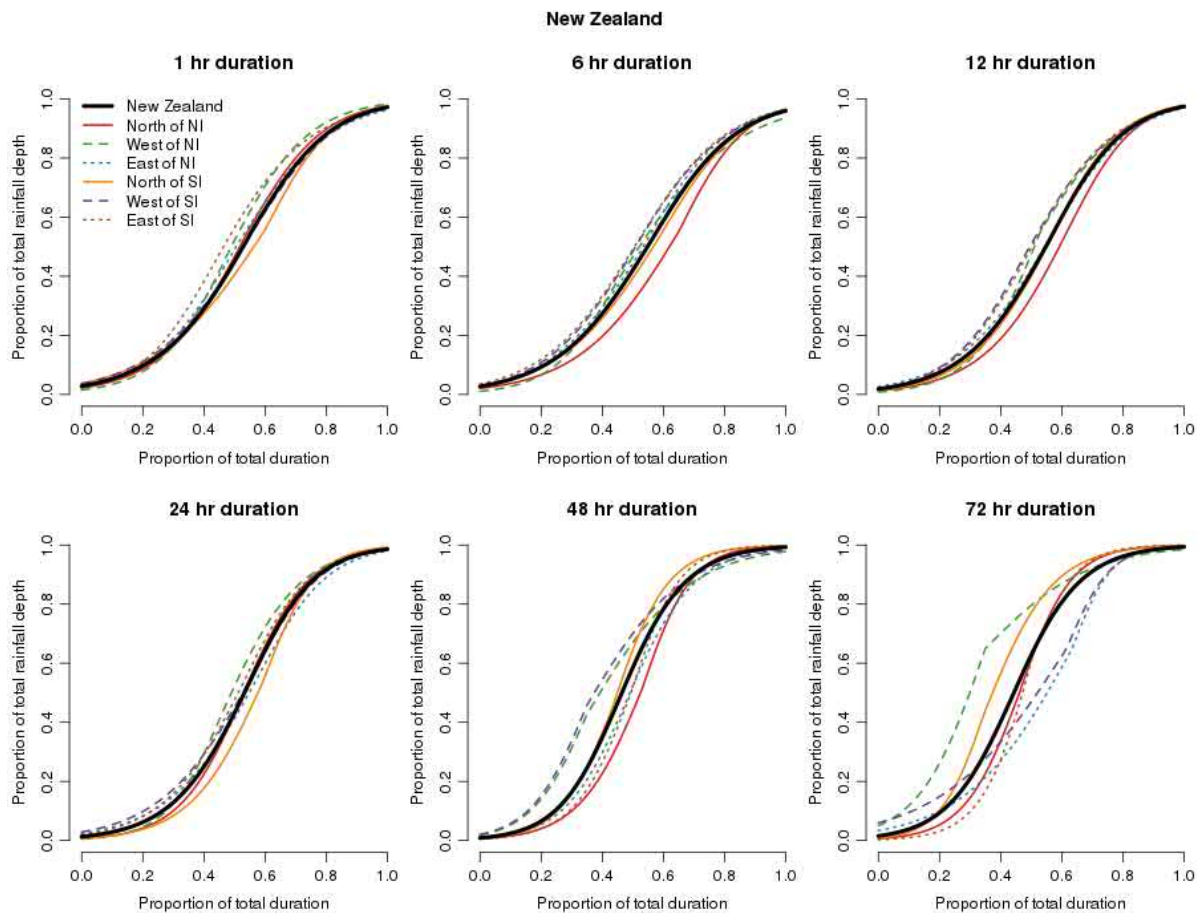
Results for all regions are listed in Table 11 and shown in Figure 35. The same general patterns seen in the East of SI region are also apparent across the country. All regions tend to show a steepening of the hyetograph with increasing duration and there is more similarity between sites at the shorter durations.



**Figure 34: Fitted cumulative hyetograph (red line) for raingauges in the east of the South Island region for all durations. The cumulative hyetographs based on observations from each raingauge are shown by thin grey lines.**

**Table 11: Parameter values in Equation (8) for each of the climate regions and the whole country. Parameters are given for 6 different storm durations.**

Region	Parameter	Duration (hr)					
		1	6	12	24	48	72
North of NI	$W_L$	3.58	3.05	3.55	4.71	4.85	5.52
	$W_R$	3.99	4.58	4.76	4.72	6.13	5.89
	$m$	0.55	0.55	0.58	0.52	0.51	0.50
	$n$	0.54	0.65	0.63	0.54	0.53	0.46
West of NI	$W_L$	4.28	4.77	4.57	5.52	5.44	4.60
	$W_R$	3.94	2.63	3.68	4.03	3.02	2.95
	$m$	0.50	0.38	0.56	0.43	0.43	0.65
	$n$	0.49	0.45	0.53	0.46	0.35	0.35
East of NI	$W_L$	3.54	3.31	3.25	3.3	5.18	2.86
	$W_R$	3.28	3.53	3.88	4.48	4.28	7.75
	$m$	0.50	0.48	0.54	0.57	0.43	0.65
	$n$	0.51	0.52	0.57	0.58	0.46	0.63
North of SI	$W_L$	2.79	3.04	3.80	4.20	5.79	6.77
	$W_R$	4.55	3.78	4.33	5.86	5.46	4.52
	$m$	0.56	0.54	0.51	0.54	0.44	0.44
	$n$	0.60	0.59	0.56	0.59	0.43	0.35
West of SI	$W_L$	2.96	3.52	4.05	3.24	5.40	2.46
	$W_R$	3.85	3.21	3.40	4.53	3.21	6.92
	$m$	0.59	0.46	0.46	0.56	0.46	0.65
	$n$	0.58	0.49	0.48	0.56	0.35	0.62
East of SI	$W_L$	4.38	3.27	4.07	3.75	5.39	5.93
	$W_R$	3.12	3.35	3.52	4.66	6.38	6.78
	$m$	0.40	0.50	0.45	0.55	0.51	0.65
	$n$	0.41	0.51	0.48	0.54	0.50	0.51
New Zealand	$W_L$	3.24	3.23	3.57	4.00	5.19	4.75
	$W_R$	3.91	3.55	4.09	4.61	4.51	4.45
	$m$	0.57	0.52	0.52	0.53	0.45	0.48
	$n$	0.57	0.56	0.56	0.55	0.45	0.43



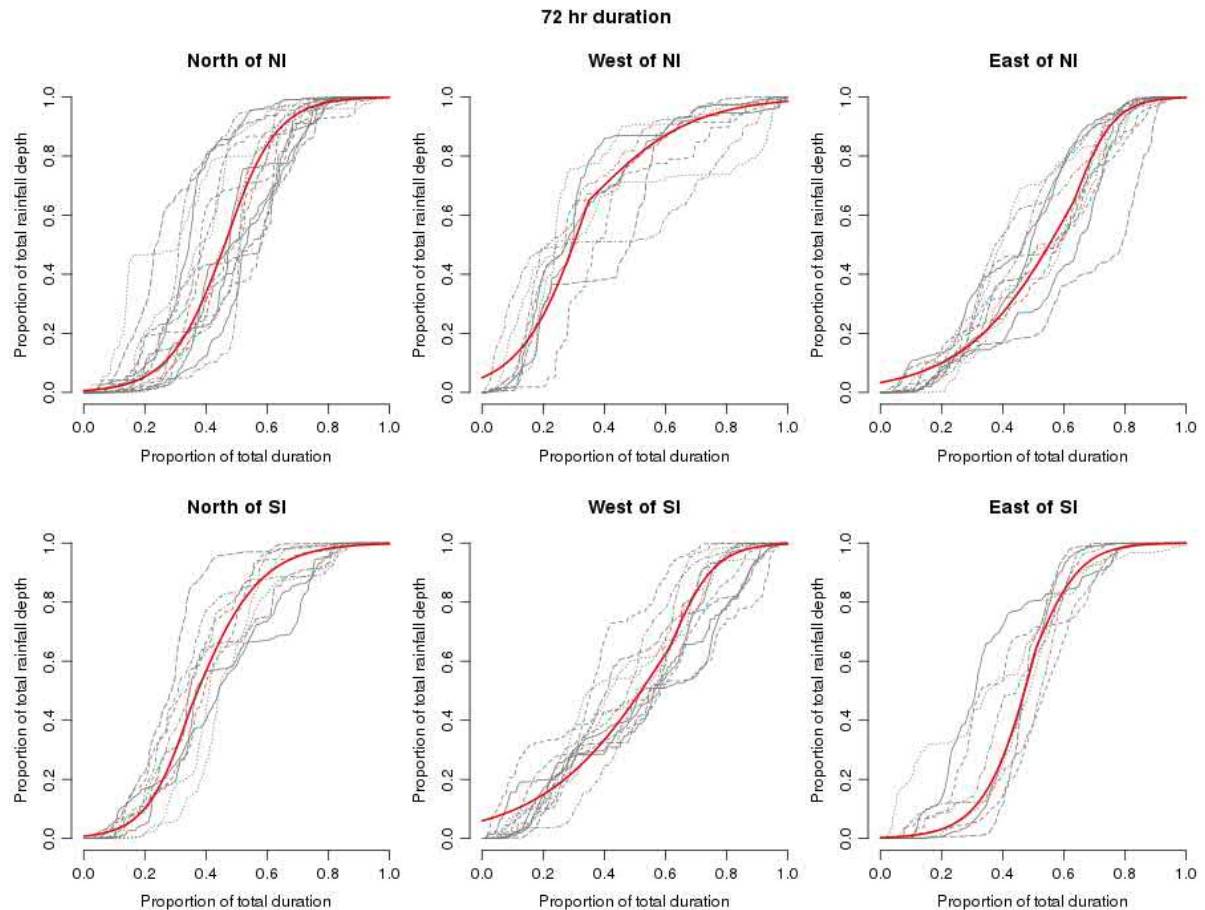
**Figure 35: Fitted cumulative hyetographs for various durations showing results for individual regions (coloured lines) and for the whole country (thick black line).**

Table 11 and Figure 35 also include results for New Zealand as a whole. These curves were fitted using the same methodology except that all gauges from all regions were used at the non-linear curve fitting step. For many regions, the country-wide hyetograph is likely to provide adequate patterns for design storm use as the different climate regions have broadly similar hyetographs.

However, some regions and durations have hyetographs which depart from the curve for New Zealand. For the shorter durations, storms in the East of SI region tend to peak earlier, while those in the North of NI and North of SI peak later. The largest regional differences are seen at longer durations where the West of NI peaks earliest and, for the 72-hour duration, both the East of NI and West of SI have storms with less intense peaks. However, these observations may not be very robust as quite different patterns are seen for the 48-hour duration. As stated above, this may relate to the longer duration containing more than one rain event which will tend to reduce the consistency between storms.

Figure 36 shows the fitted hyetograph for the 72-hour duration at all climate regions, including the individual site hyetographs used in the fitting process. The differences between regions are apparent and it is also clear that the asymmetric hyperbolic tangent function is not able to reproduce some of these curves as well as others. For example, the first half of the East of NI and West of SI hyetographs are nearly linear and, to provide the best fit to these lines, the hyperbolic tangent function no longer

has an intercept at  $m = 0$  and  $n = 0$ . Further research is needed as to whether a different functional form may provide better results, but while not perfect, the hyperbolic tangent function provides results adequate for most temporal design storm use-cases.



**Figure 36: Fitted cumulative hyetograph (red line) for the 72-hour duration at each climate region. The cumulative hyetographs based on observations from each raingauge are shown by thin grey lines.**

Figure 37 shows the four parameters necessary for describing the fitted hyetographs as a function of duration on a log scale. These plots show the relationship between the shape of the hyetograph and duration more clearly. For New Zealand as a whole, the parameters describing the curvature ( $W_L$  and  $W_R$ ) increase with duration and those describing the position of the inflection point ( $m$  and  $n$ ) decrease with duration. The fact that the latter two parameters tend to decrease together means that the most intense part of the storm occurs both earlier in time and after a smaller proportion of the total rain amount has fallen.

In most cases the regional parameters follow the same general pattern as the country-wide parameters, however they are much more variable, both between regions and between durations within the same region. This variability does reduce confidence in the regional parameters, although inspection of the fitted curves against raingauge data (Figure 34 and Figure 36) suggests the resulting curves are robust. The oscillating nature of some parameters (e.g., the  $m$  and  $n$  parameters for the West of NI) suggests that the function is over-parameterised and that altering one parameter can be compensated for by altering another.

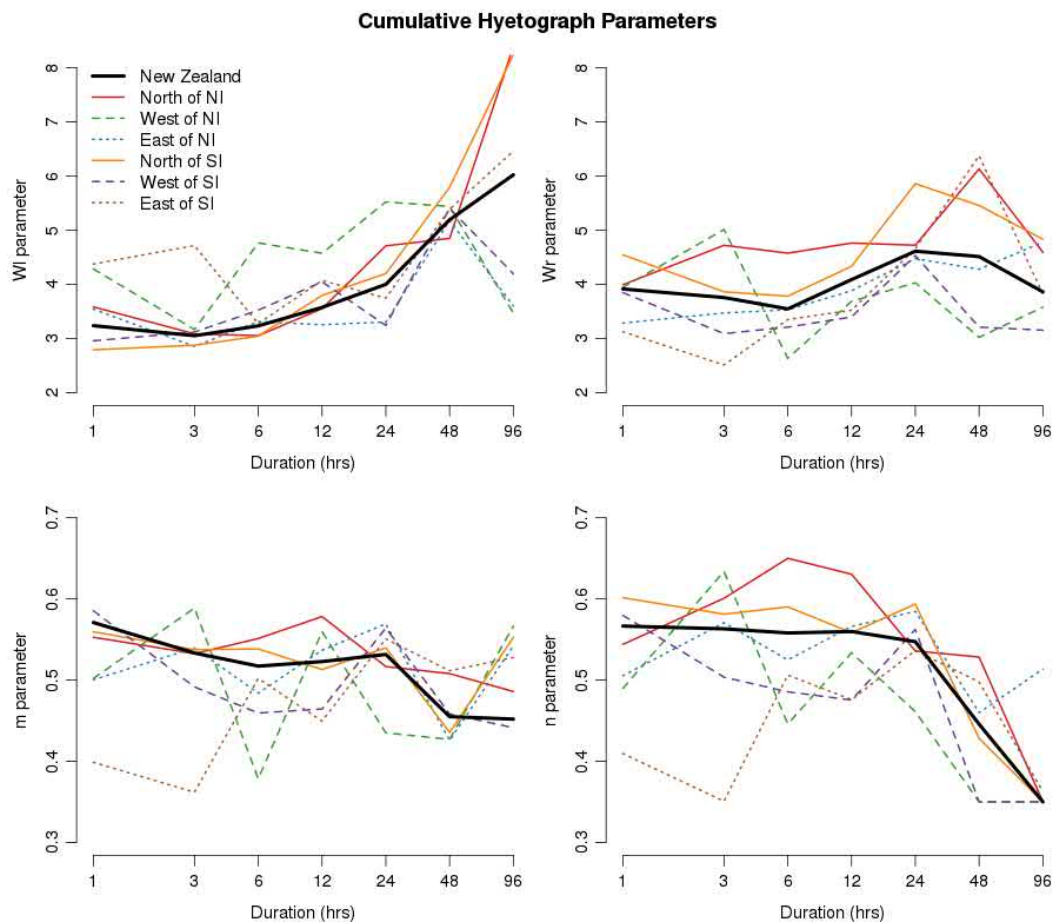


**Figure 37: Average fitted cumulative hyetographs for various durations for North and South Islands.**

In summary, the relative magnitude of a storm’s peak rain rate increases as the duration of the storm increases. This is not unexpected, as the most extreme short duration storms will tend to have high rain rates throughout the storm, whereas longer duration storms are likely to have one or more periods of very heavy rain interspersed with periods of moderate or light rain. For longer durations, the northern regions of both islands have the highest relative peak intensities. The timing of peak storm intensity varies with region, but there is no obvious pattern to this variability except for the West of NI, which tends to peak earlier for longer duration storms.

Finally, it is known that storm duration and area, topography, season, and possibly return period affect the temporal variation of heavy rainfalls in New Zealand [Tomlinson, 1978].

### 6.3.1 Return period

Cumulative hyetographs were calculated for all six durations and for a sample of regions using just 20 years of rainfall records. No significant difference was detected between the 20 years and the original 30 years’ results. Investigations in Australia yielded a similar outcome based on generally longer records [French and Jones, 2012]. The conclusion was that the derived design hyetographs could be used for storms having return periods up to 100 year [Australian Rainfall and Runoff, 1987; French and Jones, 2012]. Whether this is valid in New Zealand remains to be fully tested.



### 6.3.2 Use of cumulative hyetographs

In design, where actual rainfall is required, Equation (8) needs to be expressed in real units rather than proportions. Let  $R_T$  be the total rainfall, in mm, that falls during a period of length  $T$  and divide it into  $N$  equal length sections each containing rainfall  $r_t$ , where  $t = 1, \dots, N$ . The cumulative rainfall at time  $t$  is  $R_t = R_T P_t$ , where  $P_t$  comes from Equation (8) after substituting  $D$  with  $D_t = t/N$ ; that is

$$R_t = R_T \left( m \tanh \left[ \left( \frac{t}{N} - n \right) W_L \right] + m \right) \quad 0 \leq \frac{t}{N} \leq n$$

$$R_t = R_T \left( (1 - m) \tanh \left[ \left( \frac{t}{N} - n \right) W_R \right] + m \right) \quad n < \frac{t}{N} \leq 1$$

for  $t = 0, \dots, N$ .

The ordinary (as opposed to cumulative) hyetograph can be constructed from

$$r_t = R_t - R_{t-1} \quad (t = 1, \dots, N).$$

When the fitted hyetograph does not pass through  $R_0 = 0$  (as for West of NI in Figure 36), it is necessary to adjust the ordinary hyetograph to ensure the total rainfall matches  $R_T$ . This can be achieved using

$$r_t = (R_t - R_{t-1}) + \frac{R_T + R_0 - R_N}{N - 1} \quad (t = 1, \dots, N)$$

which simplifies to the previous version when  $R_0 = 0$  and  $R_N = R_T$ .

## 6.4 Summary

The asymmetric hyperbolic tangent function provides a simple and robust model for cumulative hyetographs derived empirically from raingauge data. Overall, the relative magnitude of a storm's peak rain rate increases as the duration of the storm increases. There is little regional difference between the cumulative hyetographs for short durations, although variability increases with duration, and there is no apparent influence of return period on the results. In most cases, for durations of 24 hours or less, using the New Zealand wide hyetograph instead of the regionally specific version will make little difference. For multi-day durations, however, it is recommended that the curve specific to the climate region be used.

Longer records of common period from a greater density of raingauges in more locations are required to make substantive progress in empirical calculations of design hyetographs. The influence of return period needs further investigation as does temporal rainfall patterns for durations less than one hour.

## 7 Conclusion

Using a regionalised index-frequency method, estimates of high intensity rainfall for all New Zealand have been revised. This project has endeavoured to utilise all available historical records and the most up-to-date rainfall measurements gathered from multiple agencies. This comprehensive data set has enabled more accurate estimates of median annual maximum rainfall and more robust regionalisation of growth curve parameters than was possible in earlier versions of this work. This is particularly true for sub-daily event durations and even more so sub-hourly durations.

The impact of future climate change on extreme rainfall has been assessed using regional climate model simulations of rainfall over New Zealand. From these simulations, amplification factors that can be applied to depth-duration-frequency tables have been estimated for four different emissions scenarios and two future time slices. These factors allow estimates of future extreme rainfall intensities to be derived based on those calculated from historical rainfall records.

Several established areal reduction methodologies have been applied to different regions across New Zealand and the *Bell* [1976] method has been selected as the most appropriate. Areal reduction factors have been estimated for three regions in New Zealand and a model based on data from these regions has been developed to provide areal reduction factors for New Zealand as a whole. A literature review and extensive analysis has been made into temporal design storm patterns and storm curves have been estimated for the six different climatically similar regions throughout New Zealand.

The estimates of high intensity rainfall derived in this report along with climate change projections are accessible using the online tool found at <https://hirds.niwa.co.nz>.

## 8 Acknowledgements

This work was funded by the Ministry for Business, Innovation and Employment via an Envirolink Tools Grant. Support for the project was provided from three local government Special Interest Groups; the River Manager's SIG (Mike Adye, Gary Clode, Graeme Campbell), Local Authority Environmental Monitoring SIG (Jeff Watson, Simon Tredgett, Mike Ede) and Regional Hazard Risk Management SIG (Lisa Pearse, Iain Dawe). Additional thanks to John Hansford, Nick Brown, Martin Doyle, Rick Liefing, Wilco Terink and others for their valuable and constructive feedback on earlier drafts of this report.

We acknowledge the support provided by regional and district councils in maintaining and providing many of the rainfall records used in this study. The additional effort that Auckland Council provided in quality checking data from the Auckland region was very helpful. Rainfall records from Fire and Emergency New Zealand have been a significant addition to this version of HIRDS and their willingness to allow use of this data is appreciated.

Assistance compiling and processing NHD rainfall records was ably provided by Kathy Walter. Initial work bringing the index-frequency software up to date for this version was done by Aran Mol. Advice and guidance related to areal reduction factors and temporal design storm analysis was provided by George Griffiths and Alistair McKerchar. Brett Mullan's initial analysis of extreme precipitation related to climate change was valuable as were Sam Dean and Andrew Tait's ideas around ways of applying results from the climate change analysis to HIRDS output.

Finally, many thanks go to Craig Thompson for his exemplary work on previous versions of the HIRDS tool, but also for giving up his time to assist and provide advice during this current project.

## 9 References

- Ailliot, P., C. Thompson, and P. Thomson (2011), Mixed methods for fitting the GEV distribution, *Water Resour Res*, 47, doi:10.1029/2010wr009417.
- Asquith, W. H., and J. S. Famiglietti (2000), Precipitation areal-reduction factor estimation using an annual-maxima centered approach, *J Hydrol*, 230(1-2), 55-69, doi:Doi 10.1016/S0022-1694(00)00170-0.
- Austin, P. M., and R. A. Houze (1970), Analysis of the structure of precipitation patterns in New England, *J. Appl. Meteorol*, 11, 926-934.
- Australian Rainfall and Runoff (1987), *A guide to flood estimation, Volume 1*, 374 pp., The Institution of Engineers Australia, Barton, ACT.
- Australian Rainfall and Runoff (2015), *Temporal patterns of rainfall. Project 3, Stage 3 Report*, 54 pp., Engineers Australia Water Engineering, ACT.
- Beable, M. E., and A. I. McKerchar (1982), Regional flood estimation in New Zealand. Water & Soil Tech. Publ. 20., edited, pp. 1-139, Ministry of Works and Development, Wellington.
- Bell, F. C. (1976), *The areal reduction factors in rainfall frequency estimation*, Natural Environment Research Council (NERC), Report No. 35, Institute of Hydrology, Wallingford, UK.
- Bhuiyan, T., A. Rahman, and S. Abbey (2010), Derivation of design rainfall temporal patterns in Australia's Gold Coast Region, paper presented at International Conference on Information and Knowledge Engineering, Las Vegas.
- Burn, D. H. (1990), Evaluation of Regional Flood Frequency-Analysis with a Region of Influence Approach, *Water Resour Res*, 26(10), 2257-2265, doi:DOI 10.1029/WR026i010p02257.
- Burn, D. H. (1997), Catchment similarity for regional flood frequency analysis using seasonality measures, *J Hydrol*, 202(1-4), 212-230, doi:Doi 10.1016/S0022-1694(97)00068-1.
- Burn, D. H., and N. K. Goel (2000), The formation of groups for regional flood frequency analysis, *Hydrolog Sci J*, 45(1), 97-112, doi:Doi 10.1080/02626660009492308.
- Carey-Smith, T., S. Dean, J. Vial, and C. Thompson (2010), Changes in precipitation extremes for New Zealand: climate model predictions, *Weather and Climate*, 30, 23-48.
- Carroll, D., and A. Rahman (2004), Investigation of subtropical rainfall characteristics for use in Joint Probability Approach to design flood estimation, paper presented at The Second Asia Pacific Association of Hydrology and Water Resources, Singapore.

Cluckie, I. D., and M. L. Pessoa (1990), Dam Safety - an Evaluation of Some Procedures for Design Flood Estimation, *Hydrolog Sci J*, 35(5), 547-569, doi:Doi 10.1080/02626669009492458.

Cunderlik, J. M., and D. H. Burn (2006), Switching the pooling similarity distances: Mahalanobis for Euclidean, *Water Resour Res*, 42(3), doi:10.1029/2005wr004245.

Dalrymple, T. (1960), Flood-frequency analysis, US Geol. Surv. Water Supply Pap. 1543-A, edited, US Govt. Printing Office, Washington DC.

de Lima, J. L. M. P., and V. P. Singh (2002), The influence of the pattern of moving rainstorms on overland flow, *Adv Water Resour*, 25(7), 817-828, doi:Pii S0309-1708(02)00067-2  
Doi 10.1016/S0309-1708(02)00067-2.

Durrans, S. R., and J. T. Kirby (2004), Regionalization of extreme precipitation estimates for the Alabama rainfall atlas, *J Hydrol*, 295(1-4), 101-107, doi:10.1016/j.jhydrol.2004.02.021.

Eagleson, P. S. (1970), *Dynamic hydrology*, xvi, 462 p. pp., McGraw-Hill, New York,.

Faulkner, D. S. (1999), *Rainfall frequency estimation, Flood Estimation Handbook Vol 2*, Institute of Hydrology, Wallingford.

Feng, Z., L. R. Leung, S. Hagos, R. A. Houze, C. D. Burleyson, and K. Balaguru (2016), More frequent intense and long-lived storms dominate the springtime trend in central US rainfall, 7, 13429, doi:10.1038/ncomms13429.

Fischer, E. M., and R. Knutti (2016), Observed heavy precipitation increase confirms theory and early models, *Nature Clim. Change*, 6(11), 986-991, doi:10.1038/nclimate3110.

French, R., and M. Jones (2012), Design rainfall temporal patterns in Australian Rainfall and Runoff: durations exceeding one hour, *Australasian Journal of Water Resources*, 16(1), 21-27.

García-Bartual, R., and I. Andrés-Doménech (2017), A two-parameter design storm for Mediterranean convective rainfall, *Hydrol. Earth Syst. Sci.*, 21(5), 2377-2387, doi:10.5194/hess-21-2377-2017.

Gilleland, E., and R. W. Katz (2016), extRemes 2.0: An Extreme Value Analysis Package in R, *J Stat Softw*, 72(8), 1-39, doi:10.18637/jss.v072.i08.

Graham, S., B. Dudley, A. Sood, J. Springer, and C. Zammit (2016), Climate change impacts on hourly precipitation across New Zealand, paper presented at 2016 joint Conference for NZ Hydrological Society, Australian Hydrology and Water Resources Symposium and IPENZ Rivers Group, Queenstown, New Zealand, 28 Nov - 2 Dec 2016.

Griffiths, G. A., A. I. McKerchar, and C. P. Pearson (2014), Towards prediction of extreme rainfalls in New Zealand, *Journal of Hydrology (NZ)*, 53(1), 41-52.

Griffiths, G. A., and C. P. Pearson (1993), Distribution of high intensity rainfalls in metropolitan Christchurch, New Zealand, *Journal of Hydrology (NZ)*, 31(1), 5-22.

Griffiths, G. A., C. P. Pearson, and G. A. Horrell (1989), Rainfall-runoff routing in the Waimakariri Basin, New Zealand, *Journal of Hydrology (NZ)*, 31(1), 5-22.

Griffiths, G. A., C. P. Pearson, and A. I. McKerchar (2009), *Review of the frequency of high intensity rainfalls in Christchurch. NIWA Report CHC2009-139*, 26 pp., National Institute of Water and Atmospheric Research, Christchurch, NZ.

Griffiths, G. M. (2007), Changes in New Zealand daily rainfall extremes 1930-2004, *Weather and Climate*, 27, 3-44.

Griffiths, G. M. (2013), New Zealand six main centre extreme rainfall trends 1962-2011, *Weather and Climate*, 33, 76-88.

Grimaldi, S., and F. Serinaldi (2006), Design hyetograph analysis with 3-copula function, *Hydrolog Sci J*, 51(2), 223-238, doi:DOI 10.1623/hysj.51.2.223.

Hosking, J. R. M. (1990), L-moments: Analysis and estimation of distributions using linear combinations of order statistics, *J. R. Stat. Soc., Ser. B*, 52(1), 105-124.

Hosking, J. R. M., and J. R. Wallis (1988), The Effect of Intersite Dependence on Regional Flood Frequency-Analysis, *Water Resour Res*, 24(4), 588-600, doi:DOI 10.1029/WR024i004p00588.

Hosking, J. R. M., and J. R. Wallis (1997), *Regional frequency analysis: An approach based on L-moments*, 224 pp., Cambridge University Press, Cambridge.

Hutchinson, M. F. (1995), Interpolating Mean Rainfall Using Thin-Plate Smoothing Splines, *Int J Geogr Inf Syst*, 9(4), 385-403, doi:Doi 10.1080/02693799508902045.

Intergovernmental Panel on Climate Change (2014), *Climate Change 2013 – The Physical Science Basis: Working Group I Contribution to the Fifth Assessment Report of the Intergovernmental Panel on Climate Change*, Cambridge University Press, Cambridge, doi:DOI: 10.1017/CBO9781107415324.

Jakob, D., K. Xuerub, and B. F. Taylor (2007), Revision of design rainfalls over Australia: A pilot study, *Aust. J. Water Resources*, 11(20), 153-159.

Jenkinson, A. F. (1955), The Frequency Distribution of the Annual Maximum (or Minimum) Values of Meteorological Elements, *Q J Roy Meteor Soc*, 81(348), 158-171, doi:DOI 10.1002/qj.49708134804.

Jowett, I. G., and S. M. Thompson (1977), *Clutha Power Development: Floods and Design Flows*, 114 pp., Ministry of Works and Development, Wellington, NZ.

Laurenson, E. M., M. R.G., and R. J. Nathan (2010), *RORB Version 6*, Monash University and Sinclair Knight Mertz, Melbourne.

Lenderink, G., and H. J. Fowler (2017), Hydroclimate: Understanding rainfall extremes, *Nature Clim. Change*, 7(6), 391-393, doi:10.1038/nclimate3305.

Lu, L. H., and J. R. Stedinger (1992), Variance of 2-Parameter and 3-Parameter Gev Pwm Quantile Estimators - Formulas, Confidence-Intervals, and a Comparison, *J Hydrol*, 138(1-2), 247-267, doi:10.1016/0022-1694(92)90167-T.

Marani, M., G. Grossi, F. Napolitano, P. Wallace, and D. Entekhabi (1997), Forcing, intermittency, and land surface hydrologic partitioning, *Water Resour Res*, 33(1), 167-175, doi:10.1029/96wr02670.

Martins, E. S., and J. R. Stedinger (2000), Generalized maximum-likelihood generalized extreme-value quantile estimators for hydrologic data, *Water Resour Res*, 36(3), 737-744, doi:10.1029/1999wr900330.

McKerchar, A. I., and C. P. Pearson (1989), Flood frequency in New Zealand. Hydrology Centre Publ. 20, edited, Department of Scientific and Industrial Research, Christchurch.

Morrison, J. E., and J. A. Smith (2002), Stochastic modeling of flood peaks using the generalized extreme value distribution, *Water Resour Res*, 38(12), doi:10.1029/2001wr000502.

Mullan, B., A. Sood, and S. Stuart (2016), Climate Change Projections for New Zealand: Atmosphere Projections Based on Simulations from the IPCC Fifth Assessment, edited, Ministry for the Environment, Wellington.

Mullan, B., D. Wratt, S. Dean, M. Hollis, S. Allan, T. Williams, and G. Kenny (2007), Climate Change Effects and Impacts Assessment: A guidance manual for local government in New Zealand updated 2007, *WLG2007/62. Rep. Available from [www.mfe.govt.nz](http://www.mfe.govt.nz)*, NIWA Client Report for Ministry for the Environment.

Nandakumar, N., E. Weinmann, R. G. Mein, and R. J. Nathan (1997), Estimation of extreme rainfalls for Victoria using the CRC-FORGE method. Report 97/4, edited, pp. 1-118, Cooperative Research Centre for Catchment Hydrology, Monash University.

Natural Environment Research Council (1975), *Flood Studies Report 2: Meteorological Studies*, 81 pp., Natural Environment Research Council, London.

Olivera, F., J. Choi, D. Kim, and M. H. Li (2008), Estimation of average rainfall areal reduction factors in Texas using NEXRAD data, *J Hydrol Eng*, 13(6), 438-448, doi:10.1061/(Asce)1084-0699(2008)13:6(438).

Pearson, C. P., and R. D. Henderson (1998), Frequency distributions of annual maximum storm rainfalls in New Zealand, *Journal of Hydrology (New Zealand)*, 37(1), 19-33.

Pfahl, S., P. A. Ogorman, and E. M. Fischer (2017), Understanding the regional pattern of projected future changes in extreme precipitation, *Nature Clim. Change*, 7(6), 423-427, doi:10.1038/nclimate3287.

Pietersen, J. P. J., O. J. Gericke, J. C. Smithers, and Y. E. Woyessa (2015), Review of current methods for estimating areal reduction factors applied to South African design point rainfall and preliminary identification of new methods, *J S Afr Inst Civ Eng*, 57(1), 16-30, doi:10.17159/2309-8775/2015/v57n1a2.

Pilgrim, D. H., and I. Cordery (1975), Rainfall Temporal Patterns for Design Floods, *J Hydr Eng Div-Asce*, 101(Nhy1), 81-95.

Podger, S., J. Green, C. Jolly, C. The, and C. Beesley (2015), Creating long duration areal reduction factors, paper presented at 36th Hydrology and Water Resources Symposium, Barton, Australia.

Prein, A. F., R. M. Rasmussen, K. Ikeda, C. Liu, M. P. Clark, and G. J. Holland (2017), The future intensification of hourly precipitation extremes, *Nature Clim. Change*, 7(1), 48-52, doi:10.1038/nclimate3168.

Rahman, A., P. Mahbub, K. Rahman, and S. Shrestha (2006), Variability of rainfall temporal patterns and its impacts on design flood estimation, paper presented at 30th Hydrology & Water Resources Symposium, Launceston.

Reed, D. W. (1999), *Overview, Flood Estimation Handbook Vol 1*, Institute of Hydrology, Wallingford.

Robertson, N. G. (1963), *The Frequency of High Intensity Rainfalls in New Zealand. Misc. Pub. No. 118*, New Zealand Meteorological Service.

Robson, A., and D. W. Reed (1999), *Statistical procedures for flood frequency estimation, Flood Estimation Handbook Vol 3*, Institute of Hydrology, Wallingford.

Seelye, C. J. (1947), *The Frequency of Heavy Rainfall in New Zealand. Note 33.*, New Zealand Meteorological Office.

Singh, S. K., G. A. Griffiths, and A. I. McKerchar (2018), Towards estimating areal reduction factors for design rainfalls in New Zealand, *Journal of Hydrology (NZ)*, in publication.

Smith, J. A. (1993), Precipitation, in *Handbook of Hydrology*, edited by D. R. Maidment, pp. 3.1-3.47, McGraw-Hill, New York.

Srikanthan, R. (1995), A review of the methods for estimating areal reduction factors for design rainfalls. Report 95/3, edited, Cooperative Research Centre for Catchment Hydrology, Monash University, Australia.

Stewart, E. J., D. W. Reed, D. S. Faulkner, and N. S. Reynard (1999), The FORGEX method of rainfall growth estimation - I: Review of requirement, *Hydrol Earth Syst Sc*, 3(2), 187-195.

Svensson, C., and D. A. Jones (2010), Review of methods for deriving areal reduction factors, *J Flood Risk Manag*, 3(3), 232-245, doi:10.1111/j.1753-318X.2010.01075.x.



Tait, A., R. Henderson, R. Turner, and X. Zheng (2006), Thin plate smoothing spline interpolation of daily rainfall for New Zealand using a climatological rainfall surface, *International Journal of Climatology*, 26(14), 2097-2115.

Thompson, C. (1992), HIRDS (Manual and software), edited, pp. 1-20, National Institute of Water and Atmosphere, Wellington.

Thompson, C. (2002), The High Intensity Rainfall Design System: HIRDS, paper presented at International Conference on Flood Estimation, International Commission for the Hydrology of the Rhine Basin, Berne, Switzerland.

Thompson, C. (2011), HIRDSV3: High Intensity Rainfall Design System, edited, pp. 1-27, National Institute of Water and Atmosphere, Wellington.

Tomlinson, A. I. (1978), Storm rainfalls, *Journal of Hydrology (NZ)*, 17(2), 57-77.

Tomlinson, A. I. (1980), The frequency of high intensity rainfall. Part 1: soil and water, Tech. Publ. 19, edited, Ministry of Works and Development, Christchurch.

Trenberth, K. E. (1999), Conceptual Framework for Changes of Extremes of the Hydrological Cycle with Climate Change, *Climatic Change*, 42(1), 327-339, doi:10.1023/A:1005488920935.

United States Weather Bureau (1957), *Rainfall-intensity-duration regime. Technical Paper 29*, US Dept of Commerce, Washington, DC.

Viglione, A., F. Laio, and P. Claps (2007), A comparison of homogeneity tests for regional frequency analysis, *Water Resour Res*, 43(3), doi:10.1029/2006wr005095.

Withers, C. S., and C. P. Pearson (1991), *Detecting climate change in New Zealand rainfall and runoff records: a progress report. Physical Science Report 22*, 150 pp., Dept of Scientific and Industrial Research, Wellington, NZ.